



HAL
open science

**Fabrication of grating waveguide structures for spectral
(and linear polarization) stabilization and wavelength
multiplexing for 976 nm, 1030 nm, and 2000 nm
wavelength range**

Ratish Rao Nagaraj Rao

► **To cite this version:**

Ratish Rao Nagaraj Rao. Fabrication of grating waveguide structures for spectral (and linear polarization) stabilization and wavelength multiplexing for 976 nm, 1030 nm, and 2000 nm wavelength range. Optics [physics.optics]. Université Jean Monnet - Saint-Etienne, 2022. English. NNT : 2022STET0049 . tel-04199016

HAL Id: tel-04199016

<https://theses.hal.science/tel-04199016>

Submitted on 7 Sep 2023

HAL is a multi-disciplinary open access archive for the deposit and dissemination of scientific research documents, whether they are published or not. The documents may come from teaching and research institutions in France or abroad, or from public or private research centers.

L'archive ouverte pluridisciplinaire **HAL**, est destinée au dépôt et à la diffusion de documents scientifiques de niveau recherche, publiés ou non, émanant des établissements d'enseignement et de recherche français ou étrangers, des laboratoires publics ou privés.



N° d'ordre NNT :2022STET0049

**THÈSE DE DOCTORAT DE L'UNIVERSITE JEAN MONNET
SAINT-ETIENNE MEMBRE DE L'UNIVERSITE DE LYON**

Opérée au sein de

Laboratoire Hubert Curien

Ecole Doctorale ED SIS 488

Sciences Ingénierie Santé SIS

Spécialité de doctorat : Optique, Photonique, Hyperfréquence

Soutenue publiquement le 08/12/2022, par

Ratish Rao NAGARAJ RAO

**Fabrication of grating waveguide structures for
spectral (and linear polarization) stabilization and
wavelength multiplexing for 976 nm, 1030 nm, and
2000 nm wavelength range**

Devant le jury composé de :

M. LUMEAU, Julien	DR CNRS, Institut Fresnel, Aix-Marseille Université	Rapporteur, Président
M. BISSON, Jean-François	Pr, Faculté des sciences, Université de Moncton (CA)	Rapporteur
M. ABDOU AHMED, Marwan	Dr HDR, Institut für Strahlwerkzeuge (IFSW), USTUTT (DE)	Examinateur
Mme. VERRIER, Isabelle	CR CNRS HDR, Laboratoire Hubert Curien - UMR 5516 – UJM	Examinatrice
M. KÄMPFE, Thomas	Dr, Jena-Optronik GmbH, Jena (DE)	Invité
M. JOURLIN, Yves	Pr, Laboratoire Hubert Curien - UMR 5516 – UJM	Directeur de thèse
Mme. GAMET, Emilie	MCF, Laboratoire Hubert Curien - UMR 5516 – UJM	Co-encadrante de thèse

I dedicate this thesis to my parents, Radha Bai and Nagaraj Rao, my brother Satish Rao, and my best friend, Sourabh K. I am forever grateful for their love and presence in my life.

Acknowledgments

I am very grateful to my research supervisor Prof. Yves JOURLIN for his mentoring, genuine support, and trust from day one of my research in Laboratoire Hubert Curien. I sincerely thank my research co-supervisor Dr. Emilie GAMET for her unmatched guidance and support throughout my research. I also greatly appreciate the time spent under the supervision of Dr. Thomas KÄMPFE during the first two years of my Ph.D.

I wholeheartedly thank Frederic CELLE for training me on Laser Interference Lithography and for the many fruitful discussions during my work in the Nano Saint-Etienne. I am glad to have been a part of the Micro- and Nano-structuring team and share the workspace with friendly colleagues Arnaud VALOUR, Emilie LAFFONT, Erieta Katerina KOUSSEI, Julie DUTEMS, Hugo BRUHIER, Lea MARICHEZ, and Manuel FLORES.

My sincerest thanks to my fellow ESRs, Adrian GRANDE, Anton SAVCHENKO, Ayoub BOUBEKRAOUI, Danish BASHIR, Denys DIDYCHENKO, Fangfang LI, Giovanna CAPRARO, Georgia MOURKIOTI, Goby GOVINDASSAMY, Janis ZIDELUNS, Marek Stehlik, Marina FETISOVA, Muhammad GHAWAS, and Sayed MUHAMMAD BAKER for the time spent and ideas shared during the project workshops and monthly meetings.

My deepest gratitude to Dr. Marwan ABDOU AHMED for his brilliant leadership, ever-curious questions, and technical discussions during my research time, and a huge shout out to all the supervisors and mentors from the partner institutions in the GREAT project consortium for their constant encouragement and support.

Finally, I sincerely admire and appreciate the Marie-Skłodowska-Curie innovative training network (ITN) for funding my Ph.D. program and providing a platform to participate in a robust and highly motivated GREAT project.

Table of Contents

Acknowledgements	III
Abstract	5
List of Figures	9
List of tables	19
General Introduction	21
Chapter 1: Organizational and theoretical framework	27
1.1. The GREAT project	27
1.1.1. Objectives of the GREAT project	28
1.2. Grating waveguide structures (GWS).....	33
1.2.1. Principle of diffraction gratings	34
1.2.2. Principle of planar waveguide	38
1.2.3. Literature overview	39
1.3. Targeted applications	47
1.3.1. Pulse compression for solid-state laser (A1-A2).....	48
1.3.2. Spectral stabilization and wavelength multiplexing for diode and solid-state lasers (A3-A4).....	50
1.3.3. Generation of radial and azimuthally polarized beams in thin-disk lasers (A5).....	51
1.4. Laser interference lithography (LIL)	54
1.4.1. Overview of maskless lithography techniques	54

1.4.2.	Two-spherical beam LIL configuration	60
1.5.	Conclusion	64
Chapter 2: Fabrication and characterization of grating structures		67
2.1.	Introduction	67
2.2.	Design of GWS	70
2.2.1.	Low index GWS for A3 application	71
2.2.2.	High index GWS for A3 application	73
2.2.3.	High index GWS for A4 application	74
2.3.	Fabrication of grating structures	77
2.3.1.	Fabrication of GWS	77
2.3.2.	Fabrication of Si master	83
2.4.	Characterization of grating structures	84
2.4.1.	High index GWS for A4 application	85
2.4.2.	Optical characterization of high-index GWS for A4 application	89
2.4.3.	Low-index Si master for A3 application	94
2.5.	Defects in the grating structures	97
2.6.	Conclusion	99
Chapter 3: Reduction of Grating Period Variation		103
3.1.	Introduction	103
3.2.	Implementation of substrate bending technique	104
3.2.1.	A period variation on a flat substrate	104
3.2.2.	Bending of a flat substrate	107
3.3.	Experimental demonstration of period variation reduction	108

3.3.1. Period variation of flat exposure vs. curved exposure	108
3.3.2. Period variation at different grating period settings	112
3.3.3. Period variation reduction using two LIL configurations	113
3.4. Substrate flatness analysis by optical profilometry	116
3.5. Wavefront aberration analysis by adaptive wavefront interferometry	118
3.6. Conclusion	120
General Conclusion	123
Bibliography	129

Abstract

This Ph.D. work is part of the European project GREAT (Grating Reflectors Enabled Applications and Training). The project focuses on exploring production technologies through appropriate control of the manufacturing process of Grating Waveguide Structures (GWS) for high-power laser systems.

The objective of this thesis is to develop GWS for spectral stabilization and wavelength multiplexing of a 976 nm emitting laser diode and a 1 μm emitting solid-state laser. The main focus of this work is on GWS fabrication by Laser Interference Lithography (LIL) and on optimizing this technique to obtain a better uniformity of the grating period.

The LIL fabrication of GWS on multilayers is detailed from the fabrication of the multilayer to the final etching step. The fabricated gratings are then characterized optically and geometrically. The GWS sample used for a solid-state laser system emitting at 1 μm showed a diffraction efficiency of 92%.

The fabrication of silicon (Si) molds is also detailed. This development is motivated by their eventual use as a buffer in the nanoimprint lithography (NIL) technique to produce GWSs faster and at a lower cost.

An important result of this work is based on the quantitative study of an established technique, namely, the deformation of the substrate during the interferential lithography step to reduce the period variation due to the use of divergent exposure beams. Experimental results show an average reduction of about 85% in period variation for a 4-inch diameter substrate.

Résumé

Ce travail de doctorat s'inscrit dans le cadre du projet européen GREAT (Grating Reflectors Enabled Applications and Training). Le projet porte sur l'exploration des technologies de production par un contrôle approprié du processus de fabrication de réseaux résonants (Grating Waveguide Structures - GWS) pour des systèmes laser haute puissance.

L'objectif de cette thèse est de développer des GWS pour la stabilisation spectrale et le multiplexage de longueurs d'onde d'une diode laser émettant à 976 nm et d'un laser à l'état solide émettant à 1 μm . Ce travail se concentre principalement sur la fabrication GWS par lithographie interférentielle (Laser Interference Lithography - LIL) et sur l'optimisation de cette technique pour obtenir une meilleure uniformité de la période du réseau.

La fabrication par LIL de GWS sur multicouche est détaillée depuis la fabrication du multicouche jusqu'à l'étape finale de gravure. Les réseaux ainsi fabriqués sont ensuite caractérisés optiquement et géométriquement. L'échantillon GWS utilisé pour un système laser à l'état solide émettant à 1 μm a montré une efficacité de diffraction de 92%.

La fabrication des moules en silicium (Si) est également détaillée. Ce développement est motivé par leur utilisation, à terme, comme tampon dans la technique de lithographie par nano-impression (NIL) pour produire des GWS plus rapidement et à moindre coût.

Un résultat important de ce travail est basé sur l'étude quantitative d'une technique établie, à savoir la déformation du substrat pendant l'étape de lithographie interférentielle pour réduire la variation de période due à l'utilisation de faisceaux d'exposition divergents. Les résultats expérimentaux montrent une réduction moyenne d'environ 85% de la variation de période pour un substrat de 4 pouces de diamètre.

List of Figures

1.1.	Seven work packages in establishing the GREAT project.....	30
1.2.	Overview of different fabrication techniques explored for producing GWS in a GREAT project.....	31
1.3.	Schematic sketch of a diffraction grating of period Λ , and the incident light is split into m diffracted orders (reflected and transmitted orders)	35
1.4.	Representation of diffracted orders (reflection and transmitted orders) from the diffraction grating surface in (a) real geometrical space (direct space) and (b) reciprocal space (indirect space), also referred to as Ewald sphere for incident light at $\theta_{inc} = 0$ (normal incidence).	37
1.5.	Representation of diffracted orders (reflection and transmitted orders) from the diffraction grating surface in (a) real geometrical space (direct space) and (b) reciprocal space (indirect space), also referred to as Ewald sphere for incident light at $\theta_{inc} \neq 0$ (oblique incidence).	37
1.6.	Schematic of dielectric planar waveguide	38
1.7.	Schematic mechanism of resonance effect in GWS structures	40

1.8.	(a) Schematic mode coupling mechanism in the waveguide integrated with grating structures, (b) Ewald Sphere or reciprocal space representation of the mode coupling in the waveguide	41
1.9.	a) Simulation of GWS using RCWA is tuning the reflection bandwidth in TM polarization. The parameters used in the design are: $\theta = 15^\circ$, period = 400 nm, DC = 0.5, the thickness of waveguide layer, $t = 300$ nm, b, c) Simulation of GWS using RCWA for board band operation of GWS reflectors in the wideband IR wavelength range. b) Parameters: $\theta = 0^\circ$, period = 700 nm, DC = 0.75, grating depth, $d = 460$ nm, $t = 840$ nm, c) Parameters: $\theta = 0^\circ$, period = 340 nm, DC = 0.68, $d = 220$ nm, $t = 2 \mu\text{m}$	44
1.10.	a) RCWA simulation of a GWS transmission wideband filter operated at Rayleigh anomaly in TM polarization. Parameters used for the simulation are: period= 1130 nm, DC = 0.723, depth = 405 nm, the thickness of waveguide = 160 nm, b–e) (c) Electric field distribution for the case study near Rayleigh anomaly in TM polarization, (c) field distribution at resonance condition (e) strong transfer of efficiency from zeroth order to first order which resulted in the dip in the transmission of zeroth order	45
1.11.	Schematic in the top view of GWS used in thermos-optic tunable filtering by Joule heating arrangement	46
1.12.	(a) SEM image of a T-like GWS structure with Silicon on a silica substrate. (b) Schematic of a single silicon crystal GWS mirror	47
1.13.	The configuration of pulse compression using G_1 - G_2 GWS pairs	49

1.14. Schematic configuration of wavelength multiplexing of diode laser array by using GWS to combine the wavelengths ($\lambda_1, \lambda_2, \lambda_3, \dots, \lambda_n$) from n number of diode lasers using a focusing lens	51
1.15. GWS schematic mechanisms developed in the GREAT project for generating azimuthal and radial polarization with a multilayer structure substrate of alternating Ta ₂ O ₅ /SiO ₂ layers. (a) GWS structure to generate radial polarization with circular grating lines etched on multilayer stack (b) GWS structure to generate radial polarization with circular grating lines on Ta ₂ O ₅ layer with multilayer deposited on the grating lines resulting in the multilayer grating profile. (c) Crystalline GWS structure generates azimuthal polarization by etching grating lines on sapphire substrate and depositing multilayers	53
1.16. Transformation of linear polarization to radial polarization using segmented GWS	54
1.17. Schematic illustration of the EBL process. The electron beam is focused on electron sensitive resist layer for the patterning of nanostructures	55
1.18. (a) Schematic of the SBIL system. (b) Illustrates the SBIL process setup for patterning circular gratings. (c) The substrate stage is rotated, resulting in the ring patterns of gratings	56
1.19. (a) Principal steps involved in the NIL patterning process	57
1.20. LIL setups with interferometry arrangement. (a) Two-beam LIL interferometer, (b) Single-beam interferometer (Lloyd's interferometer).....	58

1.21.	Interference fringes formed two different LIL setups with (a) Two-spherical beams resulting in the hyperbolic fringe patterning. (b) Two collimated beams resulted in the near-linear fringe patterning	60
1.22.	Schematic configuration of the two-spherical beam LIL setup used for the grating patterning GWS and Si masters (Nano Saint-Etienne platform, France). The Spherical-beam interference fringes are of hyperbolic shapes due to the fringe inclination, and the interference angle changes when moved away from the center of the substrate..	61
1.23.	Schematic of active fringe stabilization setup	62
1.24.	Interference pattern recording mechanism in the positive and negative photoresist-coated substrate	63
2.1.	Technical WPs overview of research methodology in developing GWS	68
2.2.	Responsible tasks performed in this thesis work	70
2.3.	Design of low-index GWS for A3 application, (a) sketch with design parameters. (b) The calculated DE plot for TE at 0 th and -1 st order with TE ₀ >92.5% and TE ₋₁ <7.5% at 976 nm.....	71
2.4.	Simulated tolerance of low-index GWS for A3 application, (a) Grating depth tolerance for variation from -20 nm to +10 nm. (b) Duty Cycle tolerance for variation from -30 % to +30 %. (c) Grating period tolerance for variation from -5 nm to +5 nm	72
2.5.	Design of high-index GWS for A3 application, (a) sketch with design parameters. (b) The calculated DE plot for TE at 0 th and -1 st order with TE ₋₁ >99.9% at 976 nm	73

2.6.	Simulated tolerance of high-index GWS for A3 application, (a) Grating depth tolerance for variation from -30 nm to +30 nm. (b) Duty Cycle tolerance for variation from -40 % to +40 %. (c) Grating period tolerance for variation from -5 nm to +5 nm	74
2.7.	Design of high-index GWS for A4 application, (a) sketch with design parameters. (b) The calculated DE plot for TE and TM -1 st order with $TE_{-1} > 99.9\%$ at 1030 nm.....	75
2.8.	Simulated tolerance of high-index GWS for A4 application, (a) Grating depth tolerance for variation from -30 nm to +30 nm. (b) Duty Cycle tolerance for variation from -20 % to +10 %. (c) Grating period tolerance for variation from -5 nm to +5 nm	76
2.9.	Working principle of Plasma assisted reactive magnetron sputtering	78
2.10.	Complete fabrication process flow of grating with LIL direct patterning technique. The multilayer deposition (a) was carried out at Institut Fresnel (IF) by ESR 6, France. The process of BARC and photoresist deposition (b-c) and LIL patterning and development of photoresist gratings structures (d) are performed at Hubert Curien laboratory (LabHC), France. The etching process (f-g) is performed at the University of Eastern Finland (UEF) with the help of ESR 5, Finland	79
2.11.	(a) The schematic sketch and (b) a Photograph of the LIL setup (Nano Saint-Etienne platform, LabHC).....	81
2.12.	Fabrication chain of Si master grating with LIL technique	83

2.13. AFM data and grating profile of photoresist grating surface on 2-inch multilayer substrate for A4 application	85
2.14. SEM image of chromium etched grating surface on 2-inch multilayer substrate for A3 application	86
2.15. (a)SEM image (b) Photograph, and (c) AFM data and grating profile of Nb ₂ O ₅ etched grating surface on 2-inch multilayer substrate for A4 application.	87
2.16. Variation in grating depth and Duty Cycle on 2-inch Nb ₂ O ₅ etched multilayer GWS with grating depth varying by 24 nm and Duty Cycle varying by 9% along the central <i>x</i> -axis for A4 application	88
2.17. A measured period variation along the 2-inch high index GWS for A4 application with a grating period of 623 nm at the substrate's center. The orange plot (▲) is the period variation along the <i>x</i> -axis. The blue plot (●) is the period variation along the <i>y</i> -axis. The error bar reflects the uncertainty in the diffraction angle measurements.	88
2.18. (a) The schematic configuration of DE measurement setup to analyze the DE response of the GWS sample using a tunable diode laser in the 1000 nm to 1070 nm range. (b) Photograph of the measurement setup 1. Diode laser output from polarization maintaining fiber, 2. Collimating lens, 3. Polarizer and $\lambda/2$ waveplate, 4. Laser chopper, 5. The beam splitter, 6. Chopper mirror, 7. GWS sample holder, 8. HR mirror, 9. Integrating sphere, 10. White screen for aligning reference and reflected laser beam from the GWS sample	90

2.19. The measured DE of TE and TM -1 st orders of GWS with a grating period of 623.5 nm and grating depth of 80 nm with a Duty Cycle of 30%.....	91
2.20. The measured spatial DE in TE -1 st order of 2-inch GWS with a grating period of 623.5 nm and grating depth of 80 nm with a Duty Cycle of 30%.....	92
2.21. Recalculated DE for TE and TM in -1 st order for GWS parameter obtained by fabrication process with grating period 623.5 nm, grating depth of 80 nm, and Duty Cycle of 30%. DE at 1030 nm for TE -1 st order is 91.5%.....	93
2.22. AFM data and grating profile of photoresist grating surface on a 2-inch Si substrate to develop master gratings for A3 application	94
2.23. (a) SEM image, (b) Photograph, and (c) AFM data and grating profile of Si etched master grating with a grating depth of 243 nm at the center of the substrate and Duty Cycle of 9% on 2-inch Si for A3 application.	95
2.24. Variation in grating depth and Duty Cycle on 2-inch Si etched master grating with grating depth varying by 13 nm and Duty Cycle varying by 7% along the central <i>x</i> -axis for A3 applications.....	95
2.25. A measured period variation along the 2-inch Si master grating A3 application with a grating period of 556 nm at the substrate's center. The orange plot (▲) is the period variation along the <i>x</i> -axis. The blue plot (●) is the period variation along the <i>y</i> -axis. The error bar reflects the uncertainty in the diffraction angle measurements.....	96

2.26.	Photograph of the Si substrate with nonuniform development of photoresist grating resulting in macroscopic concentric rings	98
2.27.	SEM image of GWS fabricated and etched in direct LIL fabrication process flow with defect spots with spot sizes from 2 μm to 10 μm	96
3.1.	LIL setup with spherical wavefronts forming hyperbolic fringes .	104
3.2.	Sketch of the spherically curved substrate with a good point P and its average vector \vec{n}_S indicating the parameters used in Eqn. (3.1) to (3.5)	106
3.3.	Calculated period distributions with the equations from Bienert et al.. The color scale indicates the period. (a): Flat substrate. (b): Curved substrate with a radius of curvature of 1000 mm.	107
3.4.	(a) Sketch of the bending process of a silicon wafer by concave vacuum chuck. (b) Image of concave vacuum chuck mounted on substrate holder stand with silicon wafer curved using vacuum supply.	108
3.5.	Photograph of fabricated photoresist grating on a 4-inch silicon wafer of thickness 525 μm using concave vacuum chuck holder by two-spherical-beam 442 nm LIL setup with an exposure time of 3 minutes and developing time of 5 seconds at 21°C	109
3.6.	Schematic of diffraction period measurement at Littrow configuration	109
3.7.	A measured period variation along the x -axis (a) and y -axis (b) on the silicon wafer exposed by two spherical waves at the central period of 1000 nm. The orange plot (\blacktriangle) is the period variation on the flat	

- exposed substrate. The blue plot (●) is the period variation on the curved exposed substrate. The error bars indicate the uncertainty in the diffraction angle measurements. 111
- 3.8. Calculated and measured maximum period variation along the x -axis of the flat- and curved-exposed substrates for the grating period varying from 500 nm to 1000 nm. The solid orange plot (▲) is the calculated maximum period variation, and the dotted plot (■) is the measured maximum period variation on the flat exposed substrates. The solid blue plot (●) is the estimated maximum period variation, and the dotted plot (■) is the measured maximum period variation on the curved exposed substrates. 113
- 3.9. A measured period variation on the x -axis of the flat exposed substrate with two LIL optical set-ups for the grating period of 500 nm. The orange plot (▲) is the period variation on the flat exposed substrate using a 442 nm LIL setup. The blue plot (●) is the period variation on the flat exposed substrate using a 266 nm LIL setup 115
- 3.10. A measured period variation on the x -axis of the curved exposed substrate with two LIL optical set-ups for the grating period of 500 nm. The orange plot (▲) is the period variation on the curved exposed substrate using a 442 nm LIL setup. The blue plot (●) is the period variation on the curved exposed substrate using a 266 nm LIL setup 115
- 3.11. Optical profilometry (a) measurement data of deformed 4-inch silicon wafer during the vacuum treatment. (b) Surface topography of the

wafer during the vacuum treatment. The maximum deflection at the center of the wafer is 1.10 mm	117
3.12. Optical profilometry measurement data of deformed 4-inch silicon wafer after the vacuum treatment for 30 minutes. The orange plot (▲) is the flatness of the wafer measured along the horizontal axis with a maximum deviation of 1.17 μm. The blue plot (●) is the flatness of the wafer along the horizontal axis with a maximum deviation of 0.80 μm	117
3.13. The working setup of adaptive wavefront interferometry	118
3.14. The surface deviation of the 4-inch substrate at the central period of 1000 nm was recorded by wavefront aberration measurement using a laser at $\lambda = 632.8$ nm (a) For flat exposed grating, P-V is 24.18λ , and the RMS value is 3.33λ . (b) For curved exposed grating, P-V is 8.22λ , and the RMS value is 1.31λ	120

List of Tables

1.1.	List of academic and industry partners with respective ESRs and their role in the GREAT project	29
1.2.	Summarized list of five different applications targeted in a GREAT project for three different laser systems	48
1.3.	Targeted performance of GWS for different applications in the GREAT project	54
2.1.	Optimized design parameters and fabrication tolerance of GWS for A3 and A4 applications	77
2.2.	Deposited multilayer stack on 2-inch diameter FS substrates for A3 and A4 applications	79
2.3.	LIL recipe with exposure dose and developing time information used to develop photoresist gratings on multilayer stack FS substrates for A3 and A4 applications	82
2.4.	List of fabricated GWS parameters and their deviation from the center of the substrate.....	93
2.5.	List of fabricated Si master parameters and their deviation from the center of the substrate	97
2.6.	Measured maximum period variation along the x -axis and the y -axis of fabricated GWS and Si master gratings for A3 and A4 applications	100
3.1.	Measured values of maximum period variation along the x -axis for flat and curved exposure on 4-inch silicon wafer substrates from 500 nm to 1000 nm central grating period settings using LIL setup at laser wavelength 442 nm with fiber arms	112
3.2.	Key differences between the two LIL configurations	114

General Introduction

This thesis framework is built as a part of the “Grating Reflectors Enabled Applications and Training (GREAT)” project (EU Research Framework Programme Horizon H2020 / Marie Skłodowska-Curie Grant Agreement n° 813159). The project aims at establishing a complete development chain for producing grating waveguide structure (GWS), which will be implemented in different laser systems to tailor the spectral [1,2], spatial [3,4], and polarization properties [4-7] of the laser beam. It is possible by collaborating with consortium partners involving 9 academic institutions and six industrial partners (<http://itn-great.eu/>). The project aims to deliver the best quality GWS by thoroughly navigating different stages of the development chain, such as the design, fabrication, and characterization, and finally, testing and implementing GWS in different laser systems. This thesis work focuses on the fabrication and characterization of GWS using the LIL technique as the GREAT ESR2 (Early-Stage Researcher 2) at Lab. Hubert Curien, Jean Monnet University (Saint Etienne, France).

GWS can be defined as a planar waveguide and a diffraction grating to give a resonant behavior [8]. The grating design and waveguide materials can tune the resonance’s wavelength according to the polarization state and the angle of the incident beam. Moreover, due to the potential to achieve very high diffraction efficiency [9, 10], GWS is a highly sought optical element in high-power laser systems [11-14]. The development of GWS with strong resonant behavior is essential in tailoring and shaping high-power

laser beams' polarization, spectral, and spatial properties [15-18]. Over the years, GWS has proven its performance in high-end laser applications such as spectral and polarization stabilization [19, 20], pulse compression [21-24], wavelength multiplexing [25, 26], and generating radial and azimuthally polarized beams [27-30]. Therefore, there is a strong demand for producing good quality GWS to achieve 99.9% efficiency in their optical performance.

The performance of GWS can be improved by carefully monitoring and controlling the fabrication process since the interference phenomena in the GWS are extremely sensitive to the geometrical parameter's deviation, such as the refractive index and thickness of the layers in the multilayers stack and the grating parameters (grating profile, period of gratings, grating depth, and Duty Cycle) [31]. In addition to the careful fabrication control, the materials used in GWS waveguides should have good resistance, i.e., a high laser damage threshold when implemented in high-power laser systems with a power of several kilowatts [32, 33].

This thesis aims to perform three tasks in realizing the grating structures. First, to establish a process flow of a fabrication technique called LIL with a direct patterning method to produce GWS for spectral and polarization stabilization and wavelength multiplexing in two different laser systems: diode lasers emitting at 976 nm and solid-state lasers emitting at 1 μm . Secondly, to establish a fabrication process flow to produce silicon (Si) master gratings using LIL. The last task is to quantitatively investigate the process of optimizing the uniformity of the grating period in the large area gratings on a 4-inch silicon substrate.

The thesis is organized as follows:

Chapter 1 starts with an explanation of the GREAT project's motivation and objectives. The structural scheme of partner organizations and early-stage researchers (ESRs) involved in delivering the project goal is presented. The next section introduces Grating Waveguide Structure (GWS) in detail, with a section on its importance and the recent advancements in the field of high-power laser applications. It is followed by a section explaining the working principle of diffraction grating elements and multilayer films. The chapter ends with the theoretical understanding of a GWS: a combination of diffraction grating elements integrated with multilayer stacked film.

Chapter 2 first presents the structural hierarchy in developing GWS from design to implementation. It contains a section listing the two tasks of this thesis work concerning the fabrication of grating structures using the LIL technique. Before the fabrication, the design of GWS is briefly presented with the designed parameters and their calculated diffraction resonance response. The agreeable simulated tolerance allowed during the fabrication of the designed GWS is presented. Firstly, the detailed fabrication process flow is established to produce GWS using the direct patterning method in LIL. Each step for fabricating GWS is explained by tabulating all the parameters' values during the fabrication process. Secondly, the fabrication process flow is established to produce Si master gratings. Fabricating silicon master gratings is motivated by its application as a stamp in the nano-imprint lithography (NIL) technique to produce GWS cost-effectively. The following section presents the geometrical characterization results (grating period, depth, and Duty Cycle) on fabricated GWS and silicon (Si) master gratings using atomic

force microscopy (AFM), scanning electron microscopy (SEM), and Littrow period measurement. The measured grating parameters are presented, and their deviations from the design grating parameters are discussed. The following section shows the optical characterization of a high-index GWS sample used for spectral stabilization for a solid-state laser at 1 μm . The diffraction efficiency (DE) of the GWs sample is measured for TE and TM -1st orders for the wavelength range 990 nm – 1060 nm, and preliminary results on the spatial scanning on a 2-inch GWS at 1030 nm are presented and studied. Based on the period measurements of GWS and Si master samples, the chapter ends with the need for investigation and reduction of the grating period variation.

The final chapter details the quantitative investigation of reducing the period variation of grating structures in 4-inch Si substrates. It introduces the two-spherical beam LIL setup and the theoretical basis to calculate the period variation on a flat exposed substrate. The section is followed by a substrate-bending approach to reduce the period variation proposed by Walsh and Smith [34] in 2001. The following section presents the experimental results of period variation of fabricated grating samples at different grating period settings with and without using the custom-made concave vacuum chuck of a radius of curvature of 100 cm. In the same section, the measured period variation results of two different LIL setups are presented and compared. The profilometry measurements were carried out on the Si substrate's surface with and without bending treatment to prove the successful bending process without damage caused to the substrate. Finally, the straightness of the grating lines in the flat and curved exposed substrates is evaluated using wavefront aberration interferometry.

At the end of the manuscript, a general conclusion on the Ph.D. thesis is presented, and perspectives are proposed to continue the project.

Chapter 1

Organizational and theoretical framework

1.1. The GREAT project

The importance of lasers in science and technology is a well-established fact, and now, lasers are found in many applications. Laser finds applications in imaging nano-scale featured particles to observe the chemical reaction in real time [36-40]. Laser applications are easily extended from detecting a weak gravitational force to helping satellites observe distant galaxies [41-43]. High-power lasers are also well developed and used in laser-material interaction research [44-46] and laser beam machining [47-50]. Lasers are also used in micro and nano-structuring, either as direct structuring or in lithography-based processes [51-58].

Adopting a laser in any targeted application depends on the ability to tailor the spatial, temporal, and spectral properties of the light in the laser system. One of the important optical key elements used to achieve the tailoring of light properties is diffraction gratings [59]. Diffraction gratings, combined with a planar waveguide, will be called Grating

Waveguide Structures (GWS). GWS is a very efficient solution for tailoring the spectral and polarization properties of laser- beams [15-16]. The GREAT project platform is built on developing GWS in high-power laser systems [11-14].

1.1.1. Objectives of GREAT project

The GREAT project establishes a complete development chain for producing GWS. It is made possible with a collaboration of consortium partners involving 9 academic institutions and 5 industrial partners, as detailed in table 1.1.

The 15 early-stage researchers (ESRs) are responsible for producing the GWS, starting from the conceptualization of the grating design to the fabrication and characterization of GWS and, at last, implementation and testing of gratings for their performance in different laser systems. The 15 ESRs in the GREAT project are hosted by the 9 academic institutions (<http://itn-great.eu/>). The GREAT project is defined by its research and training objectives to deliver the GWS.

- a) Research objectives – The project aims to establish a whole production chain from design to implementation of GWS in different high-power laser systems according to the end-user need and applications. To deliver high-efficiency GWS, the production process is carefully controlled, and their optical performance will be measured by developing precise measurement tools.
- b) Training objectives – The project will also aim to train the ESRs through hands-on experience in fabrication technologies, characterization tools, and instruments. By doing so, the ESRs can gain expertise in producing optical elements. They will be able to perform in a professional capacity and facilitate the advancement of technology in the laser engineering sector.

Beneficiaries and industrial partner	Department/ laboratory	ESR	Role in GREAT project
University of Stuttgart	Institute for laser tools (IFSW)	ESR 1	Design and characterization of GWS
		ESR 12	Testing and implementation of GWS
		ESR 13	
	Institute of applied optics (ITO)	ESR 8	Fabrication and characterization of GWS
University of Lyon	Laboratoire Hubert Curien (LabHC)	ESR 2	
University of Eastern Finland	Department of Physics and Mathematics	ESR 4	
		ESR 5	
AMO GmbH	AMO	ESR 3	
University of Southampton	Optoelectronics Research Centre	ESR 9	
		ESR 7	Thin film coatings
Ecole Centrale Marseille	Institut Fresnel (IF)	ESR 6	
		ESR 10	Laser-induced damage threshold analysis
Alphanov	Laser sources and components	ESR 11	Testing and implementation of GWS
Université Bordeaux	Laboratoire Ondes et Matière d'Aquitaine (LOMA)	ESR 14	
DILAS Diodenlaser GmbH	Beam sources department	ESR 15	
PI-Fibercryst SAS			End-users of GWS
TRUMPF Laser GmbH			
Modus Research and Innovation Limited			
Novae Laser			
Amplitude systems			

Table 1.1. List of academic and industry partners with respective ESRs and their role in the GREAT project

By defining the objectives of the GREAT project, the next step is to set up detailed working steps in the production and implementation of GWS involving the ESRs. The seven Work Packages (WP) that make the skeleton of the GREAT project are presented in Fig 1.1.

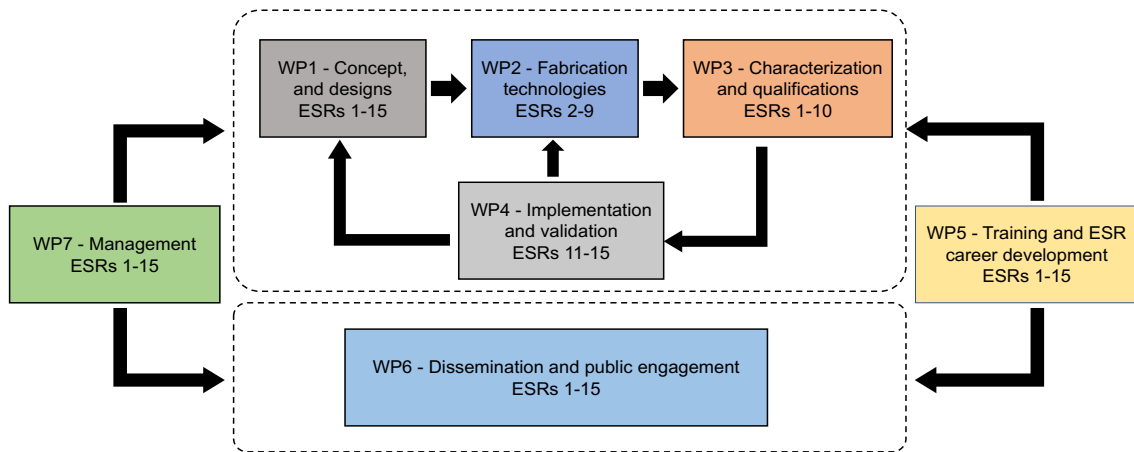


Figure 1.1. Seven work packages in establishing the GREAT project.

Fig 1.1 presents seven WPs establishing the production of GWS used for tailoring and beam shaping of the laser output in different high-power laser systems. The WP1 to WP4 involves the production of GWS, from the design of grating parameters and multilayers to fabrication and characterization of the structures and, finally the testing of their optical performance. The WPs 5-7 involves providing soft skill training to ESRs and the overall management of the project.

1.1.1.1. Concept, and designs (WP1)

In WP1, diffraction gratings are combined with planar waveguides to design the GWS with appropriate design parameters to achieve the highest diffraction efficiency (DE) at the different laser operating wavelengths. The theoretical simulations of GWS are carried out by ESR 1 using commercially available softwares, such as MC Gratings and Microsim, based on the RCWA algorithm. The design parameters are then provided to the WP2 team for the fabrication of GWS.

1.1.1.2. Fabrication technologies (WP2)

In WP2, the tasks are dedicated to fabrication technologies such as multilayer coatings, lithography techniques, and etching processes. ESRs 2-9 are responsible for the fabrication and characterization of GWS. Several coating techniques, such as Magnetron Sputtering and Pulsed Laser Deposition (specific to crystalline GWS), are used to fabricate multilayer stacks. The optimized optical monitoring technique will be developed in the GREAT project to precisely control the layer thickness. The multilayer stack is then patterned with grating structures using different lithography techniques like E-Beam lithography (EBL), Laser Interference Lithography (LIL), Scanning Beam Interference Lithography (SBIL), Stepped Mask Interference Lithography Exposure (SMILE) and Nanoimprint Lithography (NIL) as illustrated in Fig 1.2.

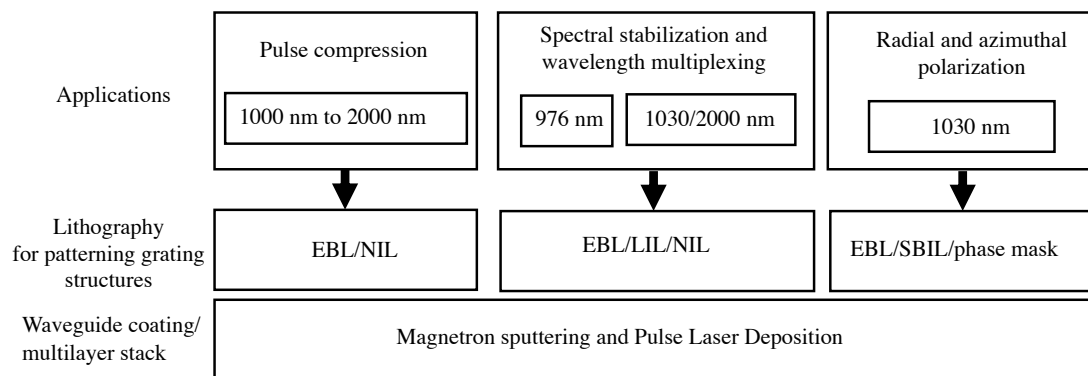


Figure 1.2. Overview of different fabrication techniques explored for producing GWS in a GREAT project.

The patterned grating structures are then submitted to etching processes using Reactive-Ion Etching (RIE), in which the layers of multilayer stacks are etched accordingly to the design parameters for each application. The project focuses on producing GWS by all the lithography techniques mentioned above and comparing the

quality of the grating structures in terms of uniformity of grating parameters. The most appropriate patterning technique is selected for each application (see table 1.2).

1.1.1.3. Characterization and qualification (WP3)

In WP3, the focus is on closely monitoring the geometrical properties and optical properties of the GWS to evaluate their quality before being used in each application. In particular, the geometrical properties of the grating structures are observed in each step during the fabrication process to monitor the grating parameters closely. The reason being the optical performance of the GWS is extremely sensitive to the deviation in grating parameters from the design. Several characterization tools are used for monitoring grating parameters, such as Atomic Force Microscopy (AFM), Scanning Electron Microscopy (SEM), optical profilometer, and ellipsometer. The ESRs 1-10 are responsible for carrying out the characterization of GWS (table 1.1). The optical performance of fabricated GWS will be evaluated by measuring the reflectivity, DE, wavefront aberration, and Laser-Induced Damage Threshold (LIDT). The evaluation of GWS for its optical performance is crucial before implementation in the laser systems for testing.

1.1.1.4. Implementation and validation (WP4)

In WP4, the GWS samples will be tested by implementing them in different laser systems for each application, as listed in table 1.1. The laser system is developed and optimized by ESRs 11-15. The functionalities of GWS inside the laser systems are then analyzed by their key performance indicators (KPI). The GWS for A1 and A2 applications (table 1.2) will be analyzed for their performance in terms of spectral bandwidth, compression efficiency, and pulse duration. The GWS for A3 and A4 (table 1.2) applications will be analyzed for their performance in terms of spectral bandwidth,

multiplexing efficiency, and second harmonic generation (SHG) efficiency. Finally, the GWS for the A5 (table 1.2) application will be analyzed for their performance in generating radial and azimuthally polarized laser beam shaping. The general targeted performance factors of GWS, such as their efficiency, LDIT, and peak power, need to be validated for each application. The variation in the measurements is investigated and provided to WP1 and WP2 to redesign and reoptimize the fabrication process to reach the targeted GWS performances.

1.1.1.5. Training of ESRs, public engagement, and project management (WP5-7)

WP5 to WP7 deal with the scientific for all the ESRs to reach expertise in producing complex optical elements and the ability to put the work experience into industrial use through soft skills training. The scientific training involves the presence of ESRs in workshops and tutorials related to the technology and analysis of optical elements. The soft-skills training involves creativity workshops and public engagement through conferences and industrial exhibitions.

Thus, the GREAT project is designed carefully to deliver high efficiency and to perform GWS for A1 – A5 applications (refer to section 1.3) in different laser systems, along with training the young researchers with the scientific skill set to gain expertise in the production of complex optical elements for a various application potential in the laser engineering sector.

1.2. Grating Waveguide Structures

This thesis work is built on the objective of developing the GWS by exploiting the resonance phenomena which occur in the coupling of mode in the waveguide medium of

the GWS. Before presenting the schematic representation of GWS, the theoretical principle behind the diffraction gratings and optical waveguides must be established.

1.2.1. Principle of diffraction gratings

Diffraction gratings are optical elements with a periodic refractive index variation through spaced grooves or alternating spacing of different mediums [60]. When the light is incident on such structures, the beam can be split into multiple directions, the diffracted orders, as seen in Fig 1.3. This unique spectral property of splitting the light into orders, reflected, or transmitted, is possible due to the periodic modulation of the surface index. If the modulation is aperiodic, the diffracted orders are not possible.

The simple grating's law [60] defines the angle of propagation and is written as,

$$k_m = k_{inc} + \frac{2\pi m}{\Lambda} \quad (1.1)$$

Where, $\|\vec{k}_m\|$ and $\|\vec{k}_{inc}\|$ are the free space and grating wavevectors, respectively. m denotes the diffracted order integer and Λ is the grating period. The wavevector $\|\vec{k}_m\|$ and $\|\vec{k}_{inc}\|$ are related to the wavelength of the incident light and the incident angle (θ_{inc}) in the refractive index n_a and diffracted angle (θ_m) in the refractive index n_w as,

$$k_{inc} = k_0 n_a \sin \theta_{inc} \quad (1.2)$$

and

$$k_m = k_0 n_w \sin \theta_m \quad (1.3)$$

Where, $\|\vec{k}_0\| = 2\pi/\lambda$ is the free space wavevector. By using Eq 1.2 and Eq 1.3 in Eq 1.1 the diffraction grating law is defined for both transmission and reflection as in Eq 1.4 and Eq 1.5, respectively.

$$k_0 n_w \sin \theta_m = k_0 n_a \sin \theta_{inc} + \frac{2\pi m}{\Lambda} \quad (1.4)$$

$$k_0 n_w \sin \theta_m = k_0 n_a \sin \theta_{inc} - \frac{2\pi m}{\Lambda} \quad (1.5)$$

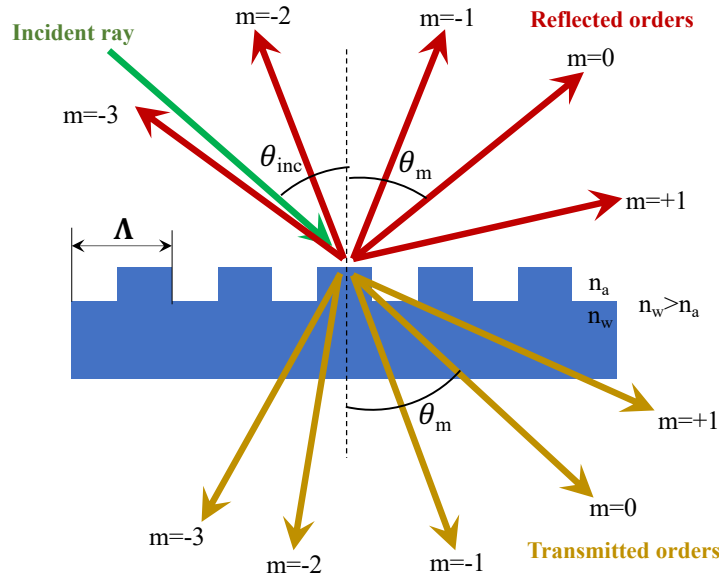


Figure 1.3. Schematic sketch of a diffraction grating of period Λ , and the incident light is split into m diffracted orders (reflected and transmitted orders).

For $m = 0$, the diffraction does not occur, and the surface acts as a non-periodic or plane surface. Diffraction orders occur for $m \neq 0$, and the diffracted angle depends on the wavelength of incident light and the refractive index of the incident and transmission mediums. Hence, this spectral property of diffraction gratings is used to separate different wavelengths of light, as each wavelength will have a different diffracted angle.

1.2.1.1. Diffraction orders and Ewald sphere

The diffraction gratings in real space can be graphically presented in its reciprocal space called the Ewald sphere [61]. The Ewald sphere demonstrates the relationship between the diffraction angle and the wavevectors of the incident ($\|\vec{k}_{inc}\|$) and diffracted

light ($\|\vec{k}_m\|$). The half-circle of the radius of $n_a k_o$ and $n_w k_o$ is drawn for the reflected orders into the n_a medium and transmitted orders into the n_w medium, respectively. When the light is incident with an angle normal to the grating surface ($\theta_{inc} = 0$), the diffracted orders are symmetrical with equal diffraction angles either in the reflection or transmission, as it is illustrated Fig 1.4(a). The reflected orders of the incident medium are denoted in red, and the transmitted orders propagating in the grating medium are denoted in orange (Fig 1.3). The real geometry of the diffraction grating for normal incidence and oblique incidence ($\theta_{inc} \neq 0$) and their equivalent conversion into reciprocal space, is shown in Fig 1.4(a-b) and Fig 1.5 (a-b) respectively. In the reciprocal space, the vertices coordinates are denoted by

$$\gamma_m = \|\vec{k}_0\| n_a \sin \theta_{inc} + \frac{2\pi m}{\Lambda} \quad (1.6)$$

The vertices coordinates are related to the incident angle, and the free space vector, as given in Eq 1.6., lies on the k_x axis. The efficiency of all the diffraction orders will be same in the case of normal incidence in reflection or transmission, considering a perfect symmetrical grating profile. When the incidence angle is oblique ($\theta_{inc} \neq 0$), in the incident plane shown in Fig 1.5 (a-b).

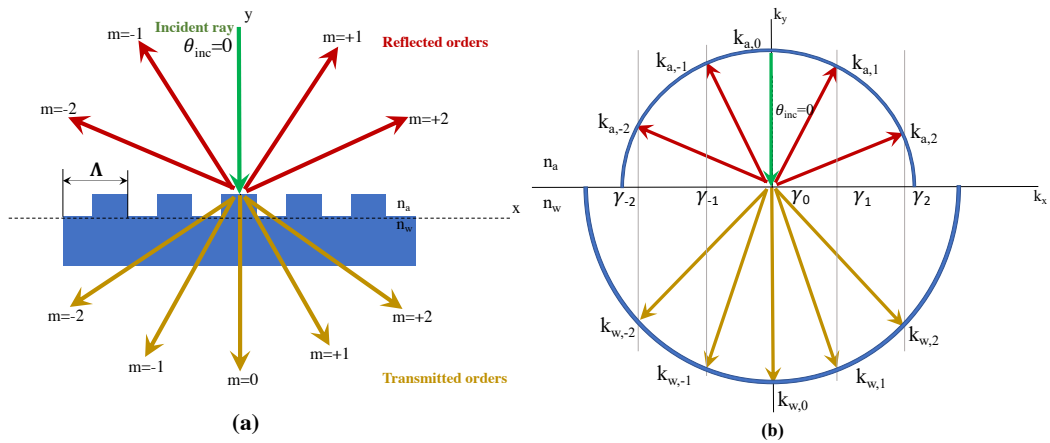


Figure 1.4. Representation of diffracted orders (reflection and transmitted orders) from the diffraction grating surface in (a) real geometrical space (direct space) and (b) reciprocal space (indirect space), also referred to as Ewald sphere for incident light at $\theta_{inc} = 0$ (normal incidence).

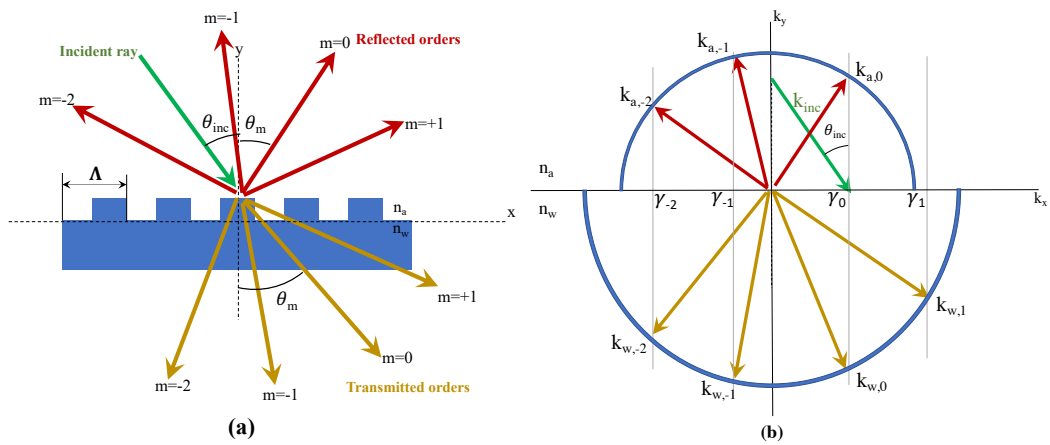


Figure 1.5. Representation of diffracted orders (reflection and transmitted orders) from the diffraction grating surface in (a) real geometrical space (direct space) and (b) reciprocal space (indirect space), also referred to as Ewald sphere for incident light at $\theta_{inc} \neq 0$ (oblique incidence).

1.2.2. Principle of the planar waveguide

An optical waveguide is a spatially inhomogeneous physical structure that can guide light [62], in propagative modes. The total internal reflection principle is obeyed in guiding light through the structure. A general waveguide structure consists of materials with different refractive indices, with light usually confined and guided in the higher refractive index region. Optical waveguides can be classified based on their geometry, mode structure, and refractive index [63]. The simplest optical waveguide structure is the planar waveguide, as shown in Fig 1.6 with propagation along z -direction.

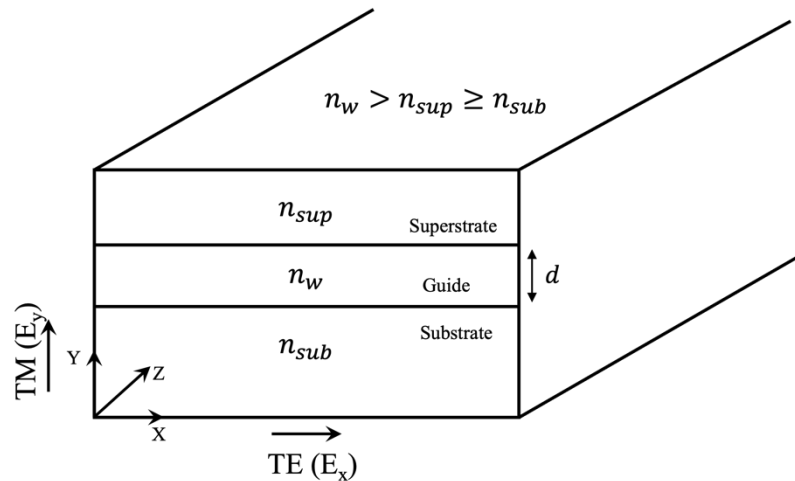


Figure 1.6. Schematic of dielectric planar waveguide [63].

It comprises a structure with infinite distance in the x - and z - directions and a guiding layer of thickness d surrounded by a superstrate and a substrate. It shows the variance of the refractive index in the y -direction. The index of refraction of the guiding medium, n_w , must be greater than that of substrate and superstrate, respectively n_{sub} and n_{sup} , for total internal reflection to occur at the interfaces. The back and forth of the light in the guide can be seen as the wave interfering with itself. Taking into account that the phase shift of the interfering waves, related to the difference in the optical path, but also the phase shifts

introduced during the total reflection at the interface substrate/guide and guide/superstrate must be a multiple of $2m\pi$, it can be shown that each mode exists if the following equations Eq 1.7 and 1.8 called dispersion equations, respectively for TE and TM polarization, accept the corresponding m integer (0, 1, 2 ...) as a solution.

$$m\pi = k_0 d \sqrt{n_w^2 - n_e^2} - \tan^{-1} \left[\frac{\sqrt{n_e^2 - n_{sub}^2}}{\sqrt{n_w^2 - n_e^2}} \right] - \tan^{-1} \left[\frac{\sqrt{n_e^2 - n_{sup}^2}}{\sqrt{n_w^2 - n_e^2}} \right] \quad (1.7)$$

$$m\pi = k_0 d \sqrt{n_w^2 - n_e^2} - \tan^{-1} \left[\frac{n_w^2 \sqrt{n_e^2 - n_{sup}^2}}{n_{sub}^2 \sqrt{n_w^2 - n_e^2}} \right] - \tan^{-1} \left[\frac{n_w^2 \sqrt{n_e^2 - n_{sup}^2}}{n_{sup}^2 \sqrt{n_w^2 - n_e^2}} \right] \quad (1.8)$$

The n_e is called the effective index and is an important characteristic of a guided mode. Indeed, it is directly linked to the propagation constant of the guided mode $\beta_m = k_0 n_e$. Both TE and TM modes can appear in a planar waveguide. The electric field component E_x in TE mode is parallel to the x-axis. In TM mode, the electric field component E_y is perpendicular to the plane interface.

1.2.3. Literature overview

After understanding the basic principle involved in diffraction gratings and the planar waveguide, the next step will be to improve the efficiency in a specific diffracted order. Very high efficiency is achieved by opting for sub-wavelength gratings in which the grating period is smaller than the wavelength of the incident light. Such gratings will eliminate the diffraction in higher propagative orders, and the beam can be redistributed only in the zeroth order and -1st orders. When this sub-wavelength grating is integrated

with the thin waveguiding film, the structure is referred to as Resonance Waveguide Gratings (RWG) or GWS, as shown in Fig 1.7.

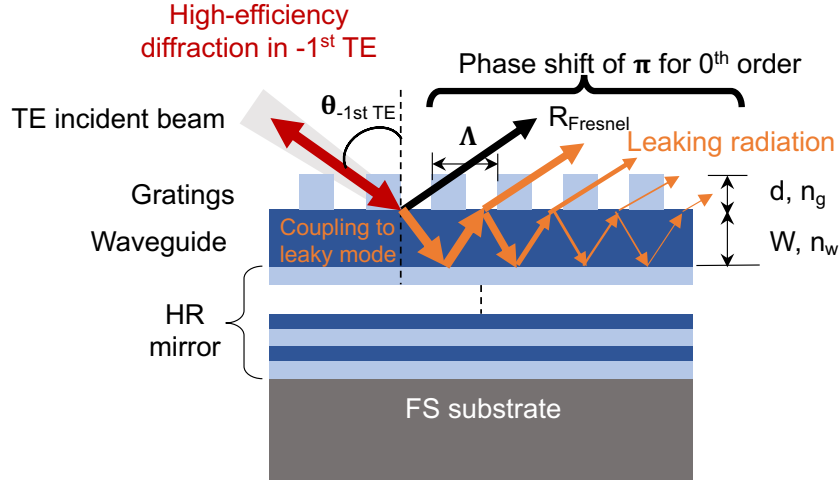


Figure 1.7. Schematic mechanism of resonance effect in GWS structures.

In 1960, grating couplers were used in place of prism couplers to couple the light on a thin-film waveguide for on-chip interconnects by Dakss et al. [64]. To couple a wave incident on a waveguide, the phase matching condition must be achieved, where the axial propagation constant of the guided mode in the waveguide β_m must be equal to the axial propagation constant in the superstrate media with refractive index, n_{sup} .

The coupling equation is then:

$$k_0 \cdot n_{sup} \sin \theta + \frac{2m\pi}{\Lambda} = k_0 n_e \quad (1.9)$$

Choosing the period and the angle properly makes it possible to have the phase-matching condition between the diffracted order and the guided mode, as seen in Fig 1.8(a-b).

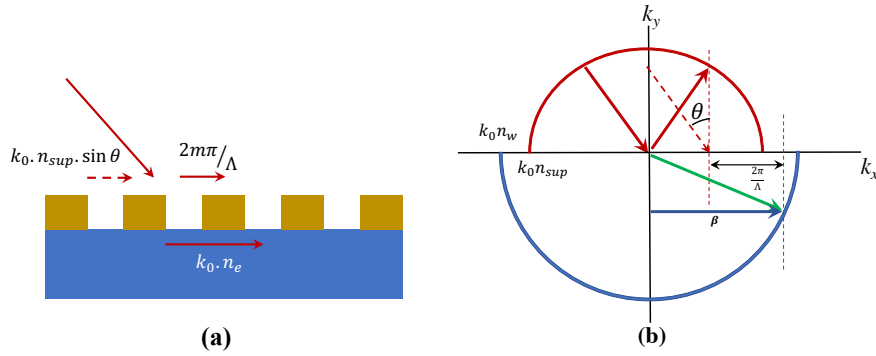


Figure 1.8. (a) Schematic mode coupling mechanism in the waveguide integrated with grating structures, (b) Ewald Sphere or reciprocal space representation of the mode coupling in the waveguide.

This work was followed by similarly demonstrating light coupling by using a hologram volume grating coupler made of gelatin by Kogelnik et al. [65]. These two demonstrations of using gratings to couple the light into the waveguide films paved the path in the 1970s to carry out detailed research to fully understand the efficiency of grating couplers integrated with dielectric waveguide films [66].

In GWS (Fig 1.7), the light will be coupled by the grating in the leaky mode inside the waveguide region. Some of the guided light is diffracted from the waveguide while propagating in the waveguide medium. This leaking radiation is coupled with noncoupled incoming light (reflected or transmitted). The recombination of this leaking radiation and the noncoupled light will produce very high reflection or transmission at a specific wavelength per the GWS parameters. Such high efficiency of resonance behavior can have linewidth at full width half maximum (FWHM) of 0.1 nm [67].

Indeed, destructive interference is possible either in the reflection or transmission due to the combining of leaking radiation and the noncoupled reflection and transmission waves dependent on the wavelength and the accumulative phase shift delay in the

waveguide. It is possible to achieve this resonant behavior by adjusting the excitation parameters. The GWS is also sensitive to the incidence angle and the wavelength with a value of 0.1° per nm of an angle-to-spectral linewidth ratio [68]. Hence GWS is an effective optical element in applications such as filtering and spectral stabilization in laser systems. Also, GWS is polarization selective and can be used as waveplates, polarizers, and depolarizers [69-75].

GWS can be appropriately designed and set up to have -1^{st} diffracted order in the same path as the incident light, referred to as Littrow configuration, to achieve high diffraction efficiency depending on the incident wavelength and polarization [76]. This high efficiency can be further designed to operate in reflection or transmission due to the dielectric material, which is usually used for waveguide thin films. GWS integrated with a multilayer stack of alternating dielectric thin films can make GWS mirrors with theoretical efficiency reaching 100% [77, 78]. Due to the dielectric material used in the GWS, they do not have a thermal heating issue, unlike the metallic grating structures, thus enabling GWS to be used in a vast variety of high-power applications such as intra and extra-cavity mirrors in laser systems [79]. GWS general structures with a periodic array of grooves on the waveguide film will make it a localized scattering element in which guided modes propagate and leak radiation. This behavior of GWS makes it a suitable optical element in applications like optical integrators for the temporal and spatial integration of incident beams [80]. This localized scattering can be further exploited in optical sensing and metamaterial studies [81-84].

GWS can be designed to have highly efficient filters operating in a very narrowband by using a grating with shallow grating depth, causing a weak in and out-coupling

efficiency [85], as shown in Fig 1.9 (a). The filter operation of GWS can be designed either in reflection or transmission. In one study, the GWS is theoretically designed to have 100% efficiency by having a symmetrical grating profile in either the vertical or horizontal direction [86], or by integrating the grating structures with a multilayer stack of quarter-wave thickness [87]. The GWS filters are characterized by their spectral response with a shape referred to as Fano lineshape [88, 89]. Recently, for a filter operation in the transmission regime, a narrowband filter was designed to have a high efficiency by demonstrating a two-crossed and spatially modulated GWS [90-92].

The wideband reflection operation of GWS was studied using a high-index dielectric layer on a lower-index layer [93, 94]. In another study, the reflector mirror in a partially etched GWS is tuned, as shown in Fig 1.9 (b-c), to operate in a border wavelength band with high efficiency by optimizing the grating profile such as the grating depth, thickness of the waveguide layer and with the trapezoidal sidewalls [95-97]. Fig 1.9 (b-c) shows the design simulation performed using RCWA of GWS to operate as broadband reflectors and the tuning process of wavelength range for different grating depths.

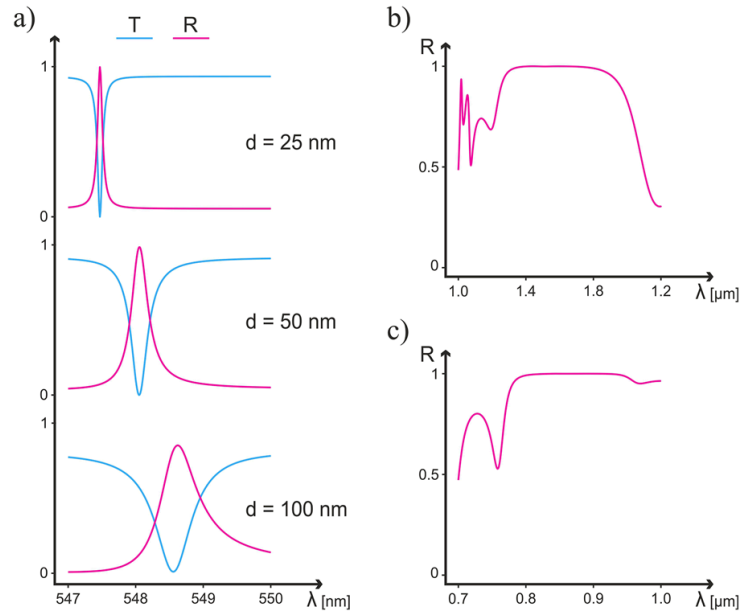


Figure 1.9. (a) Simulation of GWS using RCWA tuning the reflection bandwidth in TM polarization. The parameters used in the design are: $\theta = 15^\circ$, period = 400 nm, Duty Cycle (DC) = 0.5, the thickness of waveguide layer, $t = 300$ nm [85], (b, c) Simulation of GWS using RCWA for board band operation of GWS reflectors in the wideband IR wavelength range. (b) Parameters: $\theta = 0^\circ$, period = 700 nm, DC = 0.75, grating depth, $d = 460$ nm, $t = 840$ nm [95]. (c) Parameters: $\theta = 0^\circ$, period = 340 nm, DC = 0.68, $d = 220$ nm, $t = 2$ μm [96].

Further, a wideband reflector is designed to obtain sharp peaks of spectral response in the transmission regime by having GWS operate at the Rayleigh angle at which, the -1^{st} diffracted order is in Littrow condition [98]. The sharp variations in the spectral response of different diffracted orders by varying the wavelength are related to the Rayleigh angle (θ). Fig 1.10(a) shows the case study of a transmission wideband GWS filter working close to the Rayleigh anomaly in TM polarization [99]. In Fig 1.10(b-e), the electric field distribution of the study case for different wavelengths and incidence angles are reported. A resonance condition of the GWS is observed in Fig 1.10(c) for a normal incidence angle. However, in Fig 1.10(e) the rapid variation of efficiency from 0^{th} order to -1^{st} TM

order is observed, resulting in the complete transfer of energy from 0th order to 1st order by operating near Rayleigh anomaly.

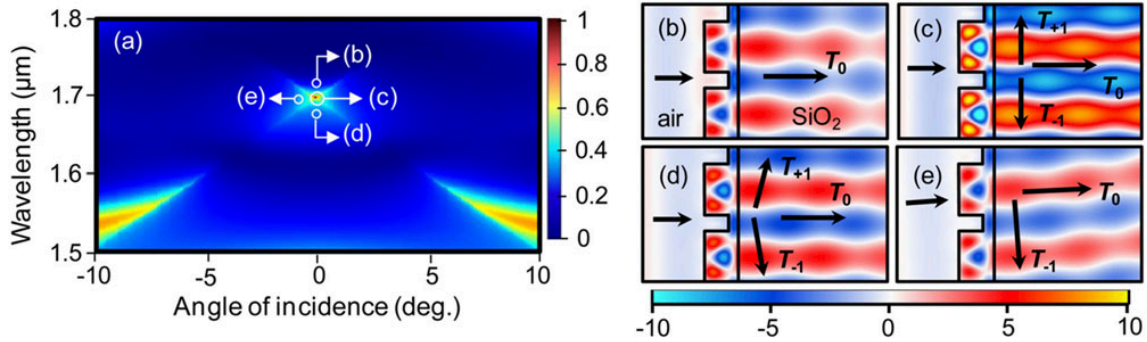


Figure 1.10. (a) RCWA simulation of a GWS transmission wideband filter operated at Rayleigh anomaly in TM polarization. Parameters used for the simulation are: period= 1130 nm, DC = 0.723, depth = 405 nm, the thickness of waveguide = 160 nm, (b–e) Electric field distribution for the case study near Rayleigh anomaly in TM polarization, (c) field distribution at resonance condition (e) strong transfer of efficiency from 0th order to first order which resulted in the dip in the transmission of 0th order [99].

GWS structures can be implemented in filtering with modification of the resonance behavior in conditions dependent on temperature. In one such study, the GWS filter was implemented to achieve the resonance shift in its spectral response. The GWS was fabricated using a soda-lime material with a graded-index profile. The resonance wavelength shift of 13 pm/K was observed [100]. The resonance shift was increased using a GWS developed with Si material and the shift of 0.12 nm/K was recorded using Joule heating arrangement as shown in Fig 1.11 [101]. The arrangement consists of placing Si GWS on an aluminum plate and is connected to the heating system through contact pads. The thermal response was doubled with a shift of 0.268 nm/K using a polymer-based GWS on a BK7 substrate [102].

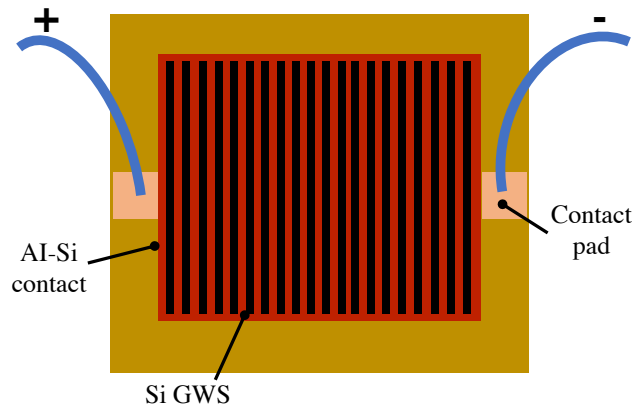


Figure 1.11. Schematic in the top view of GWS used in thermos-optic tunable filtering by Joule heating arrangement.

GWS is a potential optical element used recently to perform filtering operations in the laser cavity [103-106]. The cavity resonator has been studied and reported to show the advantages of GWS over the conventional multilayer Distributed Bragg Gratings (DBG) in terms of their fabrication and compactness [107] due to the smaller number of deposited thin-film layers reaching the same quality factor. The GWS mirrors can also be designed to achieve very narrow spectral response linewidth compared to mirrors available in the market, such as Fabry-Perot mirrors [108, 109]. The GWS mirror proves its advantage by having low mechanical losses due to the lower thickness of the overall structures and low thermal noise. Hence, GWS are also implemented in detecting weak gravitational waves where the main challenge is the cavity mirrors noise [110, 111]. Several fabricated configurations of GWS mirrors are reported in Fig 1.12(a-b), such as T-like GWS structures with silicon on a silica platform [112] and single silicon crystal monolithic GWS mirrors [113].

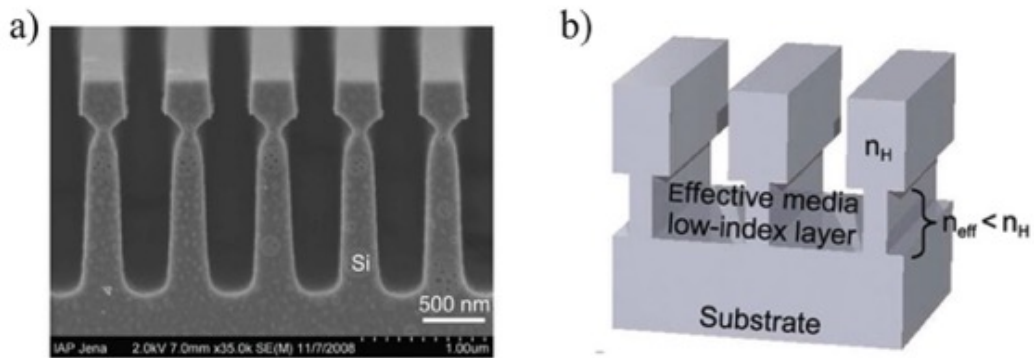


Figure 1.12. (a) SEM image of a T-like GWS structure with silicon on silica substrate [112]. (b) Schematic of a single silicon crystal GWS mirror [113].

The combined effort of understanding the nature of the materials used and knowledge about the guided resonance modes will open new opportunities for implementing GWS in future research. The vast range of spectral properties of GWS in different applications, along with the development in fabrication technologies, makes GWS exciting research possibilities and industrial applications.

In the GREAT project, the aspect of GWS as a cavity mirror in high-power laser systems to tailor the spectral, spatial, and temporal properties of the laser output is explored and completely investigated to evaluate their potential from the design to the fabrication. Such a complete evaluation of GWS in the wide field of high-power lasers has never been studied to our knowledge.

1.3. Targeted Applications

In the GREAT project, the GWS is implemented in different laser systems, such as a diode laser emitting at 976 nm, solid-state lasers like Yb: YAG thin-disk lasers emitting

at 1030 nm, and Tm-doped fiber lasers at 2000 nm. The GREAT project aims to deliver high-efficiency GWS for five different applications, as listed in table 1.2.

Targeted application of GWS	Type of the laser system	End-user applications
A1 – Pulse compression	Yb: YAG thin-disk lasers at 1030 nm	Micro materials processing, chirped pulse amplification
A2 – Pulse compression	Tm-doped fiber lasers at 2000 nm	Micro materials processing, chirped pulse amplification
A3 – Spectral stabilization and wavelength multiplexing	Diode lasers at 976 nm	Direct-diode-laser macromaterials processing
A4 - Spectral stabilization and wavelength multiplexing	Yb: YAG thin-disk lasers at 1030 nm	Macro materials processing and space debris removal
A5 – Generation of radial and azimuthal polarized beams	Yb: YAG thin-disk lasers at 1030 nm	Medical imaging, free space communication technology

Table 1.2. Summarized list of five different applications targeted in a GREAT project for three different laser systems.

1.3.1. Pulse compression for solid-state laser (A1-A2)

In A1 - A2 application, the GWS is used in developing the pulse compressors for solid-state laser systems emitting at 1030 nm and 2000 nm. The sketch of pulse compression using two pairs of parallel GWS is shown in Fig 1.13.

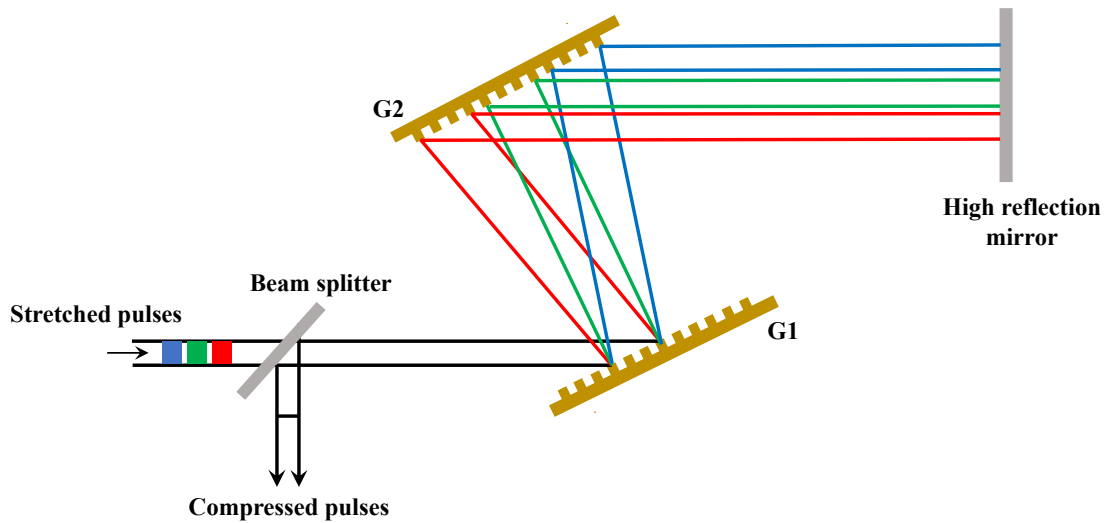


Figure 1.13. The configuration of pulse compression using G₁-G₂ GWS pair.

The pulse compression gratings' working principle involves expanding the phase shift's frequency dependence as far as the quadratic frequency term [114]. The pair of GWS arranged parallel with their grooves facing each other would exhibit a property of introducing time delay as a function of the wavelength [115]. The spectral energy of the laser pulse is evenly distributed between its amplitude and phase functions. The GWS pairs will redistribute the spectral energy between these two functions resulting in total spectral energy unchanged. The GWS pair is set up to work in the off-Littrow configuration in the -1st order. In this case, the angle of the reflected -1st order corresponds to the angle of the incident beam. The GWS developed in the GREAT project is aimed to exhibit a high DE of 99.9 % in the -1st order. This excellent optical performance results from combining the high reflection (HR) multilayer coating and optimized grating parameters. The commercially available compressors in the market use gold-coated grating mirrors or transmission gratings with an efficiency of 80-95% [116]. A trapezoidal grating-shaped mirror reported by M. Perry et al [117] has a DE higher than

95% and an LIDT ≥ 1 J/cm². Until recently, the GWS with DE of around 99.7% and LIDT of 0.5-0.6 J/cm² has been experimentally demonstrated by the partners in the GREAT project L. Gallais et al. [33]. The low LIDT issue will be solved in this project by using suitable coating materials with high LIDT and with proper grating design to minimize the field intensity at the grating lines and by minimizing the propagation length of the excited mode into the multilayer stack.

1.3.2. Spectral stabilization and wavelength multiplexing for diode and solid-state lasers (A3-A4)

In A3 – A4 applications, the GWS are designed and developed to spectrally stabilize the laser beams and in power scaling the laser output in diode laser emitting at 976 nm and in solid-state laser emitting at 1030 nm and 2000 nm. In today's industry, spectral stabilization in high-power diode lasers is achieved by Volume Bragg Gratings (VBG) [118-120]. However, the GREAT project aims to develop GWS to perform a similar spectral response as VBG but with a broader angular response [121]. The developed GWS can be implemented as intra-cavity end mirrors made to operate at a Littrow angle, as shown in Fig. 1.7, and reflects 99.9% of the light in -1st order back into the resonator resulting in high wavelength selectivity.

Moreover, the need to power scale the diode laser is motivated by the demand for high-power lasers in metal-cutting industries. The schematic configuration of wavelength multiplexing is shown in Fig. 1.14.

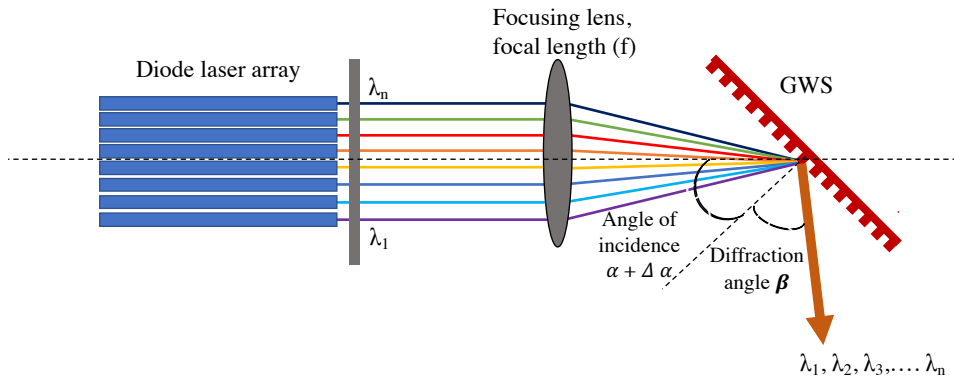


Figure 1.14. Schematic configuration of wavelength multiplexing of diode laser array by using GWS to combine the wavelengths ($\lambda_1, \lambda_2, \lambda_3, \dots, \lambda_n$) from n number of diode lasers using a focusing lens.

In the GREAT project, the developed GWS will be able to multiplex the output of several diode lasers in achieving laser power of several kW levels by maintaining good beam quality and overall efficiency above 95%. For solid-state laser systems, spectral stabilization is achieved using polarizers and etalon [122, 123]. However, the drawback of this combination is that they suffer from thermal losses at high power arrangements. In solid-state lasers, the GREAT project aims to provide GWS to combine multiple laser sources to achieve a 0.5 kW output power level with an efficiency above 95%.

1.3.3. Generation of radial and azimuthally polarized beams in thin-disk lasers

(A5)

A5 application involves developing GWS to generate radially and azimuthally polarized laser beams emitting at 1030 nm in solid-state lasers. The radially and azimuthally polarized beams have a great demand in laser material processing, optical tweezing, and light trapping [124-128]. The GREAT project addresses intra-cavity and extra-cavity approaches for generating and converting high-power laser beams with

azimuthal and radial polarization. Fig 1.15(a-b) shows the intra-cavity approach to generate both polarizations. The polarization function is achieved by implementing the GWS with circular grating lines as the cavity end mirror or as the output coupler. The polarization is filtered out by achieving a large reflectivity difference between the filtered-out polarization states and the lasing state [129]. This is made possible by the coupling behavior of GWS when the incident beam is coupled in the leaky modes in the multilayer substrate filtering out the polarization [7].

For this application, the GREAT project uses crystalline films of Yttrium Aluminium Garnet (YAG) & Gadolinium Gallium Garnet (GGG) due to their high thermal conductivity even at high-power laser operation. To develop crystalline GWS, the crystalline films are deposited by pulsed laser deposition (PLD) and combined with sub-wavelength grating patterning and etching on the deposited film.

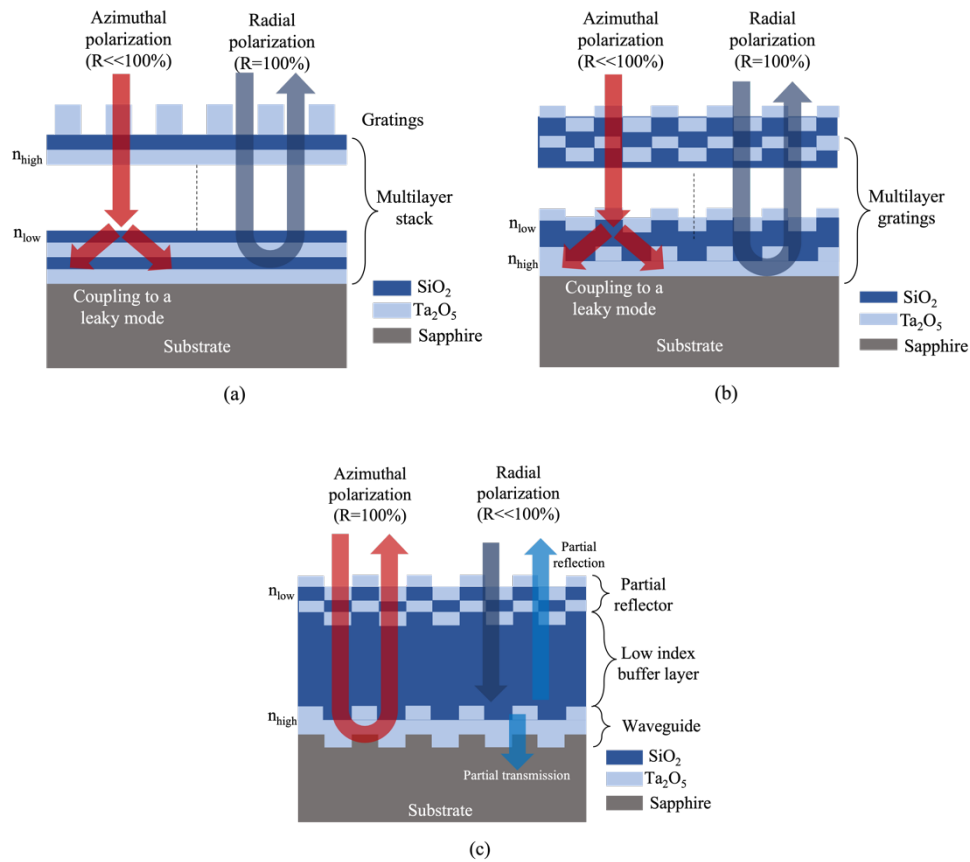


Figure 1.15. GWS schematic mechanisms developed in the GREAT project for generating azimuthal and radial polarization with a multilayer structure substrate of alternating $\text{Ta}_2\text{O}_5/\text{SiO}_2$ layers. (a) GWS structure to generate radial polarization with circular grating lines etched on multilayer stack (b) GWS structure to generate radial polarization with circular grating lines on Ta_2O_5 layer with multilayer deposited on the grating lines resulting in the multilayer grating profile. (c) Crystalline GWS structure generates azimuthal polarization by etching grating lines on sapphire substrate and depositing multilayers.

The conversion mechanism of laser beam polarization from linear to radial state is presented in Fig 1.16. The extra-cavity approach is developed for the conversion of linear polarization of the laser beam into radial polarization using segment gratings by the form-birefringence effect with variation in the orientation of the grating lines in the in-plane substrate axis per segment [130-132].

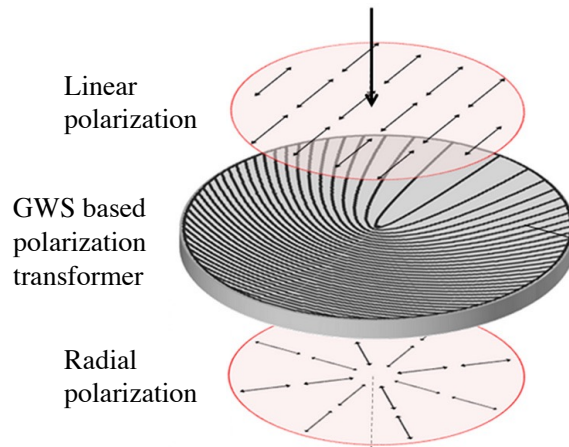


Figure 1.16. Transformation of linear polarization to radial polarization using segmented GWS [132].

The summarized list of the targeted performance of the GREAT applications with the GWS is presented in table 1.3.

Application	Emitted laser wavelength	Efficiency of GWS	Laser output power	LIDT
A1	1030 nm	$\geq 99\%$	$\geq 1\text{mJ}$	$\geq 1\text{ J/cm}^2$
A2	2000 nm	$\geq 99\%$	$> 2\text{mJ}$	$\geq 0.2\text{ J/cm}^2$
A3	976 nm	$\geq 99.9\%$	$\geq 1\text{ kW}$	$\geq 100\text{ kW/cm}^2$
A4	1030 nm 2000 nm	$\geq 99.9\%$ $\geq 99.9\%$	$\geq 1\text{ kW}$	$\geq 200\text{ kW/cm}^2$ $\geq 40\text{ kW/cm}^2$
A5	1030 nm	For intra cavity (IC) mirrors $\geq 99.9\%$ For extra cavity (EC) mirrors $\geq 90\%$	$\geq 1\text{ kW}$	IC: $\geq 200\text{ kW/cm}^2$ EC: $\geq 10\text{ kW/cm}^2$

Table 1.3. Targeted performance of GWS for different applications in the GREAT project.

1.4. Laser interference lithography (LIL)

1.4.1. Overview of maskless lithography techniques

Several fabrication techniques to pattern micro and nanostructures have been established over the years. Some of the well-known techniques include EBL, SBIL, and

NIL. EBL technique is the maskless lithography (Fig 1.17), which uses a focused beam of electrons to write an arbitrary shape on a substrate coated with negative or positive resist film sensitive to electrons [133-135]. The benefit of EBL is its capacity to write custom shapes of sub 10 nm with high resolution [136, 137]. But EBL exhibits low throughput, increased writing time, and suffers from fabrication errors like stitching and proximity effects [136].

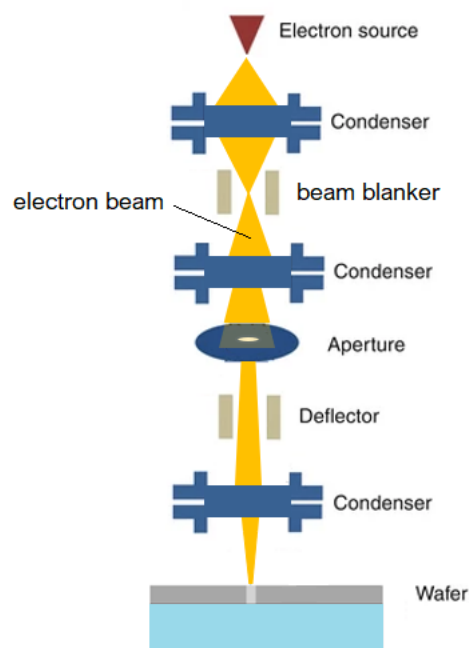


Figure 1.17. Schematic illustration of the EBL process. The electron beam is focused on electron sensitive resist layer for the patterning of nanostructures.

The Scanning Beam Interference Lithography (SBIL) technique is another maskless photolithography, as in Fig 1.18(a-b), that uses interference fringes formed by two small-diameter laser beams [138]. The patterning is then the matter of scanning the small area interference fringes across the substrate area. The benefit of SBIL is that it can pattern large-area grating lines with high precision and phase accuracy at the nanometer level at high speed [139]. However, the SBIL process faces the major challenge of locking the

interference fringes when moving the substrate resulting in spatial phase and stitching errors [140, 141].

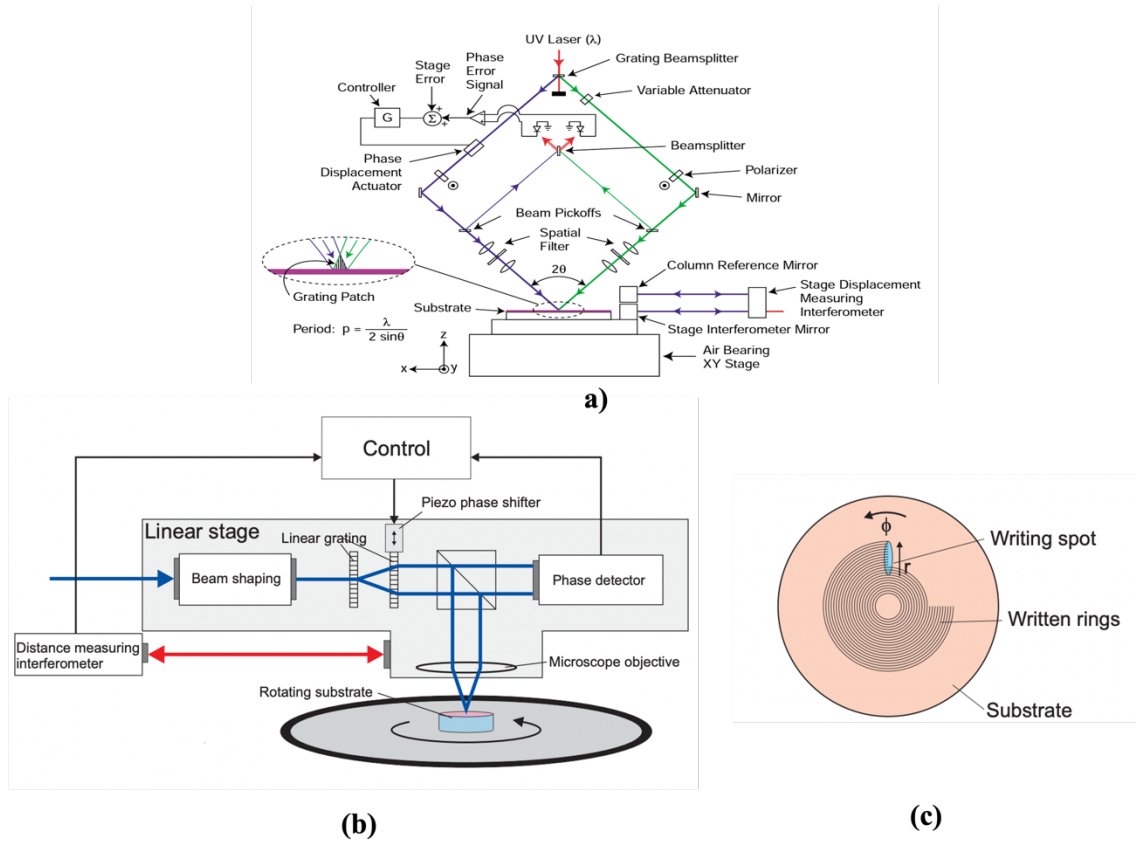


Figure 1.18. (a) Schematic of the SBIL system [138] (b) Illustrates the SBIL process setup for patterning circular gratings. (c) The substrate stage is rotated, resulting in the ring patterns of gratings [142].

The Nano-Imprint Lithography (NIL) process is a mask-assisted imprint process in which the gratings and nanostructures are printed on the resist-coated substrate using a hard mask commonly referred to as master [143] (Fig 1.19). The benefits of NIL are the high throughput and fast printing time with the mass production of nanostructures [143]. The NIL process will still depend on the maskless lithography techniques to receive the

perfect master, considered a key element required for the printing. This printing technique also faces random bald spots in the substrate with no imprinted structures [144, 145].

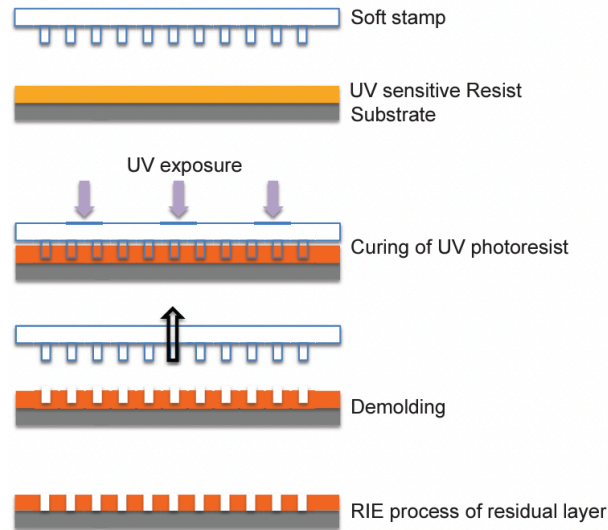


Figure 1.19. Principal steps involved in the NIL patterning process [145].

Laser Interference Lithography (LIL) is a maskless, simple technique with fast patterning time that is well-known and has been used for several decades to pattern periodic nanostructures [147-150]. The LIL technique offers excellent flexibility in terms of the patternable sample size. The setup can be easily built with basic optical resources such as a laser source, optical lens/fiber mirrors, and beam splitter. The LIL technique can accommodate one to several beams to create the interference fringes [151]. Although, over the years, LIL setup with multiple laser beams (up to six beams) has been studied and presented [152]. These complicated setups aim to improve the intensity distribution and contrast to obtain fine detail in the topography of structures. The complex LIL setups with multiple beams face the major challenge of using many optical elements and adding the noise generated in producing the fringes distribution. The simple and most common

LIL configurations are a two-beam LIL interferometer and Lloyd's interferometer [153], as presented in Fig 1.20(a-b).

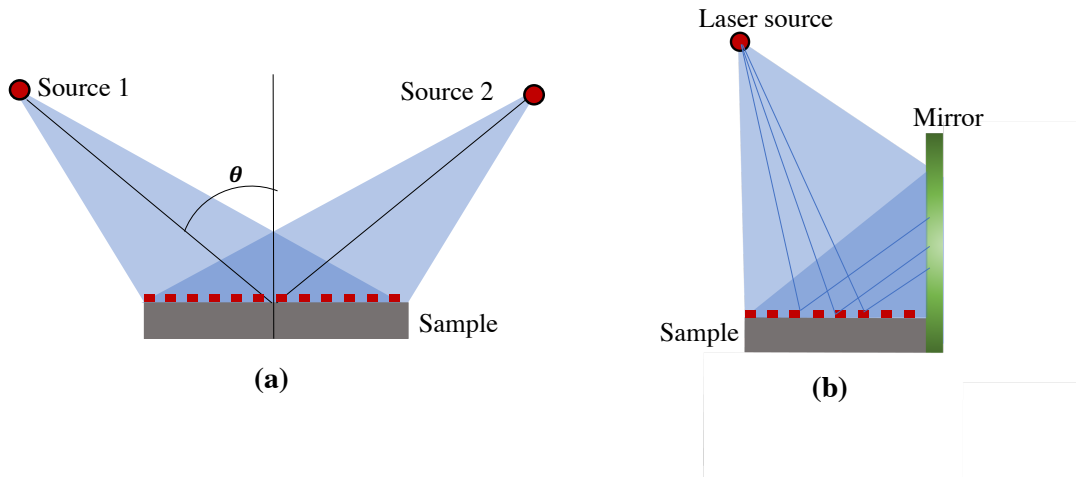


Figure 1.20. LIL setups with interferometry arrangement. (a) Two-beam LIL interferometer, (b) Single-beam interferometer (Lloyd's interferometer).

In Lloyd's interferometry configuration (Fig 1.20b), the interference fringes are formed by the laser beam interfering with itself upon the reflection from the plane mirror. This configuration is simple and offers relaxation with fringe stabilization, and the grating period can be easily changed by rotating the mirror. However, Lloyd's setup requires a bigger mirror to record the pattern on a large substrate and highly depends on the quality of the plane mirror. In a two-beam LIL interferometer configuration, the laser beams from two-point sources are combined to form the interference fringes at a half angle θ . The advantage of a two-beam LIL setup is its capacity to pattern grating structures on large substrate areas and the more straightforward modification of the wavefront of the beams to tailor the intensity distribution of the interference fringes.

The two-beam setup with two laser point sources will have a diverging beam with spherical wavefronts, as seen in Fig 1.21(a). When these spherical wavefronts are

combined, the interference fringes formed will have a hyperbolic distribution of gratings lines. This effect is due to two factors. First, the interference angle at each point on the sample changes and increases when moved away from the center of the substrate. Secondly, the fringe inclination causes the low contrast of the fringes away from the center of the substrate. These two factors will result in the grating structures with varying both grating periods and Duty Cycles. For very large distances, the spherical beams can be approximated to exhibit planar wavefronts. However, this approximation is limited by the physical dimension of the LIL setup. The merging of two spherical wavefronts will result in the gaussian intensity distribution interference fringes, which result in a nonuniform depth of energy penetration in the photosensitive resist layer during the LIL exposure process.

The LIL setup with interference fringes formed by two collimated beams (Fig 1.21b) will improve the uniformity of intensity distribution with even energy penetration during the LIL exposure process [154]. The collimated beams will also result in patterning near-linear grating lines. The grating lines are linear; however, they depend significantly on the optical elements' quality in generating collimated beams [155]. Depending on the quality of optical elements, noises can arise during the LIL process, which affects the fringe distribution during exposure.

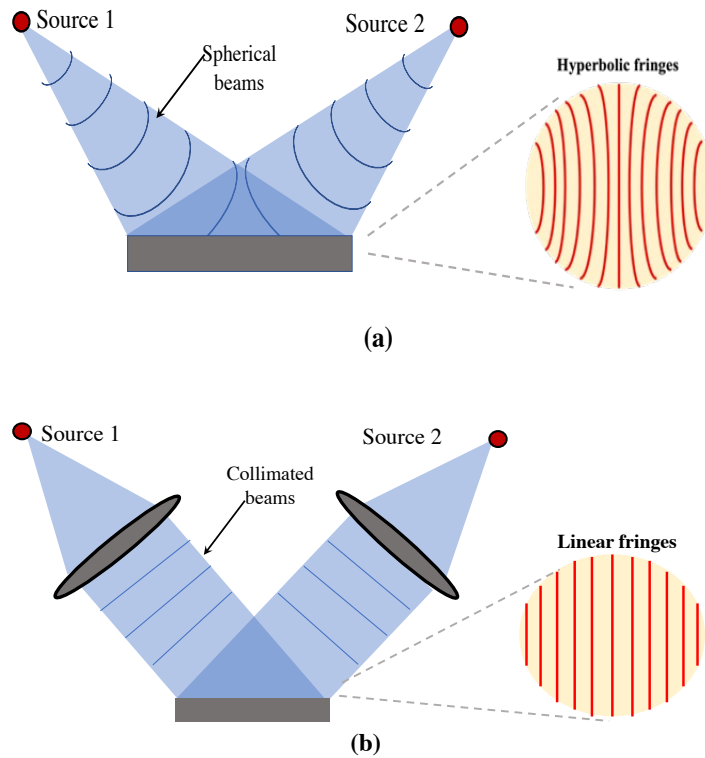


Figure 1.21. Interference fringes formed two different LIL setups with, (a) Two-spherical beams resulting in the hyperbolic fringe patterning. (b) Two collimated beams resulted in the near-linear fringe patterning.

1.4.2. Two-beam spherical LIL configuration

In this thesis, the patterning of grating structures on Fused Silica (FS) substrates and Si substrates is performed using a two-spherical beam LIL configuration, as shown in Fig 1.22. The configuration uses very few optical elements making this setup easy to build and control for different exposure settings and modifications. The laser beam is emitted from the continuous wave (CW) HeCd laser source at 442 nm. The laser beam is reflected by a plane mirror toward the 50/50 beam splitter, which splits the beam into two parts of equal power.

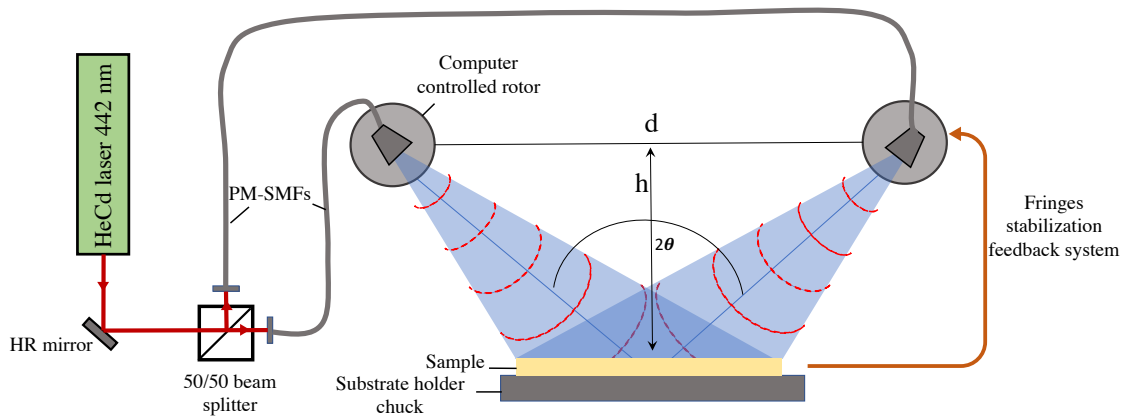


Figure 1.22. Schematic configuration of the two-spherical beam LIL setup used for the grating patterning GWS and Si masters (Nano Saint-Etienne platform, France). The spherical-beam interference fringes are of hyperbolic shapes due to the fringe inclination, and the interference angle changes when moved away from the center of the substrate (h).

The laser beams are fed into the polarization-maintaining single-mode fibers (PM-SMF). The output of fiber arms is mounted on the stepper motors, which is fixed with distance, $d=65$ cm, controlled by a LabVIEW software program. The program assigns the rotation angle to the stepper motors respective to the set period of the grating structures. The beams emerging from the two fiber arms diverge and are recombined at the substrate holder forming the interference fringes in the overlapping of the two incoming beams. The interference angle 2θ is calculated by the computer program for the specific grating period setting.

Fringe stabilization is crucial during the LIL exposure to avoid low-contrast grating lines due to fringe vibrations. The LIL setup is provided with the active fringe stabilization system (Fig 1.23), which consists of photodiode detectors connected to an active fringe stabilizer which in turn is connected to the piezoelectric mirror mounted on one of the fiber arms.

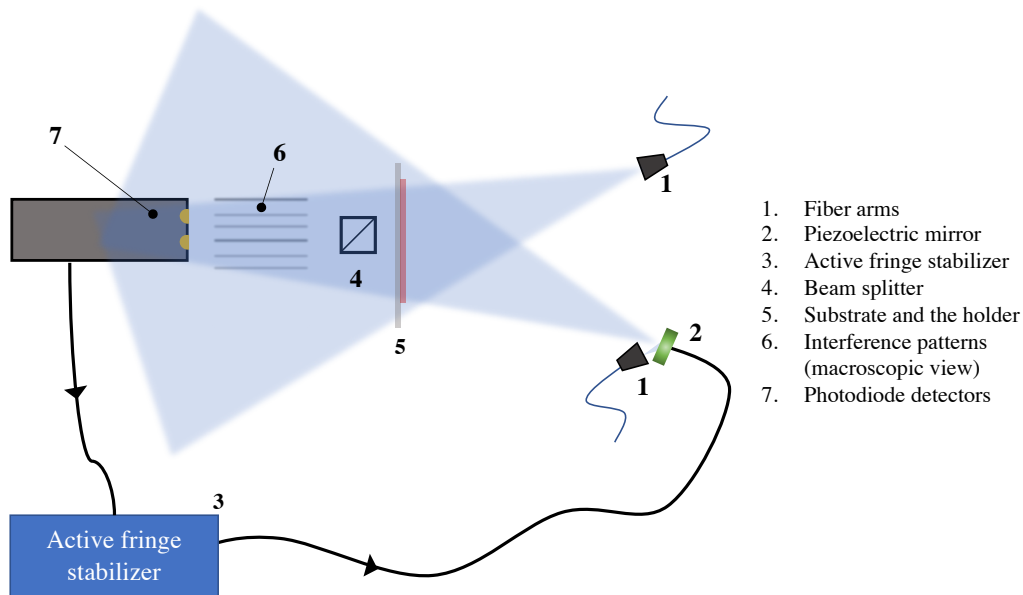


Figure 1.23. Schematic of active fringe stabilization setup.

Any vibrations in the surroundings during the LIL exposure will move the interference fringes, this movement is detected by photodiode detectors and this vibration signal is used for the active stabilizer making stabilized fringes during the exposure. The active fringe stabilizer sends the corresponding electric signal to the piezoelectric mirror, which adjusts the horizontal movement of the mirror, compensating for the difference in the optical path difference of one of the beams resulting in the fringes locked in during the patterning process.

The interference fringe pattern is recorded on the substrate using a photosensitive material solution called photoresist layer. The role of beam splitter is to aid in visually observing the fringes and adjust them to overlay on the photodetectors. Because of the specific chemical composition, the photoresist exhibits a solubility that varies upon receiving the appropriate energy dose from the laser interference fringes. The photoresist is differentiated into positive and negative photoresists based on their solubility in the

developer solvent (Fig 1.24) after being spatially UV illuminated. The positive photoresist exhibits increased solubility in the area under the exposure. In contrast, the negative photoresist will have low solubility under the exposure. Both positive and negative photoresist materials are used in patterning micro- and nano-structures in the semiconductor industries.

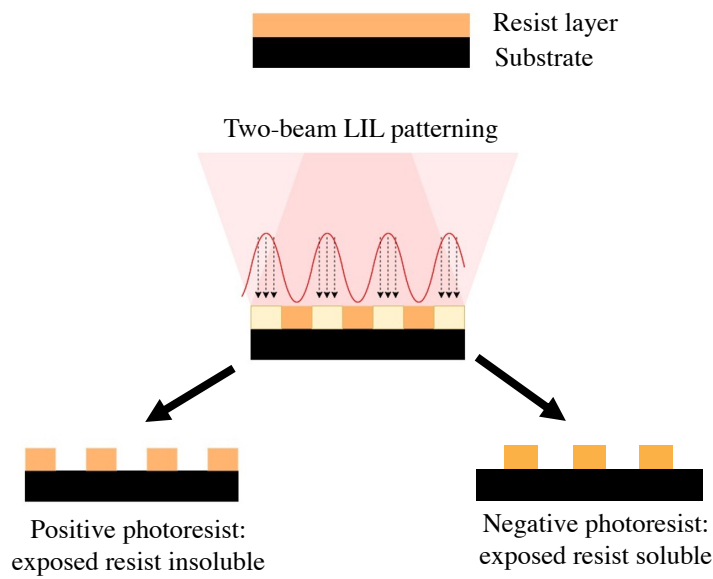


Figure 1.24. Interference pattern recording mechanism in the positive and negative photoresist-coated substrate.

To achieve grating lines for a specific set of parameters, the three important factors in the LIL process are interference angle, exposure energy dose, and development time. The interference angle is controlled by the computer program and depends on the wavelength of the laser source and the set period of the grating lines by Eq 1.10,

$$\Lambda = \frac{\lambda}{2 \sin \theta}, \quad (1.10)$$

Where Λ is the grating period, λ is the wavelength of the laser source, and θ is the half interference angle of two beams. The exposure dose is the power received by the photoresist layer during the patterning process. The exposure energy dose (J/cm^2) is related to the power received at the substrate (W/cm^2) and the exposure time (sec) as given by Eq 1.11,

$$\text{Exposure dose } \left(\frac{J}{cm^2} \right) = \text{Power } \left(\frac{W}{cm^2} \right) \times \text{exposure time (sec)} \quad (1.11)$$

The exposure dose of an exposed substrate can be varied by either changing the laser power or varying the exposure time. The photoresist will start soluble in the developing solvent for the exposure dose above the activation dose. Above the activation dose level, the photoresist becomes soluble/insoluble in the developing solvent - specific to the positive/negative resist.

1.5. Conclusion

In this chapter, the overview of the GREAT project is presented concerning the work packages considered to deliver the GWS for five different applications (A1-A5) in three different laser systems with a diode laser emitting at 976 nm, solid-state thin-disk and fiber laser emitting at 1030 nm and 2000 nm wavelength respectively. The theory of GWS is explained with the help of the diffraction grating principle and representation of diffracted orders in reciprocal space called Ewald Sphere. The historical overview section details the recent advancements of GWS in laser and optical applications. The targeted applications in the GREAT project are listed, and their working mechanisms are detailed.

Finally, the theory of the LIL technique is described, starting from the LIL basics, and presenting the schematic configuration of the LIL exposure setup, which constitutes the main thesis work to fabricate GWS and Si masters, which will be presented in chapter 2.

Chapter 2

Fabrication and characterization of grating structures

2.1. Introduction

The main goal of the GREAT project is to produce GWS to be implemented in different laser systems, such as diode laser emitting at 976 nm and solid-state laser emitting at 1030 nm and 2000 nm, for three main applications. The first application is for pulse compression in laser systems emitting at 1030 nm (A1) and 2000 nm (A2) [3, 4, 21, 32]. The second application is for spectral stabilization and wavelength multiplexing for diode lasers emitting at 976 nm (A3) and solid-state lasers emitting at 1030 nm and 2000 nm (A4) [6, 121]. The third application (A5) is to generate Cylindrical Vector Beams (CVB) with radial and azimuthal polarization in continuous wave (CW) and mode-locked Yb: YAG thin-disk laser systems [5, 28, 129, 132]. Fig 2.1 shows the overview of the research methodology with the four different work packages of the GREAT for the fabrication of GWS for the above-mentioned applications.

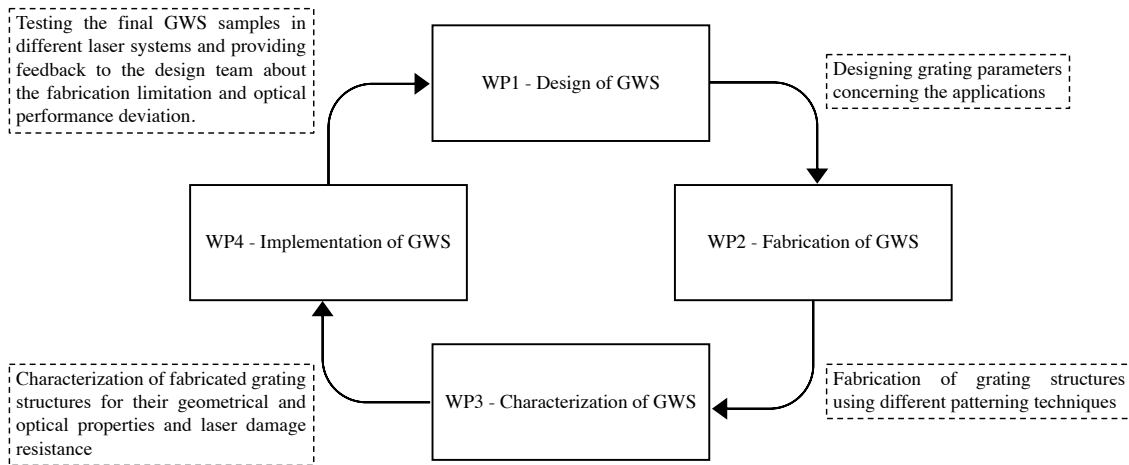


Figure 2.1. Technical WPs overview of research methodology in developing GWS

In WP 1, the responsible ESRs designs the GWS for each application and provides information about grating structure parameters for the fabrication team in WP 2. In WP 2, the ESRs develop grating structures on multilayer deposited on FS substrates and Si substrates using different fabrication techniques such as EBL [133-136], LIL [147-155], and SBIL [138-141]. In parallel, the developed Si masters will be used to produce replicas of grating structures for NIL [143-146]. The dielectric materials used for multilayer deposition are Niobium Pentoxide (Nb_2O_5), Silicon dioxide (SiO_2), and Hafnium (IV) oxide (HfO_2) [156-158]. The final GWS is obtained with the etching process performed by the RIE technique of the fabricated gratings structures.

The main objective of WP 2 is to achieve good process control of fabrication technologies in terms of their fabrication limitations and tolerance since the produced GWS has a high sensitivity to parameters deviation, such as waveguide thickness, waveguide effective index, and the grating parameters (grating period, grating depth, grating profile and Duty Cycle). The need for producing very clean and defect-free GWS

with the grating parameters as close to the design from WP 1 is very crucial for obtaining 99.9% diffraction efficiency when implemented in different laser systems.

In WP 3, we characterize the GWS samples for their geometrical properties like the surface topography of grating structures using Atomic Force Microscopy (AFM), profilometry, and Scanning Electron Microscopy (SEM). The optical characterization of the fabricated GWS samples is carried out using reflectivity, ellipsometry-based set-ups, and DE measurement techniques.

Finally, in WP 4, the GWS samples are tested by implementing them in the different laser systems. Results on the characterization are provided to WP 1 about GWS's performance and fabrication limitations, which are then used by WP 1 ESRs to re-optimize the GWS designs and to provide newly optimized grating parameters to the fabrication team in WP 2.

In this thesis work, ESR 2 is responsible for carrying out WP 2 and 3 activities involving the fabrication and characterization of GWS, as presented in Fig 2.2. Specifically, the tasks carried out in WP 2 were to develop GWS using the direct LIL patterning technique and to develop Si master gratings using the LIL technique for the A3 and A4 applications (table 1.3).

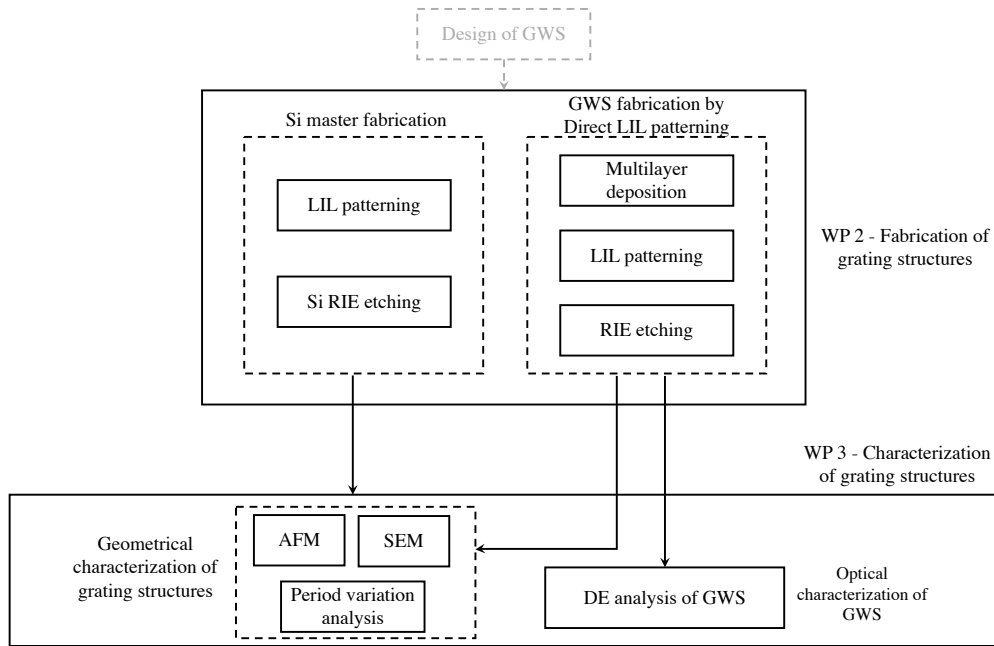


Figure 2.2. Responsible tasks performed in this thesis work.

This chapter presents the fabrication of gratings structures on multilayer deposited samples and Si substrates. The fabrication of gratings structures on multilayer samples is performed using the direct LIL patterning method. Then, the grating structure is etched onto the multilayer by the RIE technique.

In parallel, the fabrication of Si master gratings is done using the LIL patterning method and etching of Si to produce the LIL master. The fabricated GWS and Si master gratings are studied for their geometrical properties using AFM, SEM, and period variation analysis. The DE analysis studies the optical characterization of the GWS sample used for the A4 application.

2.2. Design of GWS

The GWS is designed by the ESR 1 at IFSW, University of Stuttgart, Germany, in WP1 using *MC grating* software and *Microsim* software based on RCWA numerical

method. The designs are dedicated to address the targeted A3 and A4 applications. This section presents the simulated diffraction efficiency of low- and high-index GWS for the A3 application and high-index GWS for the A4 application. The acceptable tolerance during the fabrication of GWS in terms of the grating period (Λ), grating depth (d), and Duty Cycle (DC) are simulated as well.

2.2.1. Low index GWS for A3 application

The grating parameters of low-index GWS for application A3 are designed with 28 alternating layers of SiO_2 and Nb_2O_5 ($\lambda/4$), as described in Fig 2.3(a). The top SiO_2 layer is designed to have a binary grating profile with a grating period of 554 nm, a grating depth of 30 nm, and a Duty Cycle of 50%. The calculated DE for the low-index GWS for A3 applications is plotted as shown in Fig 2.3(b), at incidence angle, AOI = 61.74° (Littrow) with the DE for $\text{TE}_0 > 92.5\%$ and $\text{TE}_{-1} < 7.5\%$ at 976 nm.

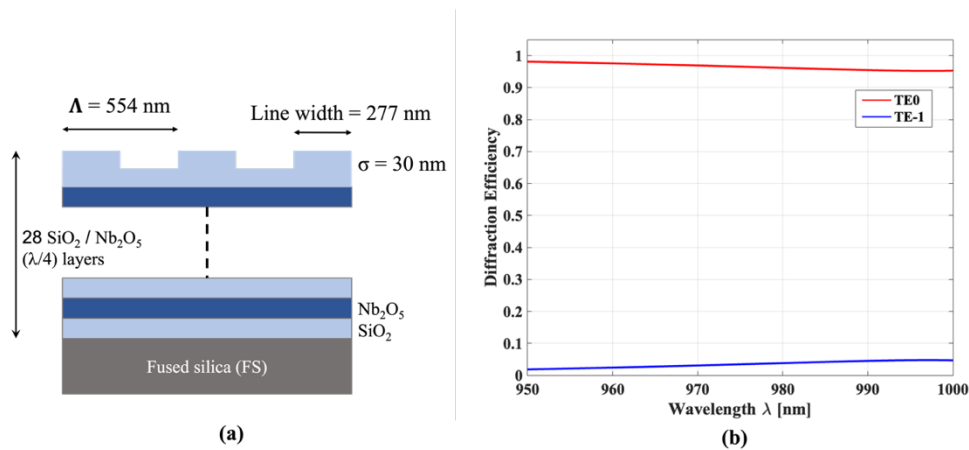


Figure 2.3. Design of low-index GWS for A3 application, (a) sketch with design parameters. (b) The calculated DE plot for TE at 0th and -1st order with $\text{TE}_0 > 92.5\%$ and $\text{TE}_{-1} < 7.5\%$ at 976 nm.

Fig. 2.4(a-c) presents the simulated fabrication tolerance for low-index GWS for A3 application varying grating depths from -20 nm to +10 nm, varying Duty Cycle from -30

% to +30 % and grating period variation from -5 nm to +5 nm. From Fig. 2.4(a), the acceptable grating depth variation should lie within the range of 0 to less than 5 nm to maintain diffraction efficiency for $TE_0 \sim 90\%$ and $TE_{-1} \sim 10\%$. From Fig. 2.4(b), the acceptable variation in the Duty Cycle must lie within the range of -20% to +10% to obtain diffraction efficiency at $92.5\% < TE_0 < 95\%$ and $TE_{-1} < 5\%$. The acceptable grating period variation lies within the range of 0 to 5 nm, as shown in Fig. 2.4(c), to maintain $TE_0 > 92.5\%$ and $TE_{-1} < 7.5\%$. Therefore, the grating depth and Duty Cycle variation are important parameters to be controlled during the fabrication.

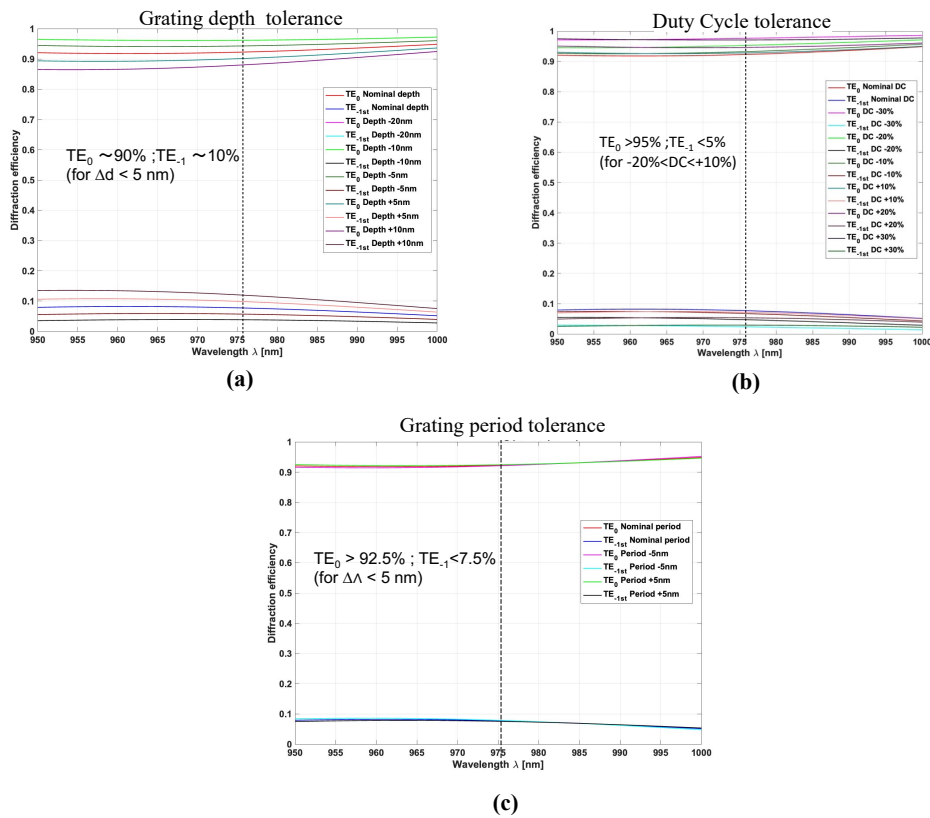


Figure 2.4. Simulated tolerance of low-index GWS for A3 application, (a) Grating depth tolerance for variation from -20 nm to +10 nm. (b) Duty Cycle tolerance for variation from -30 % to +30 %. (c) Grating period tolerance for variation from -5 nm to +5 nm.

2.2.2. High index GWS for A3 application

High-index GWS for application A3 is designed with 29 layers of alternation Nb_2O_5 and SiO_2 ($\lambda/4$), as described in Fig 2.5(a). The grating structures must have a binary grating profile with a grating period of 554 nm, a grating depth of 150 nm, the top Nb_2O_5 layer completely etched, and the remaining 34 nm etched in the SiO_2 layer. The Duty Cycle is designed to be 21%. The calculated DE for the high-index GWS for A3 applications is plotted as shown in Fig 2.5(b), at incidence angle, AOI = 55° (Littrow), with the DE for TE -1st >99.9% at 976 nm.

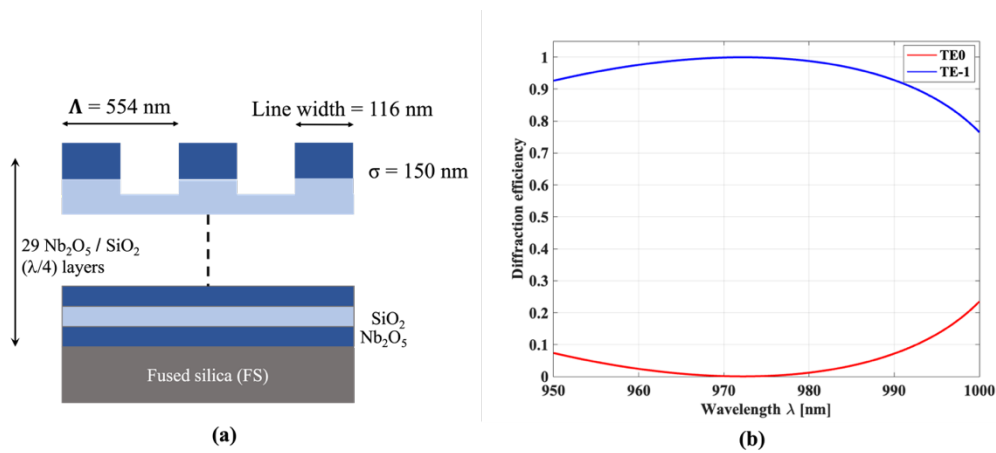


Figure 2.5. Design of high-index GWS for A3 application, (a) sketch with design parameters. (b) The calculated DE plot for TE at 0th and -1st order with TE₋₁ >99.9% at 976 nm.

Fig. 2.6(a-c) presents the simulated fabrication tolerance for high-index GWS for A3 application varying grating depths from -30 nm to +30 nm, varying Duty Cycle from -40 % to +40 % and grating period variation from -5 nm to +5 nm. From Fig. 2.6(a), the acceptable grating depth variation should lie within the range of -20 nm to +10 nm to maintain diffraction efficiency for TE₋₁ ~ 97%. From Fig. 2.6(b), the acceptable variation of $0 < \text{DC} < +10\%$ to obtain diffraction efficiency at TE₋₁ ~ 98%. The acceptable grating

period variation must lie between 0 nm and 3 nm, as shown in Fig. 2.6(c), to maintain $TE_{-1} \sim 99.9\%$. Therefore, the grating depth variation is an important parameter to be controlled during the fabrication.

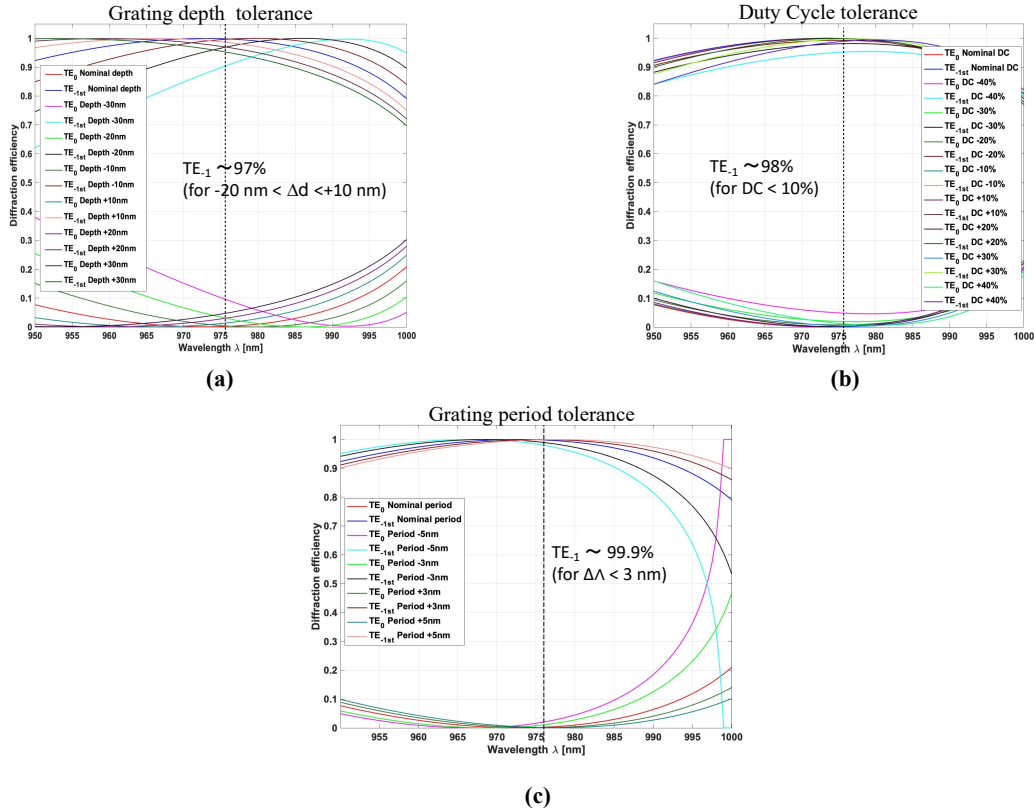


Figure 2.6. Simulated tolerance of high-index GWS for A3 application, (a) Grating depth tolerance for variation from -30 nm to +30 nm. (b) Duty Cycle tolerance for variation from -40 % to +40 %. (c) Grating period tolerance for variation from -5 nm to +5 nm.

2.2.3. High index GWS for A4 application

For the A4 application, the design structure consists of 27 alternating Nb_2O_5 and SiO_2 ($\lambda/4$) layers and two modified layers with SiO_2 of thickness 79 nm and the topmost Nb_2O_5 layer of thickness 88 nm, as described in Fig 2.3(a). The grating structures have a binary grating profile with a period of 619 nm, a grating depth of 88 nm, and a Duty Cycle of

50%. The grating is designed to have DE in TE -1^{st} $> 99.9\%$ at 1030 nm at incidence angle, AOI = 56.3° (Littrow), as shown in Fig 2.7(b).

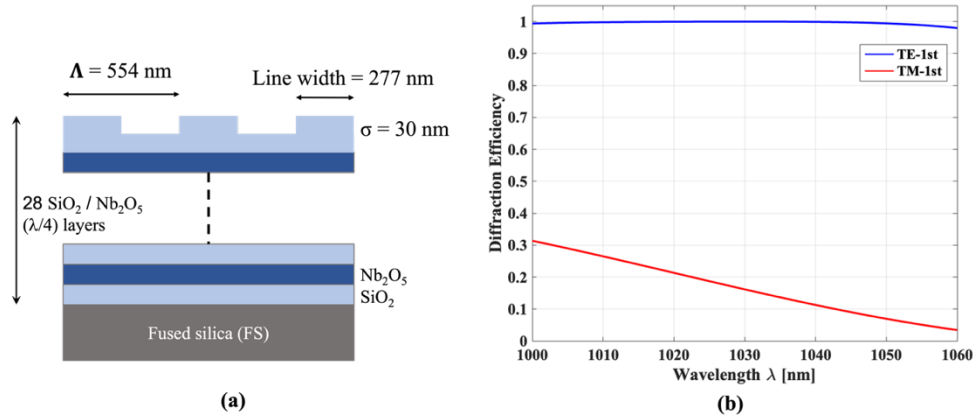


Figure 2.7. Design of high-index GWS for A4 application, (a) sketch with design parameters. (b) The calculated DE plot for TE and TM -1^{st} order with $TE_{-1} > 99.9\%$ at 1030 nm.

Fig. 2.8(a-c) presents the simulated fabrication tolerance for high-index GWS for A4 application varying grating depths from -30 nm to +30 nm, varying Duty Cycle from -20 % to +10 % and grating period variation from -5 nm to +5 nm. From Fig. 2.8(a), the acceptable grating depth variation should be within the range of -10 nm and +10 nm to maintain diffraction efficiency for $TE_{-1} \sim 99.9\%$. From Fig. 2.8(b), the acceptable variation in the DC is 0 to +10% to obtain diffraction efficiency at $TE_{-1} > 92\%$. The acceptable grating period variation is between 0 nm and 5 nm, as shown in Fig. 2.8(c), to maintain $TE_{-1} \sim 99.9\%$. Therefore, the Duty Cycle variation is an important parameter to be controlled during the fabrication.

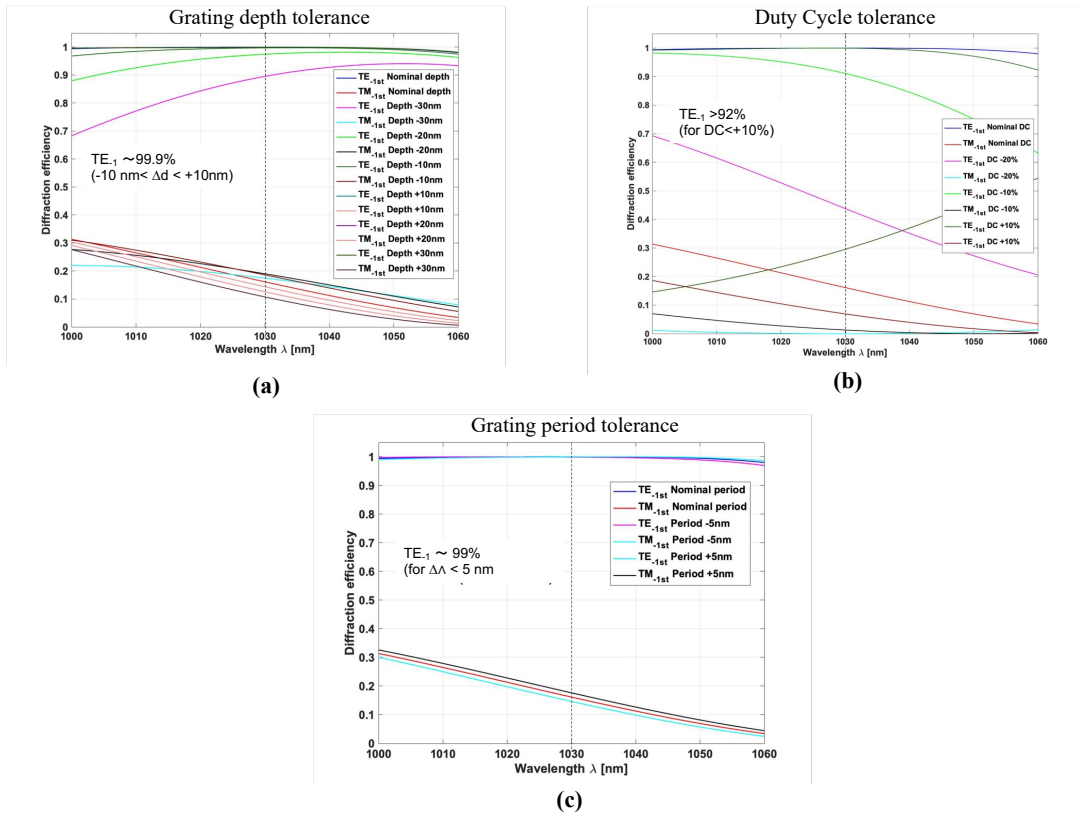


Figure 2.8. Simulated tolerance of high-index GWS for A4 application, (a) Grating depth tolerance for variation from -30 nm to +30 nm. (b) Duty Cycle tolerance for variation from -20 % to +10 %. (c) Grating period tolerance for variation from -5 nm to +5 nm.

The optimized design parameters provided to the fabrication team (ESR 1) with the respective fabrication tolerance are listed in Table 2.1. for the A3 and A4 applications.

Parameter	Low-index GWS for application A3	High-index GWS for application A3	High-index GWS for application A4	Target DE
Grating period, Λ (nm)	554	554	619	TE ₀ >92.5% TE ₋₁ <7.5% at 976 nm AOI=61.74°
Grating depth, d (nm)	30	150	88	TE ₋₁ >99.9% at 976 nm AOI=55°
Duty Cycle, DC (%)	50	21	50	TE ₋₁ >99.9% at 1030 nm AOI=56.3°
Fabrication tolerances	$\Delta d < +5$ nm -20% < DC < +10% $\Delta\Lambda < +5$ nm	-20 nm < Δd < +10 nm DC < +10% $\Delta\Lambda < +3$ nm	-10 nm < Δd < +10 nm -10% < DC < +10% $\Delta\Lambda < +5$ nm	

Table 2.1. Optimized design parameters and fabrication tolerances of GWS for A3 and A4 applications.

2.3. Fabrication of grating structures

2.3.1. Fabrication of GWS

2.3.1.1. Deposition of multilayer films

The first step is depositing a multilayer stack on clean industrial-grade fused silica substrates of 2-inch diameter and 10 mm thickness. The substrates are first immersed in an ultrasonic bath of 40 kHz with acetone solution for 10 minutes. Then the substrate is immersed in ethanol solution for 10 minutes (still under ultrasonics), and finally, it is washed in running distilled water for 10 minutes. The cleaned FS substrates are then

deposited with a multilayer stack using a Physical Vapor Deposition (PVD) method called Plasma Assisted Reactive Magnetron Sputtering (PARMS) [159-162].

The working principle sketch of PARMS, as shown in Figure 2.9., is that upon supplying an electric field of up to several thousand electron volts, the plasma is generated with sufficient force to bombard with a cathode connected to the sputter target. The sputtering is made possible in reactive gas like oxygen or nitrogen [163]. Upon bombardment, the solid atoms of the target are ejected and deposited uniformly on the substrate as thin oxide and nitride films.

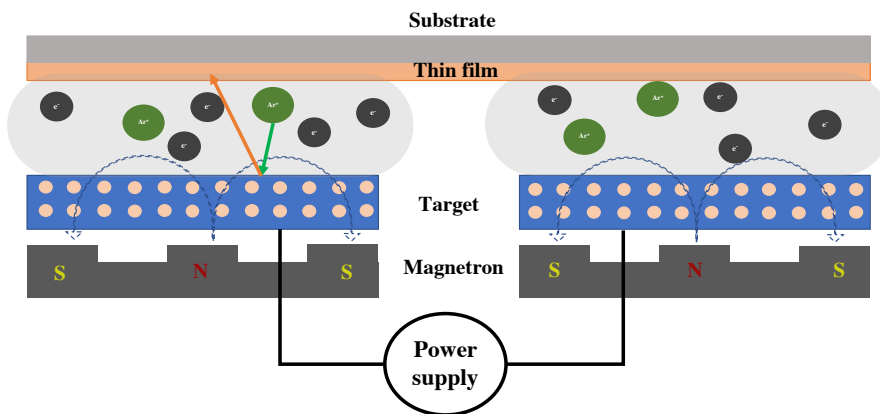


Figure 2.9. Working principle of Plasma assisted reactive magnetron sputtering

The coating materials used in deposition on FS substrates for the applications mentioned in Section 2.1., are Nb_2O_5 and SiO_2 . The FS substrates are deposited with alternating layers of Nb_2O_5 and SiO_2 using *Helios 400* sputter coater from *Bühler*. The electric power required to generate the plasma is 46 kVA. The deposited multilayer stack on FS substrates is listed in Table 2.2., for A3 and A4 applications.

Deposition parameters	Low-index GWS for application A3	High-index GWS for application A3	High-index GWS for application A4
Coating materials	SiO ₂ and Nb ₂ O ₅	Nb ₂ O ₅ and SiO ₂	Nb ₂ O ₅ and SiO ₂
Single Layer thickness (nm) - $\lambda/4$ layer	244	244	257
Number of layers	28	29	27 + two top layers with 88 nm Nb ₂ O ₅ layer and 79 nm SiO ₂
Top layer	SiO ₂	Nb ₂ O ₅	Nb ₂ O ₅

Table 2.2. Deposited multilayer stack on 2-inch diameter FS substrates for A3 and A4 applications.

2.3.1.2. Direct LIL patterning

The next step in the fabrication is to pattern the gratings on the multilayer stacked FS substrates using the LIL technique. Two fabrication processes are carried out to develop grating patterns on a 2-inch FS substrate and Si wafer. The direct LIL patterning method is implemented to develop grating structures on FS substrates, as shown by its fabrication process flow in Figure 2.10.

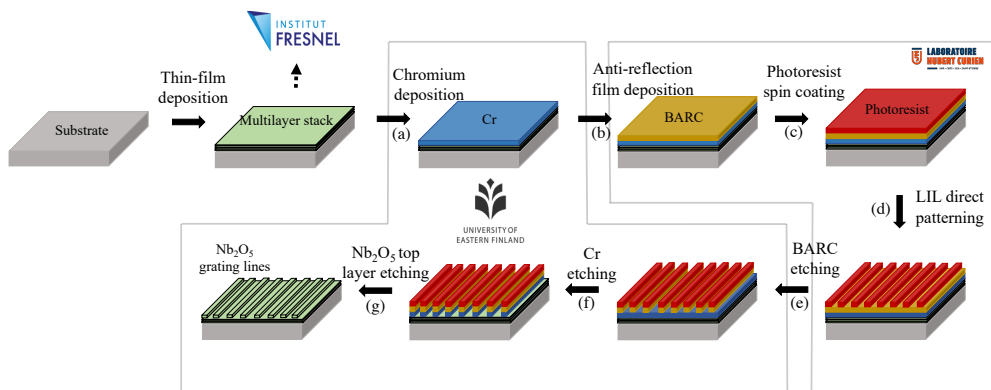


Figure 2.10. Complete fabrication process flow of grating with LIL direct patterning technique. The multilayer deposition (a) was carried out at Institut Fresnel (IF) by ESR 6, France. The process of BARC and photoresist deposition (b-c) and LIL patterning and development of photoresist gratings structures (d) are performed at Hubert Curien laboratory (LabHC), France. The etching process (f-g) is performed at the University of Eastern Finland (UEF) with the help of ESR 5, Finland.

- a) The multilayer stacked FS substrate is first coated with a thin layer of chromium of 50 nm using *Chrome Q300 sputter* by oxford instruments. Chromium is used as a hard mask to facilitate slow etching during the dry etching process later in the fabrication process flow.
- b) The FS substrate is then cleaned by oxygen plasma for 1 minute to remove contaminants and coated with *AZ® Barli II* by *MicroChemicals*, a back anti-reflection coating (BARC) of 200 nm thickness using a spin coater for 1 minute at 3000 rpm and soft baked for 40 minutes at 200°C.
- c) The BARC-coated multilayer stack substrate is then coated with S1805 (*Shipley*), a negative photoresist layer of 600 nm thickness, by spin coating for 1 minute at 5000 rpm and soft baked for 20 minutes at 90°C.
- d) The grating patterning is performed using the LIL setup in the Nano-Saint-Etienne platform of LabHC, as seen in Figure 2.7.

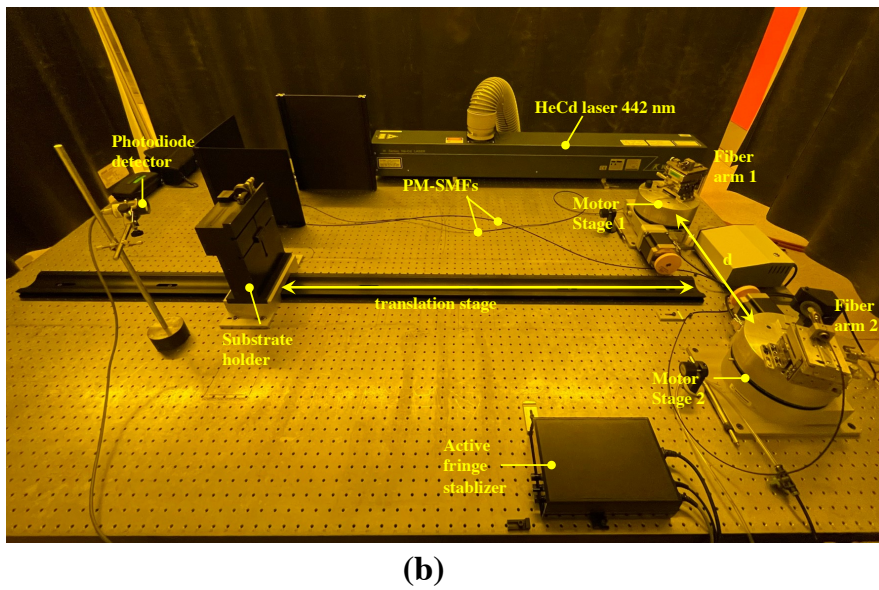
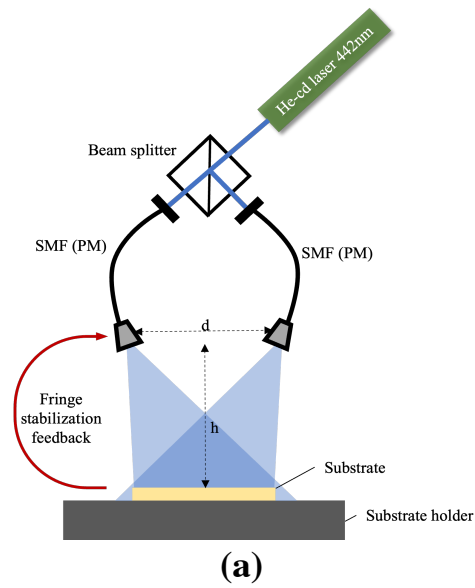


Figure 2.11. (a) The schematic sketch and (b) a Photograph of the LIL setup (Nano Saint-Etienne platform, LabHC).

The photoresist-coated multilayer stacked substrate is exposed to interference fringes formed by combining two spherical beams emerging from the fiber arms. The laser source is a HeCd laser at 442 nm and output power of 210 mW. The LIL setup is adjusted for

the appropriate grating period for each design specified in Table 2.1. The LIL recipe used to develop the photoresist gratings is detailed in table 2.3.

Patterning factor	Low-index GWS for application A3	High-index GWS for application A3	High-index GWS for application A4
Received power at the substrate holder ($\mu\text{W}/\text{cm}^2$)	423	423	348
Exposure time (minutes)	4	4	5
Exposure dose (mJ/cm^2)	101.5	101.5	104.4
Developing time	15	15	15

Table 2.3. LIL recipe with exposure dose and developing time information used to develop photoresist gratings on multilayer stack FS substrates for A3 and A4 applications.

- e) The recorded grating pattern is then developed using an organic developer solution called MF[®] - 319 by MICROPOSIT[®] for 15 seconds at 21°C.
- f) The developed photoresist grating samples are then etched using the RIE process. Oxygen plasma is used for 10 seconds at a chamber pressure of 15 mTorr before the RIE etching of the photoresist grating substrate to etch the BARC layer underneath the photoresist grating layer using plasma Lab100. For all GWS design structures mentioned in Fig 3.3, the BARC is etched for 4 minutes using Fluoroform (CHF_3) and Oxygen (O_2) gases at a chamber pressure of 20 mTorr and RF power of 200 W with an etching rate of 50 nm per minute.
- g) After the BARC is etched, the grating structure is etched through Chromium for 3 minutes using CHF_3 and O_2 gases at a chamber pressure of 15mTorr and DC power 67 W with an etching rate of 17 nm per minute.
- h) The next step in the direct LIL process flow involves the RIE the top layer of the multilayer stack using *Plasma Lab80* by Oxford Instruments. To etch the SiO_2 top

layer for low-index GWS design as shown in Fig 2.3(a), the gases used are CHF_3 and Argon (Ar) gases, with a chamber pressure of 8 mTorr and RF power of 100 W with an etching rate of 25 nm per minute. To etch the Nb_2O_5 top layer for high-index GWS designs, as shown in Fig 2.3(b)-(c), the gases used are CHF_3 and Ar gases, with a chamber pressure of 8 mTorr and RF power of 100 W with an etching rate of 32 nm per minute. The GWS samples are then treated with O_2 plasma for 3 minutes in a chamber pressure of 15mTorr and RF power of 200 W to remove photoresist and BARC residue. After the plasma treatment, the final GWS samples obtained will first be characterized for their geometrical profiles to study the fabricated grating parameters.

2.3.2. Fabrication of Si master

The second fabrication process is to develop Si gratings on 2-inch Si wafer substrates with 525 μm thickness, to obtain master gratings which can be used in the NIL process to make replicas of grating structures. The process flow of patterning the gratings structures onto Si substrates is shown in Figure 2.8.

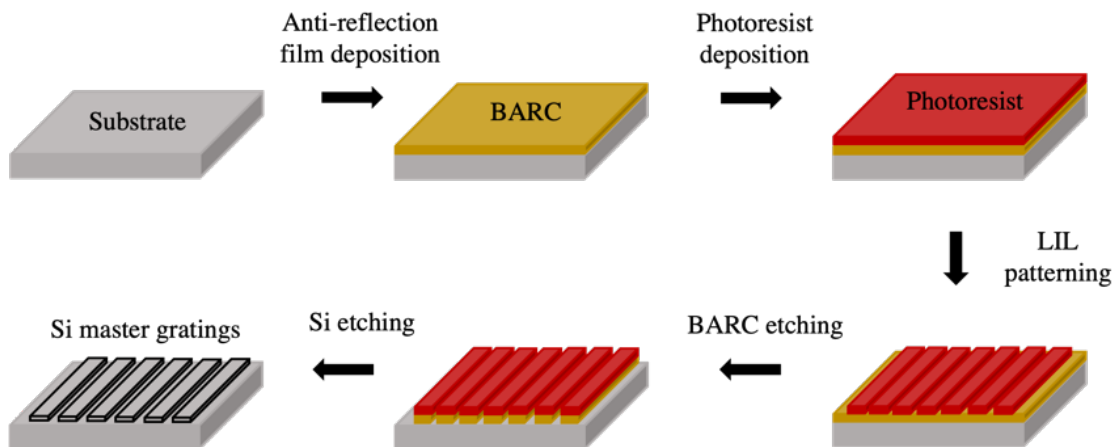


Figure 2.12. Fabrication chain of Si master gratings with LIL technique.

First, the Si substrate is cleaned and spin-coated with a BARC of 200 nm with a spin speed of 3000 rpm. The substrate is baked at 200°C for 2 minutes and then spin-coated with S1805 negative photoresist of the thickness of 600 nm at a spin speed of 5000 rpm. The substrate is then baked at 90°C for 1 minute. The interference fringe pattern is recorded on the substrate with a grating period set to 554 nm for A3 application. The exposure dose and the development time are the same as in table 3.3. The developed photoresist gratings are then treated with a dry RIE process to etch BARC and Si substrates. The etching of BARC is performed using RIE etching for 3 minutes 30 seconds at the chamber pressure of 20 mTorr and RF power of 200 W with the etching rate of 57 nm per minute. The gratings structures are etched onto the Si substrate using the etching recipe of SiO₂ material with an etching time of 4 minutes. The reactive gases used are CHF₃ and Ar gases, with a chamber pressure of 8 mTorr and RF power of 100 W with an etching rate of 46 nm per minute.

2.4. Characterization of grating structures

This section investigates the profile of fabricated grating structures for two designs—the high index GWS for the A4 application and the low index Si master for the A3 application using AFM and SEM techniques [The AFM measurements were performed at Nano Saint-Etienne, France, and the SEM images were obtained with the help of ESR 5 at UEF, Finland]. The surface topographical characteristics of grating structures, such as grating depth and the Duty Cycle, are quantitatively measured with *Bruker's Dimension Icon*® in an intermittent mode called tapping mode, in which the AFM cantilever is in contact with the surface while oscillating at its resonance frequency. This

mode provides an excellent sub-100 nm resolution to measure the grating profile with the 5 nm lower size limit in the z -direction (grating height). Additionally, Zeiss carried out the SEM images of grating structures with SIGMA. The grating period deviation is analyzed using the diffraction period measurement setup (discussed in detail in chapter 3). The optical characterization is carried out for the high index GWS for the A4 application by measuring the diffraction efficiency at the Littrow angle.

2.4.1. High index GWS for A4 application

Fig. 2.13 shows the grating profile of photoresist grating structures on a 2-inch FS substrate with a multilayer stack for A4 application. The measured grating period is 623.5 nm with a grating depth of 454 nm and a Duty Cycle of 45%.

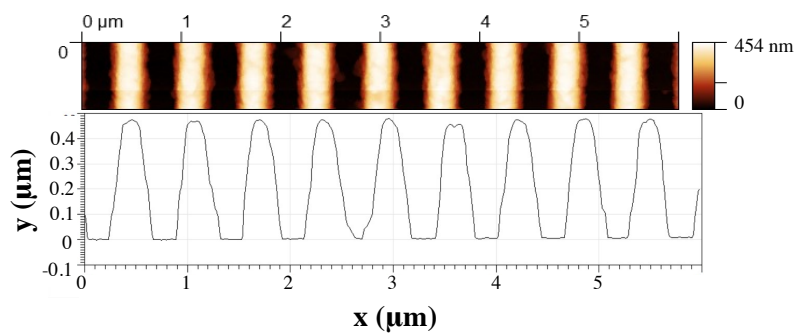


Figure 2.13. AFM data and grating profile of photoresist grating surface on 2-inch multilayer substrate for A4 application.

The photoresist grating substrate is etched for Cr thin layer for 9 minutes in the chamber with a pressure of 15 mTorr and RF power of 15 W. The resulting grating structure has Cr residual with the Duty Cycle of the grating lines reduced from 45% to 33% as shown in Fig. 2.14.

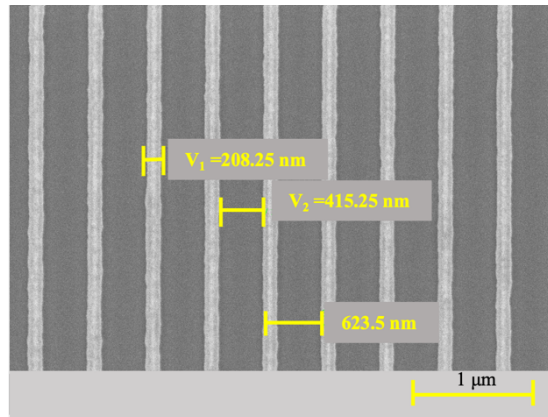


Figure 2.14. SEM image of chromium etched grating surface on 2-inch multilayer substrate for A3 application.

Upon etching the Nb_2O_5 top layer of the GWS for 2 minutes 30 seconds with a chamber pressure of 8 mTorr and RF power of 100 W. The substrate is covered with Cr residual even after the residual removal treatment for 5 min using the pressure of 15 mTorr and RF power of 15 W, as seen in Fig 2.15(a). Fig 2.15(c) shows the AFM measurement of the grating profile, which has a grating depth of 80.3 nm in the center of the substrate.

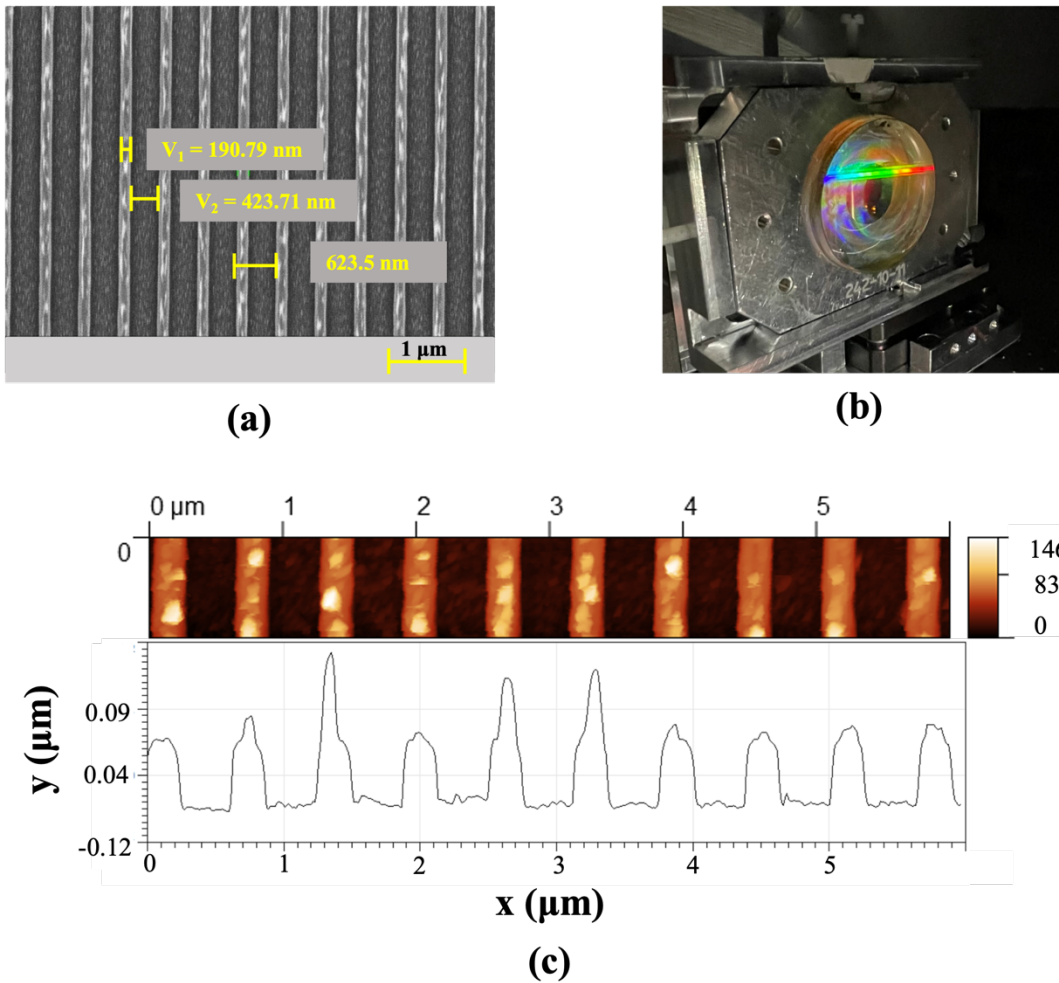


Figure 2.15. (a) SEM image (b) Photograph, and (c) AFM data and grating profile of Nb_2O_5 etched grating surface on 2-inch multilayer substrate for A4 application.

Fig. 2.16(a, b). presents the variation of grating depth and Duty Cycle on the GWS along the central x -axis with the Nb_2O_5 top layer etched for spectral stabilization for 1030 nm solid-state laser application and measured by AFM. Fig. 2.16(a) shows that the grating depth varies over 2 inches with a 25 nm difference. The Duty Cycle also varies, with a variation of 9% away from the center, as seen in Fig. 2.16(b).

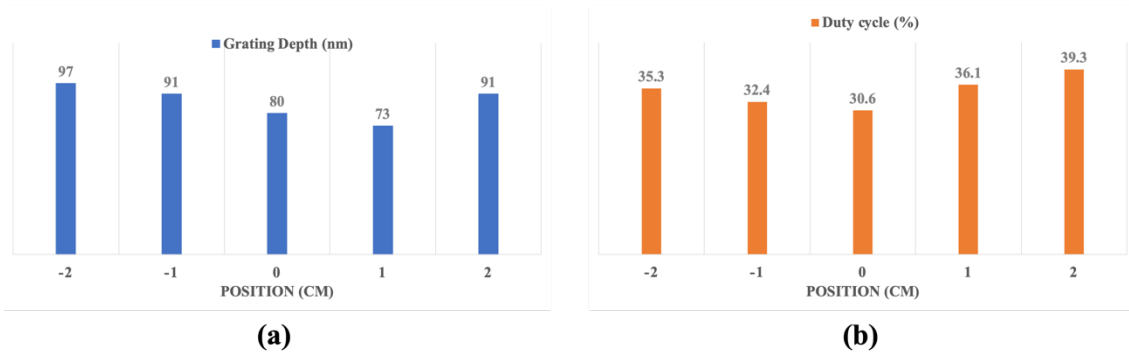


Figure 2.16. Variation in grating depth and Duty Cycle on 2-inch Nb₂O₅ etched multilayer GWS with grating depth varying by 24 nm and Duty Cycle varying by 9% along the central *x*-axis for A4 application.

Fig 2.17 presents the period variation measurement plotted for the 2-inch high index GWS with a grating period of 623.5 nm at the substrate's center (The optical setup is presented and explained in chapter 3). The maximum period variation measured along the *x*-axis is 0.6 nm and 0.2 nm along the *y*-axis. The period variation is below 0.6 nm on both the *x*- and *y*-axis. The variation along the *x*- and *y*- axis needs to be symmetrical due to the translational error during the positioning of the substrate for LIL exposure from the center of the exposure.

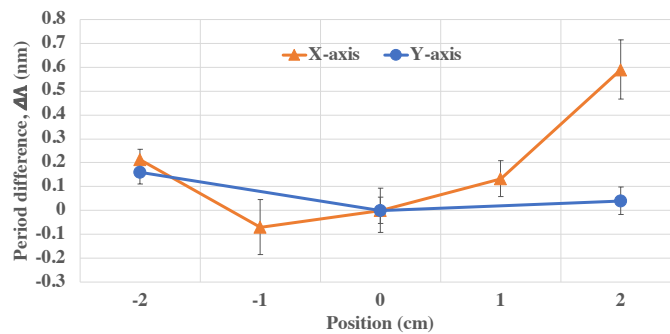


Figure 2.17. A measured period variation along the 2-inch high index GWS for A4 application with a grating period of 623 nm at the substrate's center. The orange plot (▲) is the period variation along the *x*-axis. The blue plot (●) is the period variation along the *y*-axis. The error bar reflects the uncertainty in the diffraction angle measurements.

2.4.2. Optical characterization of high-index GWS for A4 application

This section presents the result of the DE measurement carried out with a high-index GWS for the A4 application. These measurements have been performed in the set-up developed at the Institute for Laser Tools (IFSW, University of Stuttgart) in collaboration with ESR 1. Direct LIL fabricated high-index GWS for A4 application is investigated for its DE using optical measurement. The optical setup configuration used to measure the DE is shown in Fig 2.18.

The DE measurement setup consists of a diode laser tunable from 1000 nm to 1070 nm. The emitted laser beam is passed through a polarization-maintaining fiber (PMF) and collimating lens to have parallel beams. The beam is then made to pass through $\lambda/2$ waveplates to rotate its polarization state. A linear polarizer then sends the beam to allow either transverse electric (TE) or transverse magnetic (TM) polarized beam. The laser chopper disc periodically transmits and interrupts the beam with the set frequency to synchronize with the chopper substrate needed to lock in the system. The chopper laser beam passes through a 50:50 beam splitter from the uncoated layer without experiencing beam splitting. The laser beam strikes the grating sample after passing through the chopper substrate, with the reference substrate reflecting and transmitting the beam. The diffracted beam from the grating sample is reflected by the grating from the high-reflection (HR) substrate and back to the beam splitter through the chopper substrate. The beam is reflected from the beam splitter into the integrating sphere in which the beam is scattered from the interior wall, and the diffused beam is detected by the photodiode and the electrical signal is sent to the lock-in system will calculate the DE of the grating sample by the measured signal from photodiode. The measured DE is displayed on the

computer concerning the wavelength of the laser beam source. Such a lock-in system considerably reduces the noise and increases the DE measurement accuracy.

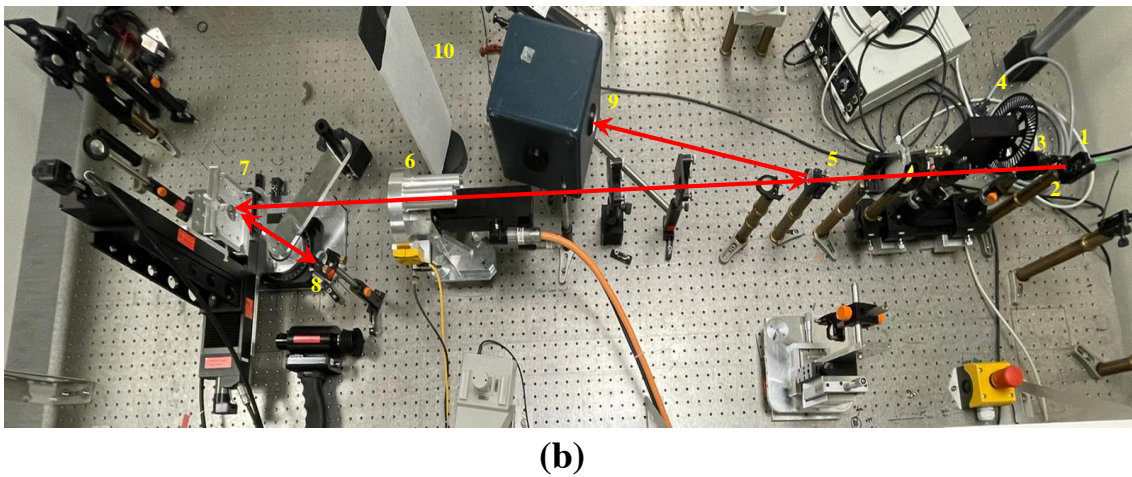
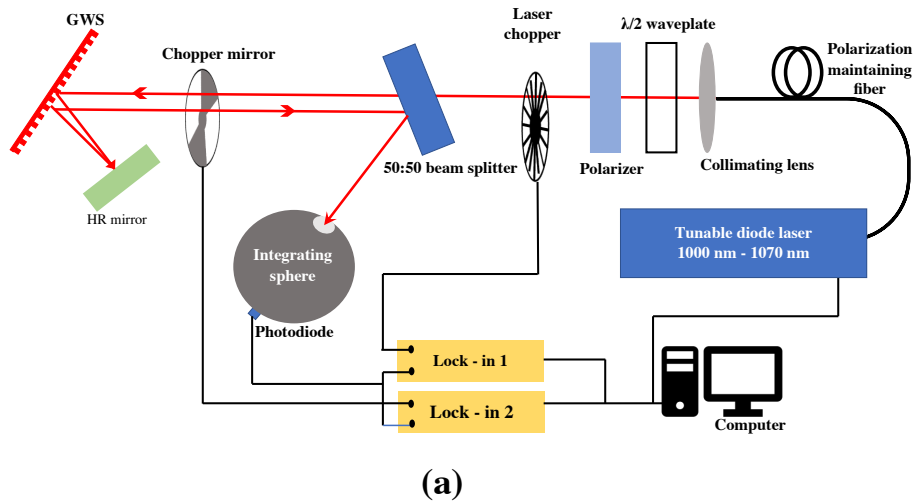


Figure 2.18. (a) The schematic configuration of DE measurement setup to analyze the DE response of the GWS sample using a tunable diode laser in the 1000 nm to 1070 nm range. (b) Photograph of the measurement setup 1. Diode laser output from polarization maintaining fiber, 2. Collimating lens, 3. Polarizer and $\lambda/2$ waveplate, 4. Laser chopper, 5. The beam splitter, 6. Chopper mirror, 7. GWS sample holder, 8. HR mirror, 9. Integrating sphere, 10. White screen for aligning reference and reflected laser beam from the GWS sample.

The DE is measured for TE and TM at -1st order for wavelength ranging from 994 nm to 1060 nm with an interval of 2 nm at Littrow configuration. The obtained DE values are plotted versus the wavelength, as shown in Fig 2.19.

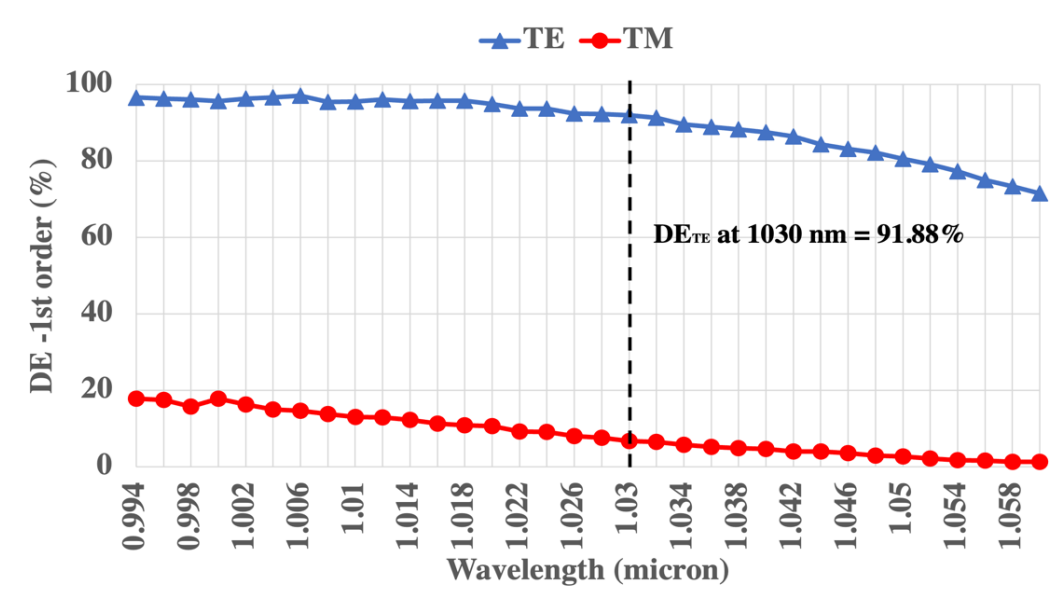


Figure 2.19. The measured DE of TE and TM -1st orders of GWS with a grating period of 623.5 nm and grating depth of 80 nm with a Duty Cycle of 30%.

The DE for TE -1st order at 1030 nm is 92 %. The measured DE is less than the calculated DE from Fig 2.7(b). The losses in DE are attributed to the deviation in the fabricated GWS parameter from the designed parameters with a grating period deviation of 4.5 nm and grating depth deviating by 8 nm, and Duty Cycle by -20% grating roughness leading to scattering losses. From table 2.1, the significant variation in the Duty Cycle is predicted to affect the diffraction efficiency strongly for TE₋₁.

Fig 2.20 shows the measured spatial DE in TE -1st order over 2-inch GWS of grating period 623.5 nm and grating depth of 80 nm with a Duty Cycle of 30%. The spatial scanning was performed by keeping the wavelength of the laser beam constant at 1030

nm and setting the scanning program to measure DE for 3 cm x 3 cm with steps of 1 mm. The DE is higher in the concentric ring shape on the substrate. This further indicates the nonuniform photoresist development during the fabrication process and the grating profile is etched onto the underneath multilayers.

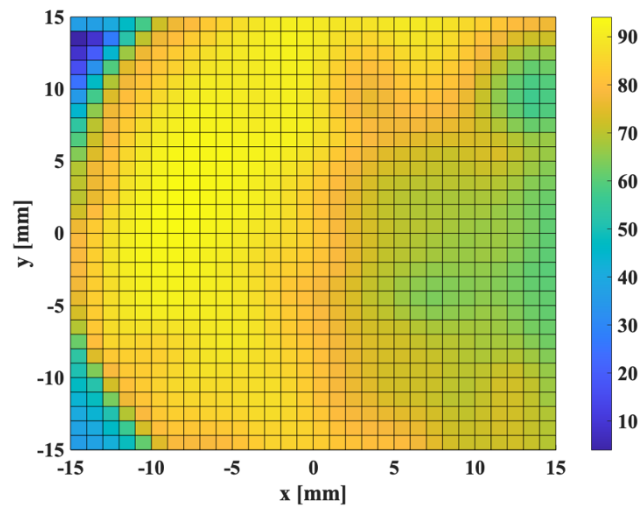


Figure 2.20. The measured spatial DE in TE -1st order of 2-inch GWS with a grating period of 623.5 nm and grating depth of 80 nm with a Duty Cycle of 30%.

To optimize the design with the feedback of fabricated GWS parameters, the DE of high-index GWS for solid-state laser at 1030 nm is restimulated using the GWS parameters obtained by the fabrication process. The recalculated DE with a grating period of 623.5 nm, grating depth of 80 nm, and Duty Cycle of 30%, as shown in Fig 2.21., follows the measured data plot in Fig 2.20 with the simulated DE at TE₋₁ ~ 91.5%

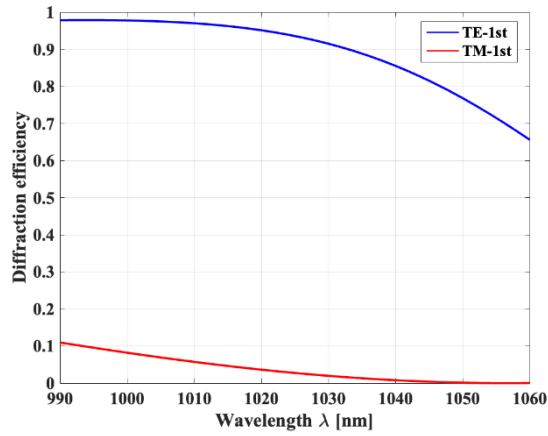


Figure 2.21. Recalculated DE for TE and TM in -1st order for GWS parameter obtained by fabrication process with grating period 623.5 nm, grating depth of 80 nm, and Duty Cycle of 30%. DE at 1030 nm for TE -1st order is 91.5%

Similarly, the fabricated samples for low- and high-index GWS for A3 applications are geometrically characterized and are listed in table 2.4. From table 2.4, the fabricated GWS suffers from parameter nonuniformity along the substrate.

Design	Grating period (nm)		Duty Cycle (%)		Grating depth (nm)	
	Design	Fabricated (Deviation for center)	Design	Fabricated (Deviation for center)	Design	Fabricated (Deviation for center)
Low-index GWS for A3 application	554	556.3 (+0.3)	50	33	30	25
High-index GWS for A3 application	554	556.3 (+0.5)	21	26 (+5)	150	137 (-12 to +5)
High-index GWS for A4 application	619	623.5 (+0.6)	50	30 (+9)	88	80 (-7 to +17)

Table 2.4. List of fabricated GWS parameters and their deviation from the center of the substrate.

From table 2.4, the fabricated GWS suffers from parameter nonuniformity along the substrate.

2.4.3. Low-index Si master for A3 application

The photoresist grating profile on 2-inch Si master gratings for the A3 application is shown in Fig 2.22. The AFM measurement of the photoresist grating structure gives a grating period of 556 nm with a grating depth of 467 nm and a Duty Cycle of 42%.

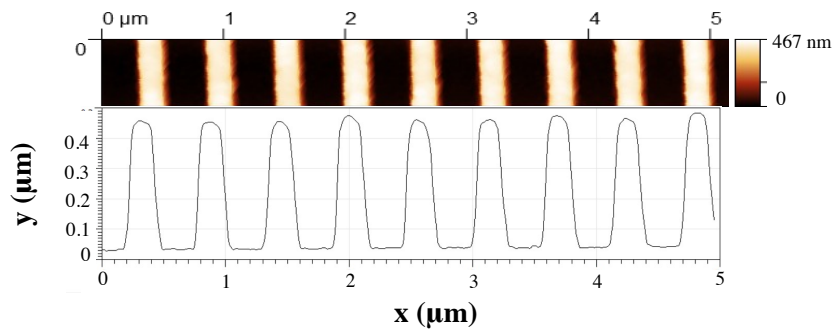


Figure 2.22. AFM data and grating profile of photoresist grating surface on a 2-inch Si substrate to develop master gratings for A3 application.

After etching the BARC for 3 minutes and 30 seconds using CHF_3 and O_2 gases with a chamber pressure of 15 mTorr and RF power of 200 W, the grating profile is etched onto the Si substrate by the RIE SiO_2 etching process for 1 minute and 30 seconds. From Fig 2.23(a, c), the resulting master grating has a grating Duty Cycle will low of 6.3% at the center of the master substrate, and the AFM measured grating depth is 243 nm giving the etching rate of SiO_2 on this Si substrate as 161.8 nm per minute.

Fig. 2.24 (a, b). presents the variation of grating depth and Duty Cycle on the master grating along the central x -axis for wavelength stabilization and multiplexing for 976 nm diode laser application and is measured by AFM. Fig. 2.24(a) shows that the grating depth

varies over 2 inches with a 13 nm difference. The Duty Cycle also varies, with a variation of 7% away from the center, as shown in Fig. 2.24(b).

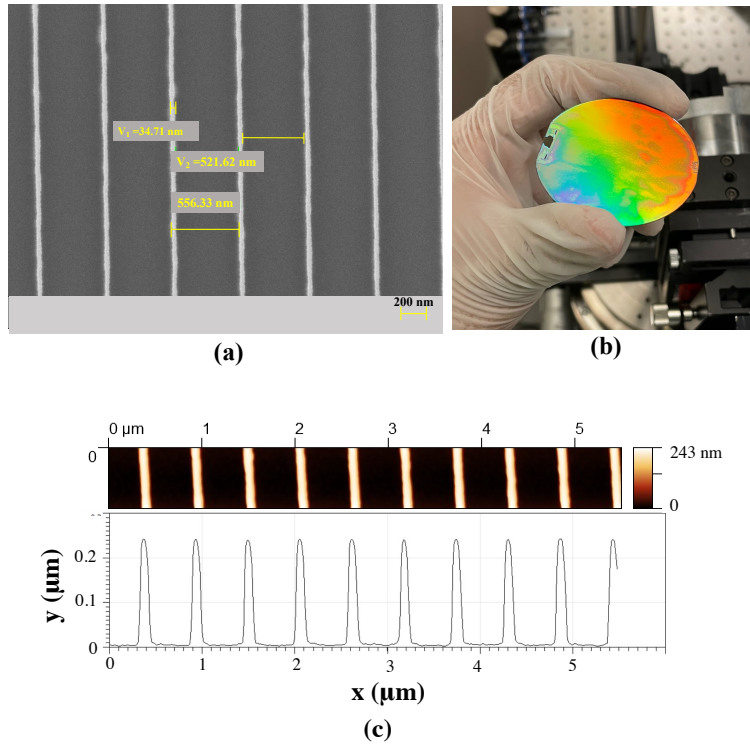


Figure 2.23. (a) SEM image, (b) Photograph, and (c) AFM data and grating profile of Si etched master grating with a grating depth of 243 nm at the center of the substrate and Duty Cycle of 9% on 2-inch Si for A3 application.

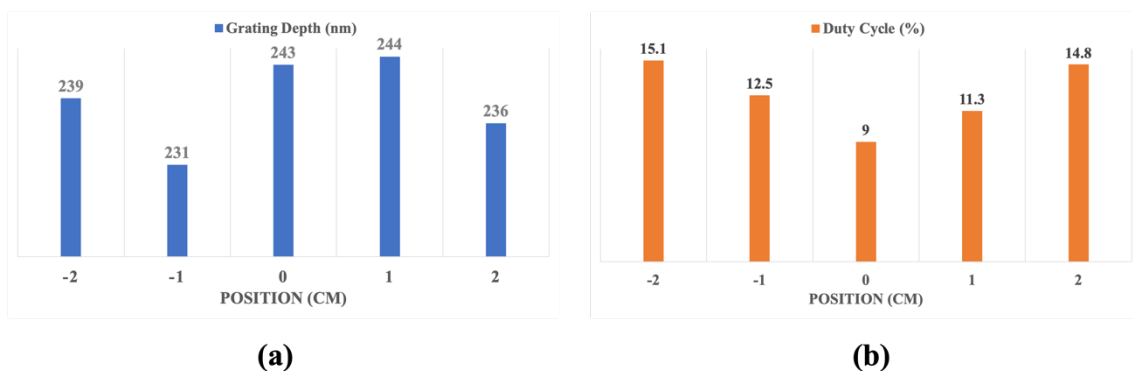


Figure 2.24. Variation in grating depth and Duty Cycle on 2-inch Si etched master grating with grating depth varying by 13 nm and Duty Cycle varying by 7% along the central x -axis for A3 applications.

Fig 2.25 presents the period variation measurement plotted for the 2-inch master grating with a grating period of 556 nm at the substrate's center. The maximum period variation measured along the x -axis is 1.5 nm and 1.1 nm along the y -axis. The uniformity of the grating period suffers period variation above 1 nm in both the x - and y -axis.

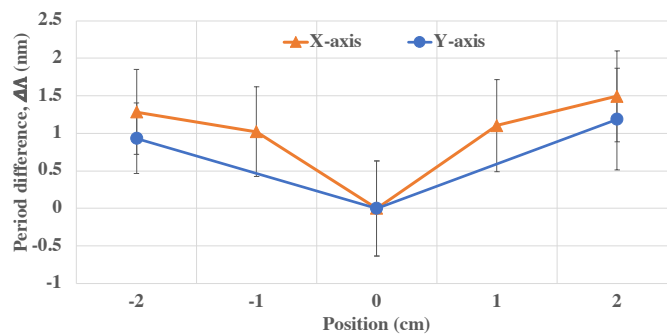


Figure 2.25. A measured period variation along the 2-inch Si master grating A3 application with a grating period of 556 nm at the substrate's center. The orange plot (\blacktriangle) is the period variation along the x -axis. The blue plot (\bullet) is the period variation along the y -axis. The error bar reflects the uncertainty in the diffraction angle measurements.

Similarly, the fabricated Si master samples for high-index GWS for A3 and A4 applications are geometrically characterized and are listed in table 2.5. From table 2.5, the grating parameters of the fabricated Si masters are not uniform across the substrate. The non-uniformity is due to the gaussian beam of the LIL exposure. The uneven exposure dose is transferred into the grating structures during the development stage resulting in varying grating profiles along the substrates. In the next chapter, this thesis will address the uniformity of grating structures with a primary focus on grating period uniformity. The significant reduction in the period variation of Si master of high-index master for A4 application motivates period uniformity. As noticed in table 2.5, the period variation is only +0.1 nm due to the temporary deformation of Si substrate during the LIL

exposure using a concave vacuum chuck. This technique is discussed in detail in the next chapter.

Design	Grating period (nm)		Duty Cycle (%)	Grating depth (nm)	
	Design	Fabricated (Deviation for center)	Fabricated (Deviation for center)	Design	Fabricated (Deviation for center)
Low-index master for A3 application	554	556.3 (+1.5)	9 (+7)	>30	243(-12 to +1)
High-index master for A3 application	554	556.3 (+1.2)	6 (+7)	>150	221 (-1 to +10)
High-index master for A4 application	619	623.5 (+0.1)	20 (+11)	>88	235 (-6 to +8)

Table 2.5. List of fabricated Si master parameters and their deviation from the center of the substrate.

2.5. Defects in the grating structures

As mentioned in section 2.1, the quality of fabricated GWS samples in terms of their grating parameters matching the design parameters and their defect-free surface is critical to achieving 99.9% DE when implemented in the laser system. This section presents the defects caused by the non-uniform development of gratings during the LIL process and unclean samples. Fig 2.26(a)-(b). shows the non-uniform development of the photoresist when a 2-inch Si substrate was exposed for grating patterning in the LIL setup. The gaussian intensity distribution of the interference fringe will result in uneven exposure dose along the Si substrate and upon development in the developer solution. The exposed

photoresist in the center dissolves faster than the surrounding area giving rise to the macroscopic concentric rings on the substrate.

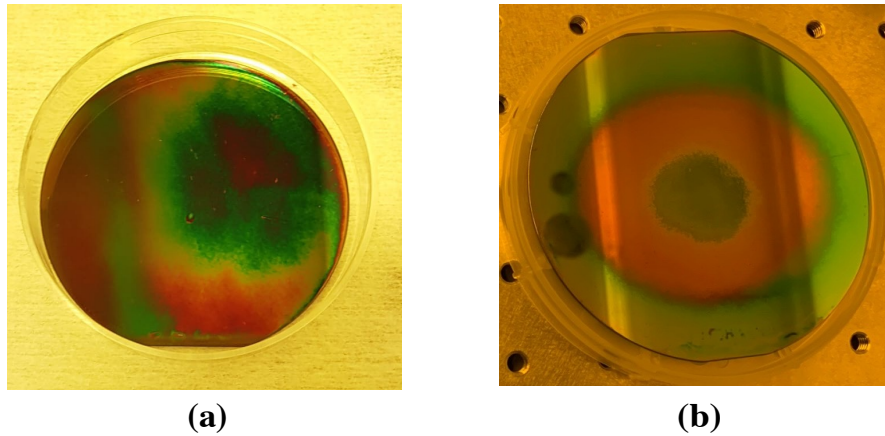


Figure 2.26(a-b). Photograph of the Si substrate with nonuniform development of photoresist grating resulting in macroscopic concentric rings.

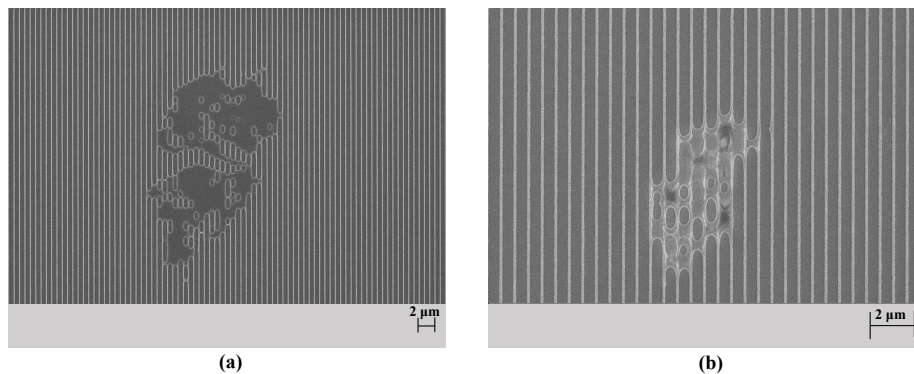


Figure 2.27(a-b). SEM image of GWS fabricated and etched in direct LIL fabrication process flow with defect spots with spot sizes from 2 μm to 10 μm .

Fig 2.27(a-b) shows the defect on the GWS patterned using direct LIL and etched with RIE. The flaws are found in several spots with defect sizes from 2 μm to 10 μm . These defects and the deviation in the fabricated grating parameters from the design parameters will result in a loss in DE and damage to GWS when implemented in a high-power laser system.

2.6. Conclusion

In this chapter, the fabrication and characterization of GWS and Si master gratings are presented in detail. In the fabrication section, the fabrication steps of GWS and Si master gratings are carried out for grating parameters designed for A3 and A4 applications. The first fabrication process flow involved recording the interference fringes using the direct LIL technique directly on BARC and negative photoresist spin-coated multilayer stack FS substrate of 2-inch size and 10 mm thickness followed by RIE etching of BARC, Cr, and the top dielectric layer of the multilayer stack. The second fabrication process flow involved the patterning on BARC and negative photoresist spin coated 2- inch Si wafer of thickness 525 μm and RIE of BARC and SiO_2 . The fabricated GWS and Si master gratings are characterized by their geometrical properties using AFM, SEM, and period variation measurement. From AFM and SEM analysis, the measured values of grating period, grating depth, and Duty Cycle of the fabricated GWS and Si master gratings are listed in Table 2.4 and 2.5 respectively.

By comparing the designed and fabricated parameters of GWS and Si master samples from table 2.4. and table 2.5, the parameters deviation is seen in fabricated GWS from their designed values. This deviation will result in poor performance of the grating structures since the grating profiles are highly sensitive to parameter deviations.

The fabricated GWS and Si master gratings have nonuniform grating depth and Duty Cycle with maximum variation in grating depth of 25 nm and 9% away from the center of the substrates. This problem arises due to the nonuniform exposure dose during the LIL patterning. The gaussian energy distribution profile is thus followed during the

development process of photoresist. Then the same grating profile is etched onto the Cr layer and dielectric multilayers underneath the photoresist and BARC. The period variation measurement of the fabricated GWS and Si master gratings shows the difference in the grating period when moved away from the center of the grating structures, as seen in table 2.6.

The parameter deviation in the fabricated GWS samples affects the DE response in TE -1st orders when implemented in the laser system. This is proved by the DE evaluation of the high-index GWS for the A4 application (Fig 2.19).

Axis	Low-index GWS for application A3		High-index GWS for application A3		High-index GWS for application A4	
	GWS	Si master grating	GWS	Si master grating	GWS	Si master grating
<i>x</i> -axis (nm)	0.3	1.5	0.5	1.2	0.6	0.1
<i>y</i> -axis (nm)	0.3	1.1	0.2	0.7	0.2	0.1

Table 2.6. Measured maximum period variation along the *x*-axis and the *y*-axis of fabricated GWS and Si master gratings for A3 and A4 applications.

The expected efficiency was 99.9% at TE -1st order, however, the GWS sample had an efficiency of 92%. In addition to the deviation of parameters, the fabricated GWS and Si master samples suffered from nonuniformity in the grating profile across the sample area. This was evaluated spatially by scanning the 2-inch high-index GWS for the A4 application (Fig 2.20) by the DE response of high-index GWS for the A4 application. The efficiency was not the same across the 2-inch sample area.

The period variation of Si master grating for 1030 nm solid-state laser from table 2.6, above has a very low period variation on a 2-inch substrate size. This is due to the curved exposure of the Si substrate using a concave vacuum chuck of the radius of curvature 100 cm, compensating for the fringe's inclination and interference angle from the two spherical beams in the LIL setup. The quantitative investigation of the implementation of a concave vacuum chuck to improve the period uniformity on the Si substrate is presented in chapter 3.

Chapter 3

Reduction of Grating Period Variation

3.1. Introduction

This chapter is devoted to quantitatively investigating reducing the period variation by temporarily bending the substrate into a spherical shape during the LIL exposure using a custom-designed concave vacuum chuck [168]. The first step involved is the fabrication of gratings on 4-inch silicon wafers using a flat and concave vacuum chuck. Then, the period of the fabricated samples is measured using a diffraction order measurement setup at Littrow configuration. The results obtained by the Littrow measurements are presented concerning flat and curved exposure and the axis on the silicon wafer. Finally, the bending stress analysis of these fabricated grating samples is presented by optical profilometry and wavefront aberration measurements.

3.2. Implementation of substrate bending technique

3.2.1. A period variation on a flat substrate

In a two-spherical beam LIL setup, as shown in Fig. 3.1, the interference is achieved by two beams with spherical wavefronts. These spherical beams, upon interference, produced a hyperbolic interference pattern on a flat exposed substrate due to two factors [34, 164]. First, the interference angle of the beam changes along the substrate, decreasing with position away from the center. Secondly, the fringe inclination changes along the substrate giving rise to a larger grating period than the interference fringes at the center.

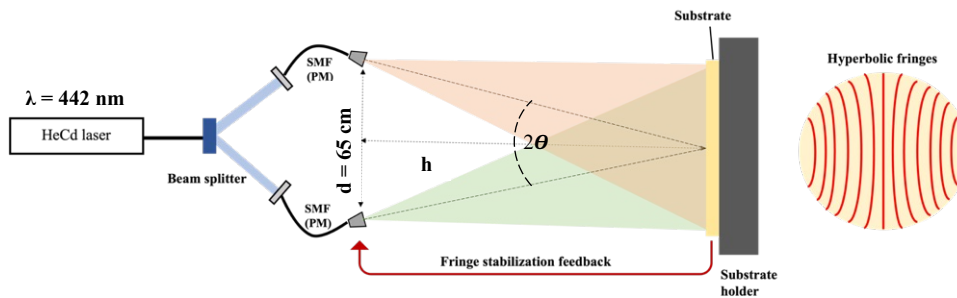


Figure 3.1. LIL setup with spherical wavefronts forming hyperbolic fringes.

The approach of bending the substrate during the exposure to correct for this period chirp was proposed by Walsh and Smith [14] in 2003. By applying a spherical curvature, they already showed a reduction of the period chirp, although no complete elimination could be achieved. The reason for this was investigated by Bienert et al., who showed that a spherical bending could not create an ideal compensation for the chirp [164]. The ideal surface to obtain the “zero-chirp” geometry is given by the rotation of the solution of a first-order differential equation [167]. However, Bienert et al. also showed that a spherical

deformation already reduces the chirp while having the advantage of comparatively easy mechanical implementation. For this reason, we also chose spherical deformation.

To calculate the expected period distribution, we used the approach shown by Bienert et al. for the exposure case considering an arbitrarily shaped substrate exposed by convex wavefronts emitted by arbitrarily positioned point sources [167]. Using this formalism, the period on a point P on the substrate is calculated by

$$\Lambda = \frac{\lambda \sqrt{1 - \left(\frac{\vec{a}_S \cdot \vec{g}_{vex}}{|\vec{a}_S| \cdot |\vec{g}_{vex}|} \right)^2}}{\frac{\vec{a}_S \cdot \vec{a}_A}{|\vec{a}_S| \cdot |\vec{a}_A|} - \frac{\vec{a}_S \cdot \vec{a}_B}{|\vec{a}_S| \cdot |\vec{a}_B|}}. \quad (3.1)$$

where λ is the wavelength and \vec{a}_A and \vec{a}_B are the vectors connecting the point sources and the point P, given as

$$\vec{a}_A = \overrightarrow{AP} \quad (3.2)$$

and

$$\vec{a}_B = \overrightarrow{BP}. \quad (3.3)$$

The vectors \vec{a}_S and \vec{g}_{vex} are given by

$$\vec{a}_S = \vec{n}_S \times (\vec{a}_B \times \vec{a}_A). \quad (3.4)$$

and

$$\vec{g}_{\text{vex}} = \left((\vec{a}_B \times \vec{a}_A) \times \left(\frac{\vec{a}_A}{|\vec{a}_A|} + \frac{\vec{a}_B}{|\vec{a}_B|} \right) \right) \times \vec{n}_S. \quad (3.5)$$

while \vec{n}_S is the normal vector at the point P, as shown in Fig. 3.2.

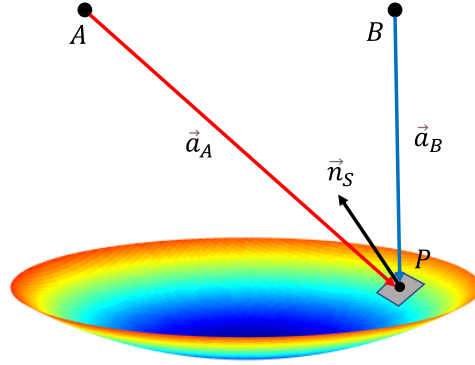


Figure 3.2. Sketch of the spherically curved substrate with a good point P and its average vector \vec{n}_S indicating the parameters used in Eqn. (3.1) to (3.5).

The laser source used to pattern the grating is a continuous wave HeCd laser source at a wavelength of 442 nm of output power 200 mW, and the distance (d) between the two single-mode fiber arms is 65 cm from Fig. 3.1. The aim period is 1000 nm. The expected period distributions for a 4-inch grating for both flat and curved exposure are calculated using the presented equations. Fig 3.3(a) shows the case of flat exposure where the maximum period increase is around 1.5 nm. In the case of curved exposure, shown in Fig 3.3(b), the period chirp is smaller, having a maximum period variation of only 0.4 nm.

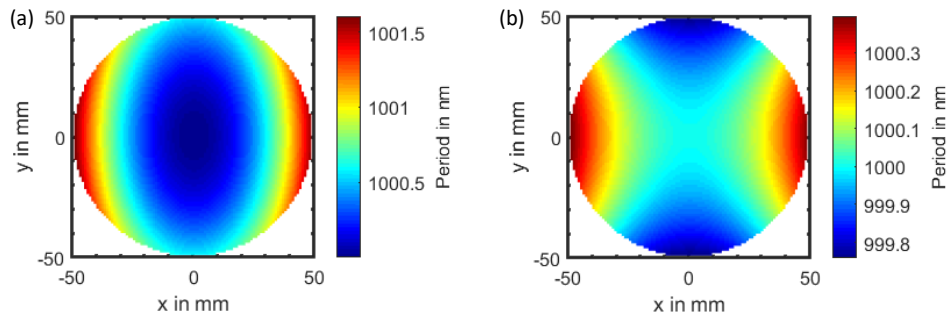


Figure 3.3. Calculated period distributions with the equations from Bienert et al. [165]. The color scale indicates the period. (a): Flat substrate. (b): Curved substrate with a radius of curvature of 1000 mm.

3.2.2. Bending on a flat substrate

To obtain the desired curvature of the substrate, a concave vacuum chuck is custom-made using aluminum alloy-3D printing. As shown in Fig. 3.4 (a-b), the substrate on the concave chuck will take the curvature shape upon applying the vacuum beneath the substrate. To achieve the substrate bending successfully, the wafer must be flexible with a thickness of 525 μm compared to its size of 4 inches. The lowest ratio of substrate thickness to its size will yield elastic deformation without the breakage of the substrate [165]. The radius of curvature of the concave vacuum chuck is designed for 100 cm. For good quality large-area gratings, the wafer must be of a planar surface. The effect of deformation on the silicon wafer can be determined using optical profilometry.

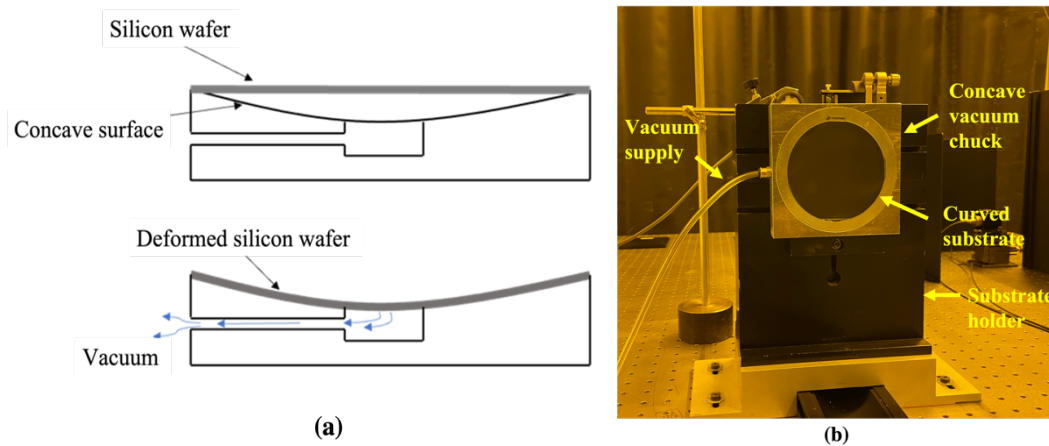


Figure 3.4. (a) Sketch of the bending process of a silicon wafer by concave vacuum chuck. (b) Image of concave vacuum chuck mounted on substrate holder stand with silicon wafer curved using vacuum supply.

3.3. Experimental demonstration of period variation reduction

3.3.1. Period variation of flat exposure vs. curved exposure

This section presents the experimental results by carrying out a series of grating period measurements on both flat exposed and curved exposed 4-inch gratings samples at central periods of 500 nm, 600 nm, 700 nm, 800 nm, 900 nm, and 1000 nm. For the fabrication part, 4-inch silicon wafers of 525 μm are coated with S1805 positive photoresist of the thickness of about 600 nm by spin coating. The photoresist-coated wafer is exposed to the interference fringes for 3 minutes and developed using MF-319 developer at room temperature 21°C for 5 seconds, as seen in Fig. 3.5. The exposure was performed using a flat vacuum chuck and a concave vacuum chuck of 100 cm curvature radius.

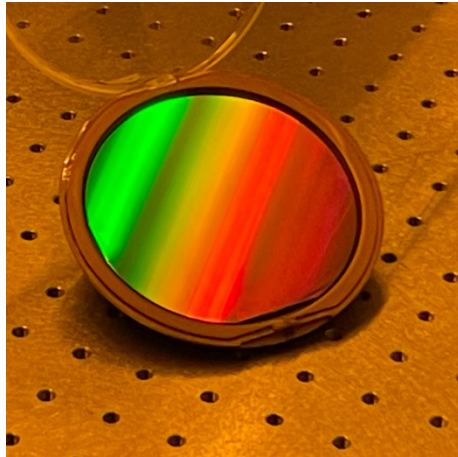


Figure 3.5. Photograph of fabricated photoresist grating on a 4-inch silicon wafer of thickness 525 μm using concave vacuum chuck holder by two-spherical-beam 442 nm LIL setup with an exposure time of 3 minutes and developing time of 5 seconds at 21°C.

The period measurements of the patterned 4-inch wafer samples are measured along the x-axis and y-axis using the Littrow configuration optical set-up as shown in Fig. 3.6 [These measurements were performed at IFSW with the help of ESR 1].

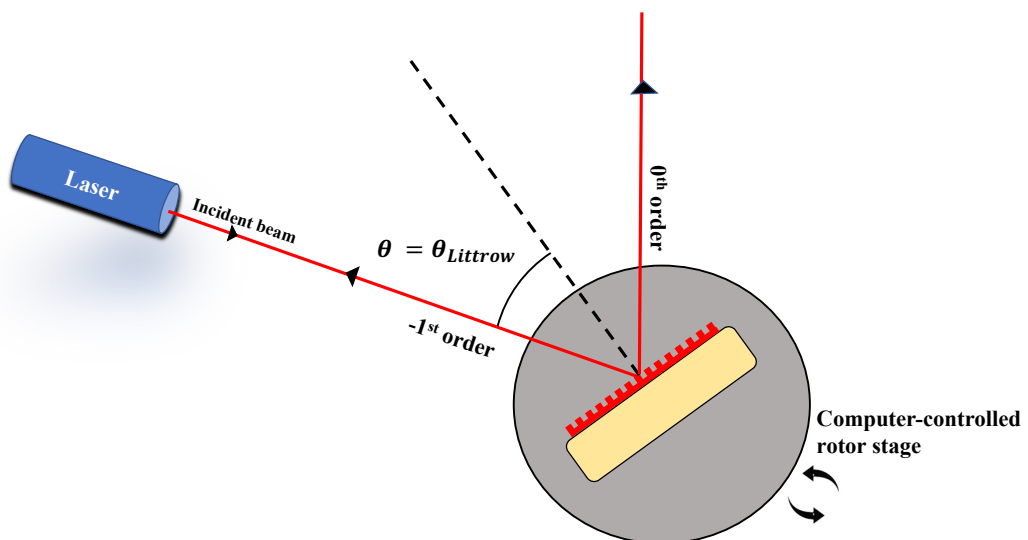


Figure 3.6. Schematic of diffraction period measurement at Littrow configuration.

The Littrow configuration is a particular setup of grating orientation to ensure the diffraction angle of reflected 1st order is equal to the incident beam. The Littrow equation is theoretically calculated by

$$\theta_{Littrow} = \theta = \sin^{-1}\left(\frac{\lambda}{2\Lambda}\right) \quad (3.6)$$

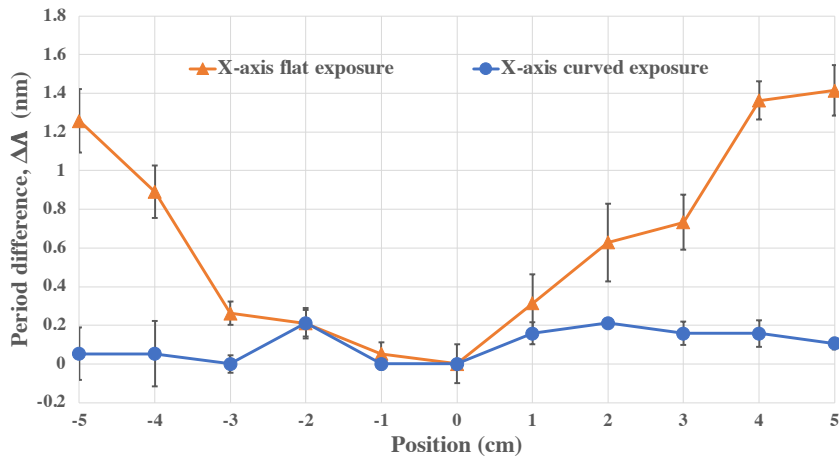
where θ is the incident beam angle and $\theta_{Littrow}$ is the Littrow angle at which the reflected -1st order coincides with the incident beam.

When the laser beam at wavelength 632.8 nm is incident on the grating sample, the sample is rotated to have diffracted -1st order coincides with the incident beam. The rotating angle gives the Littrow angle needed to calculate the localized grating period using Eq. 3.6. The data obtained are plotted for the period variation along the x-axis and y-axis concerning the position of the wafer sample.

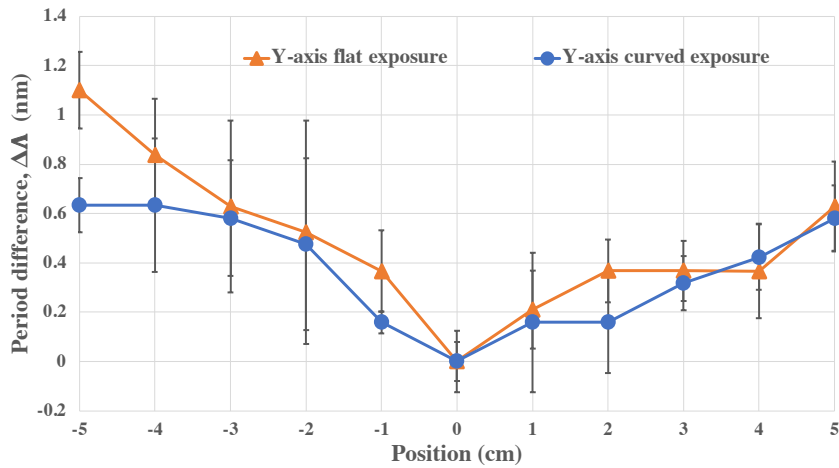
In Fig. 3.7 (a-b), the period variation of the grating sample at the central period of 1000 nm is shown for the flat exposure and curved exposure along the x-axis and y-axis. For the measurement along the x-axis, as shown in Fig. 3.7(a), the period variation of the flat exposed sample is 1.41 nm. With curved exposure, the period variation is reduced by 86%, with a maximum period variation of 0.2 nm. The error bars indicate the uncertainty observed during the experiment, with the Littrow angle varying due to the diffraction order beam spot resolution limit.

The measurement for period variation is carried out along the y-axis for both flat exposed and curved exposed wafer samples, as shown in Fig. 3.7(b). The period variation for flat and curved exposed samples is nearly identical. The period variation correction is

24% with curved substrate exposure. The period variation reduction is insignificant with curved exposure compared to the simulated result for the y -axis in Fig. 3.3.



(a)



(b)

Figure 3.7. A measured period variation along the x -axis (a) and y -axis (b) on the silicon wafer exposed by two spherical waves at the central period of 1000 nm. The orange plot (\blacktriangle) is the period variation on the flat exposed substrate. The blue plot (\bullet) is the period variation on the curved exposed substrate. The error bars indicate the uncertainty in the diffraction angle measurements.

The period measurement is repeated for the grating samples fabricated with 500 nm, 600 nm, 700 nm, 800 nm, and 900 nm central period. The measured data showed a significant reduction in period variation with grating fabricated with curved exposure by concave chuck, as shown in Table 3.1.

Central grating period (nm)	Measured maximum period variation for flat exposure (nm)	Measured maximum period variation for curved exposure (nm)
500	1.91	0.54
600	1.86	0.27
700	1.67	0.18
800	1.51	0.38
900	1.43	0.35
1000	1.41	0.20

Table 3.1. Measured values of maximum period variation along the x -axis for flat and curved exposure on 4-inch silicon wafer substrates from 500 nm to 1000 nm central grating period settings using LIL setup at laser wavelength 442 nm with fiber arms.

3.3.2. Period variation at different grating period settings

The influence of different grating period settings in the two spherical-beam LIL optical setups on the period variation is studied by patterning the 4-inch wafer samples for grating periods 500 nm, 600 nm, 700 nm, 800 nm, 900 nm, and 1000 nm. The samples were patterned using both flat chuck and concave vacuum chuck. From Fig. 3.8, it is shown that period variation is more significant for the lower grating period setting. This is due to the interference angle of the two beams increasing at the lower grating period than in the larger period setting. The curved exposed wafer samples show an excellent reduction in the period variation irrespective of the grating period settings.

It can be observed from Fig. 3.8 that the measured period variation values for curved exposed substrates indicated by the blue dotted line (●) agree well with a parabolic fitted simulation value indicated by the blue solid line (■). This proves the parabolic shape bending during the deformation process rather than the spherical curvature shape. The parabolic shape can be facilitated due to the vacuum hole present only at the center, which also proved true from section 3.4.

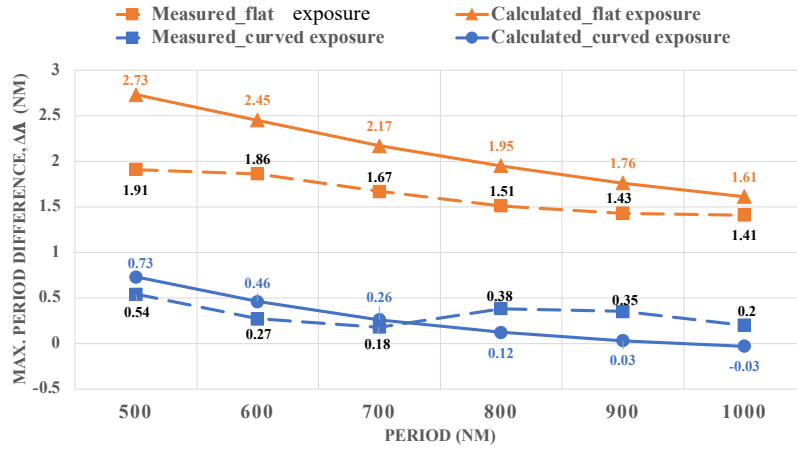


Figure 3.8. Calculated and measured maximum period variation along the x -axis of the flat- and curved-exposed substrates for the grating period varying from 500 nm to 1000 nm. The solid orange plot (▲) is the calculated maximum period variation, and the dotted plot (■) is the measured maximum period variation on the flat exposed substrates. The solid blue plot (●) is the estimated maximum period variation, and the dotted plot (■) is the measured maximum period variation on the curved exposed substrates.

3.3.3. Period variation reduction using two LIL configurations

A concave vacuum chuck was implemented, and the measured period variation reduction was compared in two different LIL setups. The difference in the two LIL configurations is given by their laser source employment and the optical element used for beam exiting, as specified in the Table. 3.2.

Key difference	Setup 1	Setup 2
Laser source	HeCd laser at 442 nm	Nd: YAG laser at 266 nm
Two beams exiting from	Single mode polarisation maintaining fibers	Pinholes
Grating period setting	The different periods are set with varying h and constant d as in Fig.3.1.	The different periods are set with varying d and constant h .

Table. 3.2. Key differences between the two LIL configurations.

The period variation reduction with a 266 nm LIL setup is seen to be much better compared to the 442 nm LIL setup due to the shorter wavelength resulting in less divergence of beams, and the large distance between the sources will approximate the spherical waves to planar waves by increasing the source and substrate holder distance.

In Fig. 3.9, the orange plot (\blacktriangle) shows the flat exposure of the wafer sample on a 442 nm LIL setup. The blue plot (\bullet) indicates the flat exposure of the wafer sample at the 500 nm grating period setting on the 266 nm LIL setup. It is evident from the figure that the period variation of the flat exposed grating sample obtained by the 266 nm LIL setup shows a substantial reduction in the period variation with a maximum period variation of 0.40 nm.

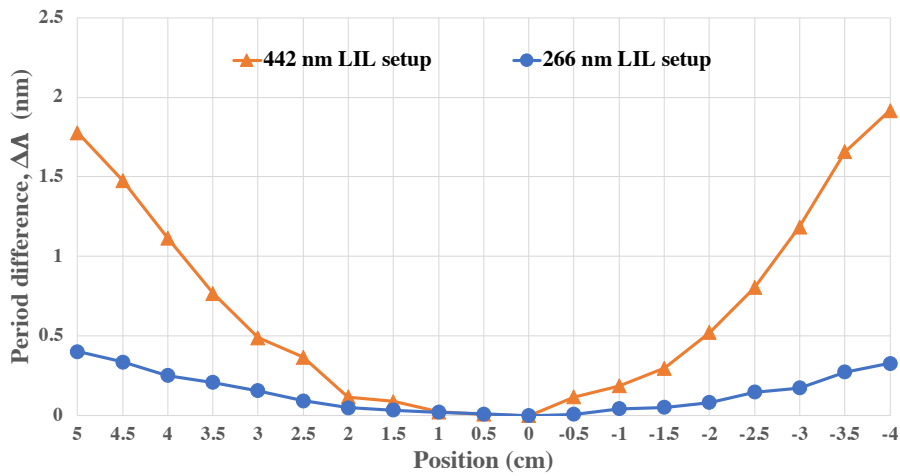


Figure 3.9. A measured period variation on the x-axis of the flat exposed substrate with two LIL optical set-ups for the grating period of 500 nm. The orange plot (\blacktriangle) is the period variation on the flat exposed substrate using a 442 nm LIL setup. The blue plot (\bullet) is the period variation on the flat exposed substrate using a 266 nm LIL setup.

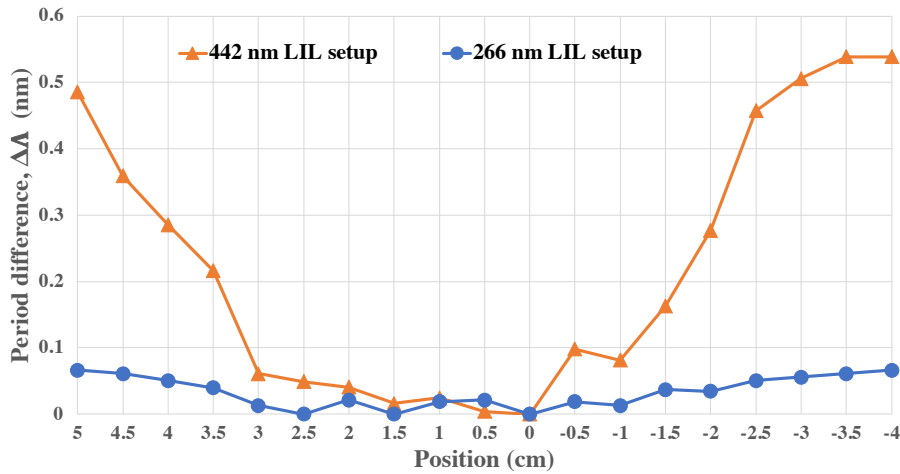


Figure 3.10. A measured period variation on the x-axis of the curved exposed substrate with two LIL optical set-ups for the grating period of 500 nm. The orange plot (\blacktriangle) is the period variation on the curved exposed substrate using a 442 nm LIL setup. The blue plot (\bullet) is the period variation on the curved exposed substrate using a 266 nm LIL setup.

The period variation is further improved in the 266 nm LIL setup by implementing the concave vacuum chuck. From Fig. 3.15, the period variation of the curved exposed

sample on 266 nm LIL setup with a maximum period variation of 0.06 nm (72%) at the edge is much lower than the curved exposed sample on 442 nm LIL setup with a maximum period variation of 0.54 nm (83%). Using the LIL configuration with the shorter wavelength laser source is ideal for obtaining near-perfect linear gratings on a large thin substrate.

3.4. Substrate flatness analysis by optical profilometry

The after-effect of the temporary deformation process of silicon wafers using a concave vacuum chuck on the flatness of the substrate itself was studied using optical profilometry [This analysis was performed with the help at Manutech Usd, Saint-Etienne, France]. The surface topology is measured using the profilometer *CHRocodile S* by *Precitec* with the chromatic sensor of the measurement range of 1 mm. The sensor has a numerical aperture of 0.7 and a resolution of 35 nm along a vertical direction. The thin thickness of the 4-inch silicon wafer compared to its surface diameter provide good flexibility during the bending treatment. In Fig. 3.11(a)-(b), the plot shows the deflection height in the center of the substrate during the deformation. The maximum deflection height is measured to be 1.10 mm without the wafer breakage.

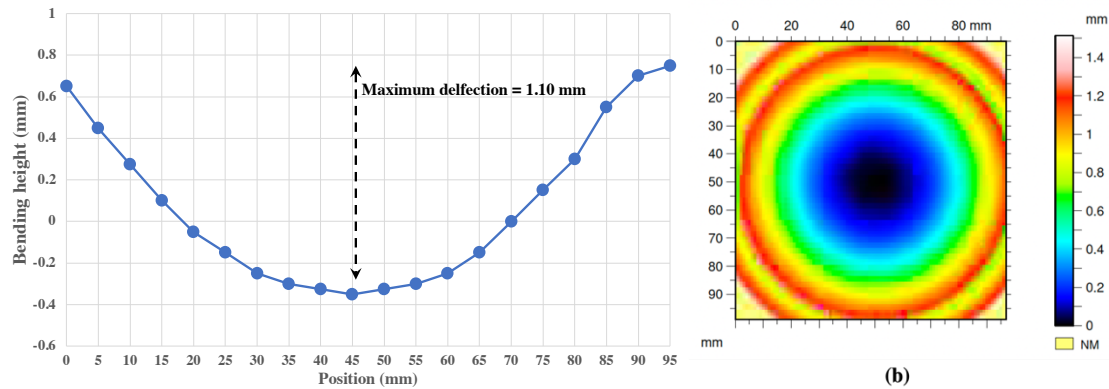


Figure 3.11. Optical profilometry (a) measurement data of deformed 4-inch silicon wafer during the vacuum treatment. (b) Surface topography of the wafer during the vacuum treatment. The maximum deflection at the center of the wafer is 1.10 mm.

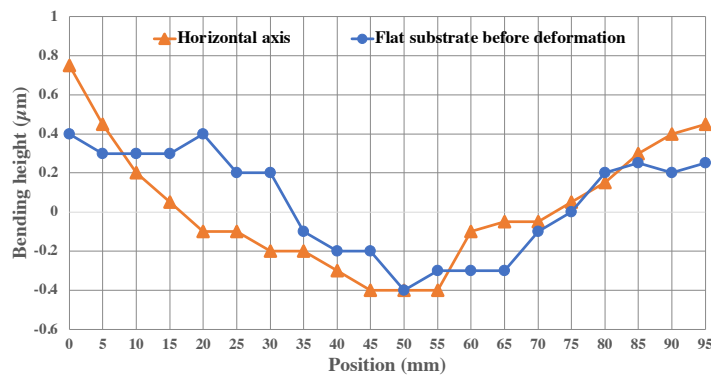


Figure 3.12. Optical profilometry measurement data of deformed 4-inch silicon wafer after the vacuum treatment for 30 minutes. The orange plot (\blacktriangle) is the flatness of the wafer measured along the horizontal axis with a maximum deviation of 1.17 μm . The blue plot (\bullet) is the flatness of the wafer along the horizontal axis with a maximum deviation of 0.80 μm .

The profilometry measurement was made after the bending treatment of the wafer sample for 30 minutes. As shown in Fig. 3.12, the horizontal axis indicated by the orange plot (\blacktriangle) on the substrate maintains good flatness with a deviation of 1.17 μm compared to the measurement before the vacuum treatment indicated by the blue plot (\bullet) with a maximum deviation of 0.8 μm .

3.5. Wavefront aberration analysis by adaptive wavefront interferometry

This investigation aims to show the quality of the gratings produced by measuring the reconstructed planar wavefront from the grating samples [This task was performed at ITO with the help of ESR 8]. The measurement setup used here is called adaptive wavefront interferometry. This technique is based on Twyman–Green interferometry principle developed by Frank Twyman and Arthur Green [166]. The working setup is illustrated in Fig. 3.13. The beam from the laser source of 632.8 nm is expanded and collimated by optical lenses to produce a parallel beam. The parallel beam is split into two beams using a beam splitter. One part of the beam passes through the test grating sample and is reflected from the plane mirror. The recombination of the beams is recorded using an imaging system to study how perfectly straight the lines of the grating (grating linearity) are by analyzing the wavefront aberration.

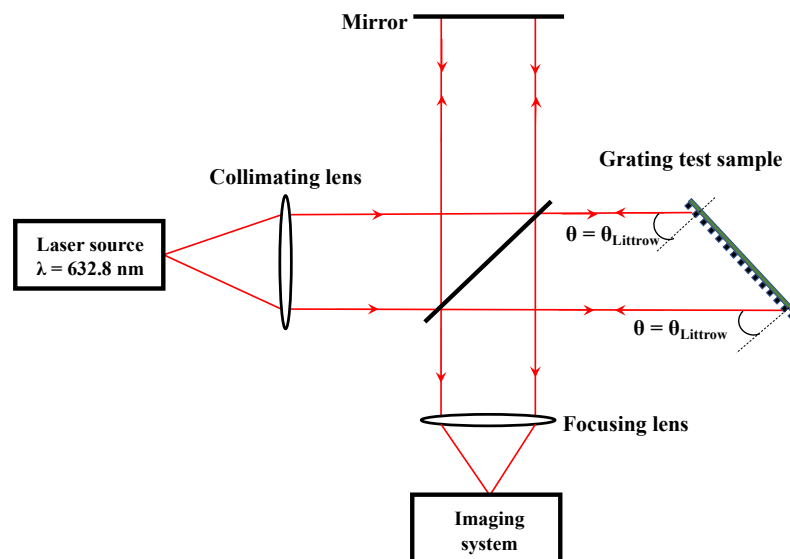


Figure. 3.13. The working setup of adaptive wavefront interferometry.

In the ideal case, the wavefront from gratings with perfect linear lines on a flat surface will have no aberration. The aberration caused by the grating samples is measured by two parameters, peak-to-valley (PV) and Root Mean Square (RMS). P-V and RMS values indicate the difference between the actual grating sample and an ideal flat optical surface. P-V measures the difference between the highest and lowest points on the grating sample, and RMS is the average deviation over the grating sample surface from the ideal flat surface. The combination of P-V and RMS will provide a good understanding of the quality of the gratings. The quality of the grating samples is better with lower P-V and RMS values. P-V and RMS are expressed in linear units (commonly in units of wavelength). In this experiment, the wavefront aberration is caused by two sources. First, the straightness error of the grating lines in the grating samples. Second, the deviation error of the substrate flatness from a perfectly planar substrate. Both errors are added up in the standard measurement and cannot be separated. To obtain information on the straightness error of the grating lines, the wavefront reconstruction is measured in complementary diffraction -1st orders at their Littrow configuration and subtracted from each other, canceling the deviation error resulting in the effect of straightness error of grating lines.

The equipment used for the wavefront aberration measurement is an interferometer by Schneider ALi 200 with Fisba μ Phase DCI2 with a plane wave of 150 mm diameter. The measured data of surface deviation is retrieved by the reconstructed planar wavefront, as shown in Fig. 3.14(a-b). The wavefront reconstruction from the 4-inch gratings fabricated at the central grating period of 1000 nm was recorded by wavefront aberration measurement using a laser at $\lambda = 632.8$ nm. The flat exposed substrate wavefront

reconstruction shows a P-V value of 24.18λ and an RMS value of 3.33λ ; the curved exposed substrate wavefront reconstruction has a P-V value of 8.22λ and an RMS value of 1.31λ . Although aberration is present both in flat and curved exposed grating substrates, the curved exposed substrate relatively showed 2.5 times better P-V and RMS values than the flat exposed substrate. This investigation showed that the curved exposed grating samples would have better linearity of grating lines.

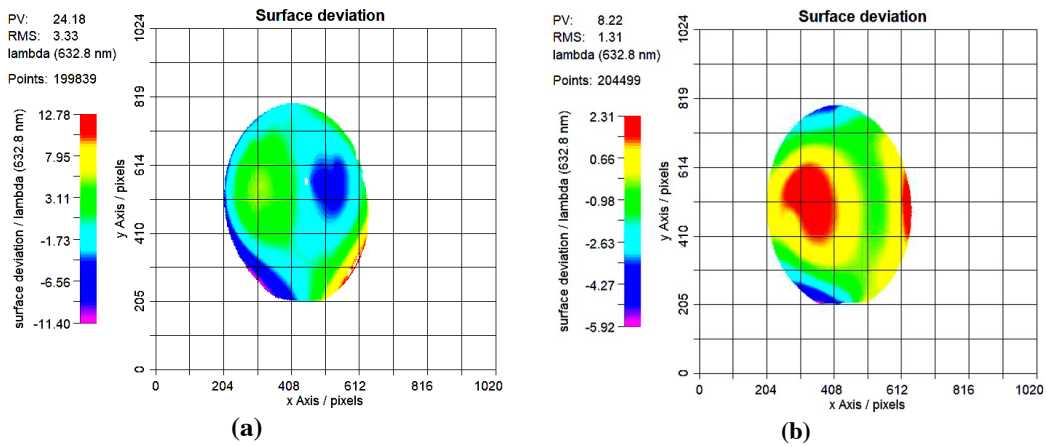


Figure 3.14. The surface deviation of the 4-inch substrate at the central period of 1000 nm was recorded by wavefront aberration measurement using a laser at $\lambda = 632.8$ nm (a) For flat exposed grating, P-V is 24.18λ , and the RMS value is 3.33λ . (b) For curved exposed grating, P-V is 8.22λ , and the RMS value is 1.31λ .

3.6. Conclusion

This chapter experimentally demonstrated the period variation reduction process for the 4-inch silicon wafer grating samples fabricated using a two-spherical-beam LIL setup [168]. First, the theoretical foundation was established to define the period variation issue on flat surface gratings. The analytical solution to reduce the period variation is then derived, and the concave vacuum chuck needed for the period variation correction is customized made for a 100 cm radius of curvature using the 3D printing technique. The

concave chuck is then used to fabricate a wide range of gratings with different grating period settings from 500 nm to 1000 nm using a LIL setup with a laser source at 442 nm.

The period measurement of wafer samples patterned using flat and concave chuck was studied and compared. The period variation in the flat exposed grating substrate along the x -axis had a maximum period variation of 1.41 nm at the 1000 nm central grating period setting. The period variation was reduced by 85% on a curved exposed grating substrate. The period variation reduction is further improved by implementing the concave vacuum chuck in the LIL setup with pinholes and a shorter laser wavelength of 266 nm. The maximum period variation with the combination of concave chuck and 266 nm laser source LIL setup was measured to be 0.06 nm at a 500 nm central grating period setting. The substrate flatness was verified using the optical profilometry measurement. The maximum deviation on the surface after the bending process was 1.17 μm along the horizontal axis compared to the maximum deviation of 0.80 μm on a flat surface before the bending process. This shows a slight flatness deviation and can be ignored compared to the substrate size of 10 cm.

Finally, the quality of the grating lines for their straightness in the grating samples was analyzed by measuring the wavefront aberration from the reconstructed wavefront using an adaptive wavefront interferometry setup with a working laser at $\lambda = 632.8$ nm. The flat exposed substrate had a P-V value of 24.18λ and an RMS value of 3.33; the curved exposed substrate had a P-V value of 8.22λ and an RMS value of 1.31λ . The curved exposed substrate showed 2.5 times better P-V and RMS values than the flat exposed substrate. Hence, we can produce a good quality grating with low straightness error on a

large silicon wafer substrate by performing curved substrate exposure using a concave vacuum chuck during the LIL patterning process.

General Conclusion

The aim of this thesis work involved realizing the grating structures by carrying out three tasks. The first task was fabricating GWS using the direct patterning method by the LIL technique for spectral and polarization stabilization and wavelength multiplexing in two different laser systems: diode lasers emitting at 976 nm and solid-state lasers emitting at 1 μm . Using LIL, the second task was fabricating Si master gratings on 2-inch Si wafers. The last task was to experimentally prove the potential of reducing period variation on 4-inch silicon grating samples using a substrate bending approach proposed by Walsh and Smith [34].

Chapter 1 provided a bibliographic work of GWS, presenting its importance and recent advancements in high-power laser applications. The presentation of the GREAT project and its objectives established a clear motivation and hierarchy in delivering the GWS for different applications (A1 to A5). The theoretical section with the working principle of GWS as a combination of diffraction gratings and the multilayer stacked film set a base for understanding the importance of geometrical parameters of the grating structures and the multilayers to achieve a high resonance response.

In chapter 2, to achieve our objectives in fabricating the grating structures, the first step was to design the grating parameters of the three target design for applications (A3 and A4) using commercial simulation software such as *MC gratings* and *Microsim*. The associated Diffraction Efficiency response was computed using an RCWA-based

algorithm along with their tolerance concerning the grating period, Duty Cycle, and grating depth. The simulated tolerance was specified for the acceptable fabrication deviation. The design parameters are then used in the fabrication of grating structures by two fabrication process flows:

- a) The first fabrication process involved the fabrication of grating structures directly on BARC and negative photoresist-coated multilayer film stack, called the direct patterning LIL technique. The patterned grating structures are then etched onto BARC, followed by Cr and the top layer of the multilayer stack using the RIE process. The etching of the SiO₂ top layer corresponds to the low-index GWS sample used for the A3 application. The etching of the Nb₂O₅ top layer and partial SiO₂ layer corresponds to the high-index GWS sample used for the A3 application. The etching of the Nb₂O₅ top layer corresponds to the high-index GWS sample used for the A4 application.
- b) The second fabrication process involved the fabrication of grating structures on 2-inch Si wafers to produce Si masters. The Si masters were fabricated by patterning with LIL on BARC and negative photoresist coated wafers and then dry etching the grating structures onto BARC, followed by the Si layer using the SiO₂ etching recipe.

The fabricated GWS and Si masters were characterized by their geometrical properties using AFM, SEM, and period variation measurements. The parameters of fabricated GWS samples were not the same as the design parameters. The fabricated GWS samples for the A3 A4 applications showed an average of 28% deviation in the Duty Cycle. However, the deviation in the grating period and the grating depth was minimal. The final samples also suffered from the Cr residual caused during the etching process.

The fabricated GWS samples and Si masters for A3-A4 applications also suffered from the varying grating depth and Duty Cycles and non-uniform grating periods across the sample area. The samples showed an average variation of 6.7 % in the Duty Cycle and 18 nm in the grating depth. The maximum period variation evaluated along the x -axis was 0.59 nm, and the y -axis was 0.24 nm. The fabricated Si master samples for A3 and A4 applications showed an average variation of 6.4 % in the Duty Cycle and 11.3 nm in the grating depth. The maximum period variation evaluated with Si masters for A3 applications along the x -axis was 1.49 nm, and the y -axis was 1.12 nm.

For the Si master sample used for the A4 application, the maximum period variation measured along the x -axis is 0.08 nm. The maximum period variation measured along the y -axis is 0.07 nm. The period variation of this Si master sample was noticed to be much lower due to the implementation of the curved sample LIL exposure technique, which improved the uniformity of the grating period.

The parameter deviations demonstrated their influence on the DE response of the GWS by presenting the measured DE of high-index GWS for the A4 application. The DE of the measured sample was 91.88% for TE -1st order at 1030 nm. The losses in DE were due to the strong deviation in the fabricated GWS parameters from the designed parameters with a grating period deviation of 4.5 nm, grating depth deviating by 8 nm, and Duty Cycle by 20%. The fabricated GWS and Si masters also suffered from the non-uniform grating depth due to the gaussian energy distribution of interference fringes during the LIL patterning. The combined factors of nonuniform grating development in LIL and the deviation in the fabricated grating parameters from the design parameters will result in a loss in DE and damage GWS when implemented in a high-power laser system. The

fabricated samples showed variations in the grating period measured along the x - and y -axis. The period variation was due to the interference fringes formed by the diverging spherical beam in the LIL setup. The substrate bending approach using a concave vacuum chuck was implemented on Si master grating for a 1030 nm solid-state laser. The period variation was significantly low, with the measured values of 0.08 nm along the x -axis and 0.07 nm along the y -axis. This experimental proof was the motivation to investigate further the substrate bending approach in 4-inch Si substrate gratings in the final chapter.

In the final chapter, a quantitative investigation on reducing the period variation of 4-inch Si substrate was carried out based on the substrate bending approach proposed by Walsh and Smith [34]. In two ways, the photoresist grating structures were patterned by LIL setup with a 442 nm laser source on 4-inch Si substrates. Firstly, the conventional flat substrate LIL exposure using a flat vacuum chuck as substrate holder. Secondly, the substrate was temporarily bent into a curved shape during the LIL exposure using a custom-made concave vacuum chuck of 4-inch diameter with a curvature radius of 100 cm. The accurate period of fabricated flat and curved exposed grating substrates was measured along the x -axis and y -axis using period measurement setup at Littrow configuration. The measured data showed a significant reduction of period variation in curved exposed substrates with an average 80% reduction at different grating period settings. The period variation is further reduced by using a concave vacuum chuck combined with a pinhole LIL setup of a shorter wavelength laser source of 266 nm. The maximum period variation was 0.06 nm at a 500 nm central grating period setting in the x -axis. The substrate flatness was measured using the optical profilometry measurement. The maximum deviation on the surface after the bending process was 1.17 μm along the

horizontal axis compared to the maximum deviation of 0.80 μm on a flat surface before the bending process. The quality of the grating lines for their straightness in the grating samples was verified by measuring the wavefront aberration from the reconstructed wavefront using an adaptive wavefront interferometry setup with a working laser at $\lambda = 632.8 \text{ nm}$. The curved exposed substrate showed 2.5 times better P-V and RMS value than the flat exposed substrate.

The work performed throughout this thesis enables us to conclude the outcome from the following perspectives:

- a) Based on the above evaluation, the grating fabrication by the LIL technique did not efficiently improve the DE of GWS to meet the standard goal of the GREAT project. However, the LIL technique remains the potential fabrication technique to pattern gratings faster and more cost-effectively and free of fabrication errors like stitching errors and proximity effect observed in the E-beam lithography. LIL can be compared to the SBIL technique similarly, with SBIL capable of grating patterns with good uniformity but still suffering from stitching errors and writing time. The other technique, such as the NIL process, overcomes this stitching error and long writing time and benefits from fast and mass-producible grating structures. But this process still has a major issue with a random bald spot during the printing process, and NIL relies on other fabrication techniques like E-beam and LIL for the grating master. Considering the above-mentioned advantages of LIL over other fabrication techniques, plus establishing strict process control, uniform grating structures are achievable, which will be the objective for future work in the GREAT project.

b) To optimize the LIL technique to achieve uniform gratings structures, several grating parameters need to be addressed. In this work, the improvement of the grating period was focused on by reducing the period variation across the sample area with a curved exposure technique using a concave vacuum chuck. The reduction in the period variation was carried out only on Si wafer substrate since Si wafers are flexible and can be bent temporarily without damage. The experimental results obtained by bending 4-inch Si substrates during the LIL exposure proved the significant reduction in the period variation compared to the flat substrate LIL exposure. This quantitative investigation has set the promising technique to improve the grating period uniformity on Si substrates, which play an important role in making gratings structures replicas during the NIL process. For future work, the next approach in optimizing the LIL technique is to improve the Duty Cycle and grating depth uniformity by addressing the gaussian intensity distribution of interference fringes during the LIL exposure.

Bibliography

- [1] M. A. Ahmed, M. Rumpel, A. Voss, and T. Graf, "Applications of sub-wavelength grating mirrors in high-power lasers," *Advanced Optical Technologies* **1**(5), (2012).
- [2] D. González-Andrade, A. Dias, J. G. Wangüemert-Pérez, A. Ortega-Moñux, Í. Molina-Fernández, R. Halir, P. Cheben, and A. V. Velasco, "Experimental demonstration of a broadband mode converter and multiplexer based on subwavelength grating waveguides," *Optics & Laser Technology* **129**, 106297 (2020).
- [3] M. Rumpel, M. Moeller, C. Moormann, T. Graf, and M. A. Ahmed, "Broadband pulse compression gratings with measured 997% diffraction efficiency," *Opt. Lett.* **39**(2), 323 (2014).
- [4] M. Rumpel, M. Möller, C. Moormann, A. Voss, T. Graf, and M. Abdou-Ahmed, "Demonstration of grating mirrors with high diffraction efficiency for pulse compression," in *Advanced Solid-State Lasers Congress (OSA, 2013)*, p. ATh1A.7.
- [5] M. Rumpel, M. Abdou Ahmed, A. Voss, and T. Graf, "Grating waveguide structures for intracavity generation of beams with azimuthal polarization in an Yb:YAG thin-disk laser," in T. Graf, J. I. Mackenzie, H. Jelínková, and J. Powell, eds. (2012), p. 84331A.
- [6] M. Rumpel, M. Abdou Ahmed, A. Voss, and T. Graf, "High-efficiency wavelength and polarization selective grating-waveguide structures for Yb:YAG thin-disk lasers," in T. Graf, J. I. Mackenzie, H. Jelínková, and J. Powell, eds. (2012), p. 84331D.
- [7] M. A. Ahmed, M. Haefner, M. Vogel, C. Pruss, A. Voss, W. Osten, and T. Graf, "High-power radially polarized Yb:YAG thin-disk laser with high efficiency," *Opt. Express* **19**(6), 5093 (2011).
- [8] C. Pérez-Armenta, J. Čtyroký, P. Cheben, J. H. Schmid, A. Ortega-Moñux, R. Halir, I. Molina-Fernández, and J. G. Wangüemert-Pérez, "A Design Methodology for

- Resonant Sensors based on Subwavelength Grating Waveguides at 1.31 μm ," in Optical Sensors and Sensing Congress (OSA, 2020), p. SW3F.1.
- [9] N. Destouches, A. V. Tishchenko, J. C. Pommier, S. Reynaud, O. Parriaux, S. Tonchev, and M. A. Ahmed, "99% efficiency measured in the -1st order of a resonant grating," *Opt. Express* **13**(9), 3230 (2005).
- [10] G. Quaranta, G. Basset, O. J. F. Martin, and B. Gallinet, "Recent Advances in Resonant Waveguide Gratings," *Laser & Photonics Reviews* **12**(9), 1800017 (2018).
- [11] A. Boubekraoui, F. Beirow, T. Graf, and M. Abdou Ahmed, "Intra-cavity wavelength multiplexing of high-brightness thin-disk laser beams," *Appl. Phys. B* **128**(7), 120 (2022).
- [12] S. Pricking, F. Baumann, S. Zaske, E. Dold, E. Kaiser, and A. Killi, "Progress in green disk laser development for industrial high power applications," in *Solid State Lasers XXX: Technology and Devices*, W. A. Clarkson and R. K. Shori, eds. (SPIE, 2021), p. 13.
- [13] J. Pinto, R. Aylwin, G. Silva-Oelker, and C. Jerez-Hanckes, "Diffraction efficiency optimization for multilayered parametric holographic gratings," *Opt. Lett.* **46**(16), 3929 (2021).
- [14] M. Rumpel, T. Dietrich, F. Beirow, T. Graf, and M. A. Ahmed., "Resonant Waveguide Gratings enable advanced designs of laser resonators," in *Laser Congress 2020 (ASSL, LAC)* (OSA, 2020), p. AW2A.5.
- [15] M. Rumpel, T. Dietrich, F. Beirow, T. Graf, and M. A. Ahmed, "Resonant Waveguide Gratings – Versatile Devices for Laser Engineering: Accurate tailoring of the spectral, temporal and spatial parameters of your laser systems," *PhotonicsViews* **17**(3), 50–55 (2020).
- [16] E. G. Loewen and E. Popov, *Diffraction Gratings and Applications*, 0 ed. (CRC Press, 2018).
- [17] M. Rumpel, F. Beirow, T. Graf, and M. Abdou Ahmed, "Design of grating waveguide structures for pulsed laser systems: Strategy to maximize the production

- yield given special characteristics of the production process," *PhotonicsViews* **19**(3), 56–59 (2022).
- [18] G. Levy-Yurista and A. A. Friesem, "Very narrow spectral filters with multilayered grating-waveguide structures," *Appl. Phys. Lett.* **77**(11), 1596–1598 (2000).
- [19] A. Sharon, H. G. Weber, H. Engel, D. Rosenblatt, A. A. Friesem, and R. Steingrueber, "Light modulation with resonant grating–waveguide structures," *Opt. Lett.* **21**(19), 1564 (1996).
- [20] M. A. Butt, C. Tyszkiewicz, K. Wojtasik, P. Karasiński, A. Kaźmierczak, and R. Piramidowicz, "Subwavelength Grating Waveguide Structures Proposed on the Low-Cost Silica–Titania Platform for Optical Filtering and Refractive Index Sensing Applications," *IJMS* **23**(12), 6614 (2022).
- [21] P. Poole, S. Trendafilov, G. Shvets, D. Smith, and E. Chowdhury, "Femtosecond laser damage threshold of pulse compression gratings for petawatt scale laser systems," *Opt. Express* **21**(22), 26341 (2013).
- [22] W. Li, Z. Gan, L. Yu, C. Wang, Y. Liu, Z. Guo, L. Xu, M. Xu, Y. Hang, Y. Xu, J. Wang, P. Huang, H. Cao, B. Yao, X. Zhang, L. Chen, Y. Tang, S. Li, X. Liu, S. Li, M. He, D. Yin, X. Liang, Y. Leng, R. Li, and Z. Xu, "339 J high-energy Ti:sapphire chirped-pulse amplifier for 10 PW laser facility," *Opt. Lett.* **43**(22), 5681 (2018).
- [23] J.-K. Rhee, J. A. Arns, W. S. Colburn, T. S. Sosnowski, and T. B. Norris, "Chirped-pulse amplification of 85-fs pulses at 250 kHz with third-order dispersion compensation by use of holographic transmission gratings," *Opt. Lett.* **19**(19), 1550 (1994).
- [24] T. J. Kessler, J. Bunkenburg, H. Huang, A. Kozlov, and D. D. Meyerhofer, "Demonstration of coherent addition of multiple gratings for high-energy chirped-pulse-amplified lasers," *Opt. Lett.* **29**(6), 635 (2004).
- [25] A. Sentenac and A.-L. Fehrembach, "Angular tolerant resonant grating filters under oblique incidence," *J. Opt. Soc. Am. A* **22**(3), 475 (2005).
- [26] Y. Luo, P. J. Gelsinger, J. K. Barton, G. Barbastathis, and R. K. Kostuk, "Optimization of multiplexed holographic gratings in PQ-PMMA for spectral-spatial imaging filters," *Opt. Lett.* **33**(6), 566 (2008).

- [27] A. Sevian, O. Andrusyak, I. Ciapurin, V. Smirnov, G. Venus, and L. Glebov, "Efficient power scaling of laser radiation by spectral beam combining," *Opt. Lett.* **33**(4), 384 (2008).
- [28] M. A. Ahmed, A. Voss, M. M. Vogel, and T. Graf, "Multilayer polarizing grating mirror used for the generation of radial polarization in Yb:YAG thin-disk lasers," *Opt. Lett.* **32**(22), 3272 (2007).
- [29] G. M. Lerman and U. Levy, "Generation of a radially polarized light beam using space-variant subwavelength gratings at 1064 nm," *Opt. Lett.* **33**(23), 2782 (2008).
- [30] M. A. Ahmed, J. Schulz, A. Voss, O. Parriaux, J.-C. Pommier, and T. Graf, "Radially polarized 3kW beam from a CO₂ laser with an intracavity resonant grating mirror," *Opt. Lett.* **32**(13), 1824 (2007).
- [31] S. M. Norton, G. M. Morris, and T. Erdogan, "Experimental investigation of resonant-grating filter lineshapes in comparison with theoretical models," *J. Opt. Soc. Am. A* **15**(2), 464 (1998).
- [32] S. Hocquet, J. Neauport, and N. Bonod, "The role of electric field polarization of the incident laser beam in the short pulse damage mechanism of pulse compression gratings," *Appl. Phys. Lett.* **99**(6), 061101 (2011).
- [33] L. Gallais, M. Rumpel, M. Moeller, T. Dietrich, T. Graf, and M. Abdou Ahmed, "Investigation of laser damage of grating waveguide structures submitted to sub-picosecond pulses," *Appl. Phys. B* **126**(4), 69 (2020).
- [34] M. E. Walsh and H. I. Smith, "Method for reducing hyperbolic phase in interference lithography," *J. Vac. Sci. Technol. B* **19**(6), 2347 (2001).
- [35] M. C. Gower, "Industrial applications of laser micromachining," *Opt. Express* **7**(2), 56 (2000).
- [36] R. Liu, Z. Wang, T. Sparks, F. Liou, and J. Newkirk, "Aerospace applications of laser additive manufacturing," in *Laser Additive Manufacturing* (Elsevier, 2017), pp. 351–371.
- [37] S. Seeger, S. Monajembashi, K.-J. Hutter, G. Futterman, J. Wolfrum, and K. O. Greulich, "Application of laser optical tweezers in immunology and molecular genetics," *Cytometry* **12**(6), 497–504 (1991).

- [38] Q. Peng, A. Juzeniene, J. Chen, L. O. Svaasand, T. Warloe, K.-E. Giercksky, and J. Moan, "Lasers in medicine," *Rep. Prog. Phys.* **71**(5), 056701 (2008).
- [39] S. Fritzler, V. Malka, G. Grillon, J. P. Rousseau, F. Burgy, E. Lefebvre, E. d'Humières, P. McKenna, and K. W. D. Ledingham, "Proton beams generated with high-intensity lasers: Applications to medical isotope production," *Appl. Phys. Lett.* **83**(15), 3039–3041 (2003).
- [40] U. Bergmann, V. Yachandra, and J. Yano, eds., *X-Ray Free Electron Lasers: Applications in Materials, Chemistry and Biology, Energy and Environment Series* (Royal Society of Chemistry, 2017).
- [41] R. X. Adhikari, "Gravitational radiation detection with laser interferometry," *Rev. Mod. Phys.* **86**(1), 121–151 (2014).
- [42] B. Willke, K. Danzmann, M. Frede, P. King, D. Kracht, P. Kwee, O. Puncken, R. L. Savage, B. Schulz, F. Seifert, C. Veltkamp, S. Wagner, P. Weßels, and L. Winkelmann, "Stabilized lasers for advanced gravitational wave detectors," *Class. Quantum Grav.* **25**(11), 114040 (2008).
- [43] P. Krötz, D. Stupar, J. Krieg, G. Sonnabend, M. Sornig, F. Giorgetta, E. Baumann, M. Giovannini, N. Hoyler, D. Hofstetter, and R. Schieder, "Applications for quantum cascade lasers and detectors in mid-infrared high-resolution heterodyne astronomy," *Appl. Phys. B* **90**(2), 187–190 (2008).
- [44] M. S. Brown and C. B. Arnold, "Fundamentals of Laser-Material Interaction and Application to Multiscale Surface Modification," in *Laser Precision Microfabrication*, K. Sugioka, M. Meunier, and A. Piqué, eds., Springer Series in Materials Science (Springer Berlin Heidelberg, 2010), **135**, pp. 91–120.
- [45] P. S. Mohanty and J. Mazumder, "Solidification behavior and microstructural evolution during laser beam—material interaction," *Metall Mater Trans B* **29**(6), 1269–1279 (1998).
- [46] X. Wang and X. Xu, "Molecular dynamics simulation of thermal and thermomechanical phenomena in picosecond laser material interaction," *International Journal of Heat and Mass Transfer* **46**(1), 45–53 (2003).

- [47] L. Yang, J. Wei, Z. Ma, P. Song, J. Ma, Y. Zhao, Z. Huang, M. Zhang, F. Yang, and X. Wang, "The Fabrication of Micro/Nano Structures by Laser Machining," *Nanomaterials* **9**(12), 1789 (2019).
- [48] X. Xie, C. Zhou, X. Wei, W. Hu, Q. Ren, 1.Laser Micro/Nano Processing Lab, School of Electromechanical Engineering, Guangdong University of Technology, Guangzhou 510006, China, and 2.Department of Experimental Teaching, Guangdong University of Technology, Guangzhou 510006, China, "Laser machining of transparent brittle materials: from machining strategies to applications," *Opto-Electronic Advances* **2**(1), 18001701–18001713 (2019).
- [49] D. K. Shanmugam, F. L. Chen, E. Siores, and M. Brandt, "Comparative study of jetting machining technologies over laser machining technology for cutting composite materials," *Composite Structures* **57**(1–4), 289–296 (2002).
- [50] H. D. Vora, S. Santhanakrishnan, S. P. Harimkar, S. K. S. Boetcher, and N. B. Dahotre, "Evolution of surface topography in one-dimensional laser machining of structural alumina," *Journal of the European Ceramic Society* **32**(16), 4205–4218 (2012).
- [51] T. Gissibl, S. Thiele, A. Herkommer, and H. Giessen, "Two-photon direct laser writing of ultracompact multi-lens objectives," *Nature Photon* **10**(8), 554–560 (2016).
- [52] M. Thiel, J. Fischer, G. von Freymann, and M. Wegener, "Direct laser writing of three-dimensional submicron structures using a continuous-wave laser at 532 nm," *Appl. Phys. Lett.* **97**(22), 221102 (2010).
- [53] Z.-L. Wu, Y.-N. Qi, X.-J. Yin, X. Yang, C.-M. Chen, J.-Y. Yu, J.-C. Yu, Y.-M. Lin, F. Hui, P.-L. Liu, Y.-X. Liang, Y. Zhang, and M.-S. Zhao, "Polymer-Based Device Fabrication and Applications Using Direct Laser Writing Technology," *Polymers* **11**(3), 553 (2019).
- [54] Y. Zhou, Q. Bao, B. Varghese, L. A. L. Tang, C. K. Tan, C.-H. Sow, and K. P. Loh, "Microstructuring of Graphene Oxide Nanosheets Using Direct Laser Writing," *Adv. Mater.* **22**(1), 67–71 (2010).

- [55] A. A. Ushkov, I. Verrier, T. Kampfe, and Y. Jurlin, "Subwavelength diffraction gratings with macroscopic moiré patterns generated via laser interference lithography," *Opt. Express* **28**(11), 16453 (2020).
- [56] F. Yu, P. Li, H. Shen, S. Mathur, C.-M. Lehr, U. Bakowsky, and F. Mücklich, "Laser interference lithography as a new and efficient technique for micropatterning of biopolymer surface," *Biomaterials* **26**(15), 2307–2312 (2005).
- [57] J. de Boor, N. Geyer, J. V. Wittemann, U. Gösele, and V. Schmidt, "Sub-100 nm silicon nanowires by laser interference lithography and metal-assisted etching," *Nanotechnology* **21**(9), 095302 (2010).
- [58] H. Wu, Y. Jiao, C. Zhang, C. Chen, L. Yang, J. Li, J. Ni, Y. Zhang, C. Li, Y. Zhang, S. Jiang, S. Zhu, Y. Hu, D. Wu, and J. Chu, "Large area metal micro-/nano-groove arrays with both structural color and anisotropic wetting fabricated by one-step focused laser interference lithography," *Nanoscale* **11**(11), 4803–4810 (2019).
- [59] N. Bonod and J. Neauport, "Diffraction gratings: from principles to applications in high-intensity lasers," *Adv. Opt. Photon.* **8**(1), 156 (2016).
- [60] R. W. Wood, "Anomalous Diffraction Gratings," *Phys. Rev.* **48**(12), 928–936 (1935).
- [61] L. J. Barbour, "EwaldSphere : an interactive approach to teaching the Ewald sphere construction," *J Appl Crystallogr* **51**(6), 1734–1738 (2018).
- [62] A. W. Snyder and J. D. Love, *Optical Waveguide Theory* (Springer US, 1984).
- [63] P. J. Chandler and F. L. Lama, "A New Approach to the Determination of Planar Waveguide Profiles by Means of a Non-stationary Mode Index Calculation," *Optica Acta: International Journal of Optics* **33**(2), 127–143 (1986).
- [64] M. L. Dakss, L. Kuhn, P. F. Heidrich, and B. A. Scott, "Grating coupler for efficient excitation of optical guided waves in thin films", *Appl. Phys. Lett.* **16**, 523-525 (1970).
- [65] H. Kogelnik and T. P. Sosnowski, "Holographic thin film couplers," in *The Bell System Technical Journal*, vol. 49, no. 7, pp. 1602-1608, Sept. 1970

- [66] G. A. Golubenko, A. S. Svakhin, V. A. Sychugov, and A. V. Tishchenko, "Total reflection of light from a corrugated surface of a dielectric waveguide," *Sov. J. Quantum Electron.* **15**(7), 886–887 (1985).
- [67] D. Rosenblatt, A. Sharon and A. A. Friesem, "Resonant grating waveguide structures," in *IEEE Journal of Quantum Electronics*, vol. 33, no. 11, pp. 2038-2059, Nov. 1997
- [68] S. Hernandez, O. Gauthier-Lafaye, A.-L. Fehrembach, S. Bonnefont, P. Arguel, F. Lozes-Dupuy, and A. Sentenac, "High performance bi-dimensional resonant grating filter at 850nm under high oblique incidence of $\sim 60^\circ$," *Appl. Phys. Lett.* **92**(13), 131112 (2008).
- [69] G. Cincotti, "Polarization gratings: design and applications," in *IEEE Journal of Quantum Electronics*, vol. 39, no. 12, pp. 1645-1652, Dec. 2003
- [70] S. R. Nersisyan, N. V. Tabiryan, D. M. Steeves, and B. R. Kimball, "The principles of laser beam control with polarization gratings introduced as diffractive waveplates," in I. C. Khoo, ed. (2010), p. 77750U.
- [71] M. Mutlu, A. E. Akosman, G. Kurt, M. Gokkavas, and E. Ozbay, "Experimental realization of a high-contrast grating based broadband quarter-wave plate," *Opt. Express* **20**(25), 27966 (2012).
- [72] A. G. Lopez and H. G. Craighead, "Wave-plate polarizing beam splitter based on a form-birefringent multilayer grating," *Opt. Lett.* **23**(20), 1627 (1998).
- [73] Kazuo Shiraishi, Satoshi Oyama, and Chen S. Tsai, "A Polarizer Using Thin Metallic-Film Subwavelength Grating for Infrared to Terahertz Region," *J. Lightwave Technol.* **29**, 670-676 (2011).
- [74] Xiaowei Guan, Pengxin Chen, Sitao Chen, Peipeng Xu, Yaocheng Shi, and Daoxin Dai, "Low-loss ultracompact transverse-magnetic-pass polarizer with a silicon subwavelength grating waveguide," *Opt. Lett.* **39**, 4514-4517 (2014) Xiaowei Guan, Pengxin Chen, Sitao Chen, Peipeng Xu, Yaocheng Shi, and Daoxin Dai, "Low-loss ultracompact transverse-magnetic-pass polarizer with a silicon subwavelength grating waveguide," *Opt. Lett.* **39**, 4514-4517 (2014).

- [75] G. Biener, A. Niv, V. Kleiner, and E. Hasman, "Computer-generated infrared depolarizer using space-variant subwavelength dielectric gratings," *Opt. Lett.* **28**(16), 1400 (2003).
- [76] C.-F. Kao, S.-H. Lu, H.-M. Shen, and K.-C. Fan, "Diffractive Laser Encoder with a Grating in Littrow Configuration," *Jpn. J. Appl. Phys.* **47**(3), 1833–1837 (2008).
- [77] Q. Lv, Z. Liu, W. Wang, X. Li, S. Li, Y. Song, H. Yu, Bayanheshig, and W. Li, "Simple and compact grating-based heterodyne interferometer with the Littrow configuration for high-accuracy and long-range measurement of two-dimensional displacement," *Appl. Opt.* **57**(31), 9455 (2018).
- [78] P. P. Lu, K.-X. Sun, R. L. Byer, J. A. Britten, H. T. Nguyen, J. D. Nissen, C. C. Larson, M. D. Aasen, T. C. Carlson, and C. R. Hoaglan, "Precise diffraction efficiency measurements of large-area greater-than-99%-efficient dielectric gratings at the Littrow angle," *Opt. Lett.* **34**(11), 1708 (2009).
- [79] M. Rumpel, B. Dannecker, A. Voss, M. Moeller, C. Moormann, T. Graf, and M. A. Ahmed, "Thermal behavior of resonant waveguide-grating mirrors in Yb:YAG thin-disk lasers," *Opt. Lett.* **38**(22), 4766 (2013).
- [80] N. V. Golovastikov, D. A. Bykov, and L. L. Doskolovich, "Resonant diffraction gratings for spatial differentiation of optical beams," *Quantum Electron.* **44**(10), 984–988 (2014).
- [81] M. Zourob and A. Lakhtakia, eds., *Optical Guided-Wave Chemical and Biosensors I*, Springer Series on Chemical Sensors and Biosensors (Springer Berlin Heidelberg, 2009), 7.
- [82] M. Neviere, E. Popov, R. Reinisch, and G. Vitrant, *Electromagnetic Resonances in Nonlinear Optics*, 0 ed. (CRC Press, 2000).
- [83] P. Genevet, J.-P. Tetienne, E. Gatzogiannis, R. Blanchard, M. A. Kats, M. O. Scully, and F. Capasso, "Large Enhancement of Nonlinear Optical Phenomena by Plasmonic Nanocavity Gratings," *Nano Lett.* **10**(12), 4880–4883 (2010).
- [84] C. Min, P. Wang, C. Chen, Y. Deng, Y. Lu, H. Ming, T. Ning, Y. Zhou, and G. Yang, "All-optical switching in subwavelength metallic grating structure containing nonlinear optical materials," *Opt. Lett.* **33**(8), 869 (2008).

- [85] A. Sharon, D. Rosenblatt, and A. A. Friesem, "Resonant grating–waveguide structures for visible and near-infrared radiation," *J. Opt. Soc. Am. A* **14**(11), 2985 (1997).
- [86] E. Popov, L. Mashev, and D. Maystre, "Theoretical Study of the Anomalies of Coated Dielectric Gratings," *Optica Acta: International Journal of Optics* **33**(5), 607–619 (1986).
- [87] S. Tibuleac and R. Magnusson, "Reflection and transmission guided-mode resonance filters," *J. Opt. Soc. Am. A* **14**(7), 1617 (1997).
- [88] K. Bougot-Robin, W. Wen, and H. Benisty, "Resonant waveguide sensing made robust by on-chip peak tracking through image correlation," *Biomed. Opt. Express* **3**(10), 2436 (2012).
- [89] D. A. Bykov, L. L. Doskolovich, and V. A. Soifer, "Coupled-mode theory and Fano resonances in guided-mode resonant gratings: the conical diffraction mounting," *Opt. Express* **25**(2), 1151 (2017).
- [90] A.-L. Fehrembach, K. Sharshavina, F. Lemarchand, E. Popov, A. Monmayrant, P. Arguel, and O. Gauthier-Lafaye, " $2 \times 1D$ crossed strongly modulated gratings for polarization independent tunable narrowband transmission filters," *J. Opt. Soc. Am. A* **34**(2), 234 (2017).
- [91] L. Macé, O. Gauthier-Lafaye, A. Monmayrant, and H. Camon, "Design of angularly tolerant zero-contrast grating filters for pixelated filtering in the mid-IR range," *J. Opt. Soc. Am. A* **34**(4), 657 (2017).
- [92] A. Monmayrant, S. Aouba, K. C. Shin Yu, P. Arguel, A.-L. Fehrembach, A. Sentenac, and O. Gauthier-Lafaye, "Experimental demonstration of 1D crossed gratings for polarization-independent high-Q filtering," *Opt. Lett.* **39**(20), 6038 (2014).
- [93] L. Chen, M. C. Y. Huang, C. F. R. Mateus, C. J. Chang-Hasnain, and Y. Suzuki, "Fabrication and design of an integrable subwavelength ultrabroadband dielectric mirror," *Appl. Phys. Lett.* **88**(3), 031102 (2006).

- [94] A. Ricciardi, S. Campopiano, A. Cusano, T. F. Krauss, and L. O’Faolain, "Broadband Mirrors in the Near-Infrared Based on Subwavelength Gratings in SOI," *IEEE Photonics J.* **2**(5), 696–702 (2010).
- [95] S. Zhang, Y. H. Ko, and R. Magnusson, "Broadband guided-mode resonant reflectors with quasi-equilateral triangle grating profiles," *Opt. Express* **25**(23), 28451 (2017).
- [96] R. Magnusson, "Wideband reflectors with zero-contrast gratings," *Opt. Lett.* **39**(15), 4337 (2014).
- [97] W. Yu, D. Wu, X. Duan, and Y. Yi, "Subwavelength grating wideband reflectors with tapered sidewall profile," *MRS Advances* **1**(23), 1683–1691 (2016).
- [98] J. E. Harvey and R. N. Pfisterer, "Understanding diffraction grating behavior: including conical diffraction and Rayleigh anomalies from transmission gratings," *Opt. Eng.* **58**(08), 1 (2019).
- [99] S. Enoch and N. Bonod, eds., *Plasmonics: From Basics to Advanced Topics*, Springer Series in Optical Sciences (Springer Berlin Heidelberg, 2012), **167**.
- [100] S. Block, E. Gamet, and F. Pigeon, "Semiconductor laser with external resonant grating mirror," *IEEE J. Quantum Electron.* **41**(8), 1049–1053 (2005).
- [101] M. J. Uddin and R. Magnusson, "Guided-Mode Resonant Thermo-Optic Tunable Filters," *IEEE Photon. Technol. Lett.* **25**(15), 1412–1415 (2013).
- [102] A. N. Enemu, R. R. Chaudhuri, Y. Song, and S.-W. Seo, "Thermo-Optic Sensor Based on Resonance Waveguide Grating for Infrared/Thermal Imaging," *IEEE Sensors J.* **15**(8), 4213–4217 (2015).
- [103] K. C. Harvey and C. J. Myatt, "External-cavity diode laser using a grazing-incidence diffraction grating," *Opt. Lett.* **16**(12), 910 (1991).
- [104] H. Loh, Y.-J. Lin, I. Teper, M. Cetina, J. Simon, J. K. Thompson, and V. Vuletić, "Influence of grating parameters on the linewidths of external-cavity diode lasers," *Appl. Opt.* **45**(36), 9191 (2006).
- [105] I. H. White, "A multichannel grating cavity laser for wavelength division multiplexing applications," *J. Lightwave Technol.* **9**(7), 893–899 (1991).

- [106] S. Iadanza, A. P. Bako, P. K. J. Singaravelu, D. Panettieri, S. A. Schulz, G. C. R. Devarapu, S. Guerber, C. Baudot, F. Boeuf, S. Hegarty, and L. O’Faolain, "Thermally stable hybrid cavity laser based on silicon nitride gratings," *Appl. Opt.* **57**(22), E218 (2018).
- [107] C. J. Chang-Hasnain and W. Yang, "High-contrast gratings for integrated optoelectronics," *Adv. Opt. Photon.* **4**(3), 379 (2012).
- [108] F. Brückner, D. Friedrich, T. Clausnitzer, O. Burmeister, M. Britzger, E.-B. Kley, K. Danzmann, A. Tünnermann, and R. Schnabel, "Demonstration of a cavity coupler based on a resonant waveguide grating," *Opt. Express* **17**(1), 163 (2009).
- [109] V. Karagodsky, C. Chase, and C. J. Chang-Hasnain, "Matrix Fabry–Perot resonance mechanism in high-contrast gratings," *Opt. Lett.* **36**(9), 1704 (2011).
- [110] M. Bassan, ed., *Advanced Interferometers and the Search for Gravitational Waves: Lectures from the First VESF School on Advanced Detectors for Gravitational Waves*, Astrophysics and Space Science Library No. volume 404 (Springer, 2014).
- [111] N. Mavalvala, D. E. McClelland, G. Mueller, D. H. Reitze, R. Schnabel, and B. Willke, "Lasers and optics: looking towards third generation gravitational wave detectors," *Gen Relativ Gravit* **43**(2), 569–592 (2011).
- [112] S. Kroker, T. Käsebier, F. Brückner, F. Fuchs, E.-B. Kley, and A. Tünnermann, "Reflective cavity couplers based on resonant waveguide gratings," *Opt. Express* **19**(17), 16466 (2011).
- [113] Kodo Kawase, Manabu Sato, Tetsuo Taniuchi, and Hiromasa Ito, "Coherent tunable THz-wave generation from LiNbO₃ with monolithic grating coupler", *Appl. Phys. Lett.* **68**, 2483-2485 (1996).
- [114] E. Treacy, "Optical pulse compression with diffraction gratings," *IEEE J. Quantum Electron.* **5**(9), 454–458 (1969).
- [115] Z. Li, S. Tokita, S. Matsuo, K. Sueda, T. Kurita, T. Kawasima, and N. Miyanaga, "Scattering pulse-induced temporal contrast degradation in chirped-pulse amplification lasers," *Opt. Express* **25**(18), 21201 (2017).

- [116] S. Fu, W. Zhang, W. Kong, G. Wang, F. Xing, F. Zhang, and H. Zhang, "Review of pulse compression gratings for chirped pulse amplification system," *Opt. Eng.* **60**(02), (2021).
- [117] N. Bonod et al.: "Diffraction gratings: from principles to applications in high-intensity lasers", *Advances in Optics and Photonics* 8, 156 (2016).
- [118] T. Waritanant and T. Chung, "Influence of Minute Self-Absorption of a Volume Bragg Grating Used as a Laser Mirror," *IEEE J. Quantum Electron.* **47**(3), 390–397 (2011).
- [119] Y. Li, V. Negoita, T. Barnowski, S. Strohmaier, and G. Treusch, "Wavelength locking of high-power diode laser bars by volume Bragg gratings," in *2012 IEEE Photonics Society Summer Topical Meeting Series* (IEEE, 2012), pp. 29–30.
- [120] A. L. Glebov, O. Mokhun, A. Rapaport, S. Vergnole, V. Smirnov, and L. B. Glebov, "Volume Bragg gratings as ultra-narrow and multiband optical filters," in H. Thienpont, J. Mohr, H. Zappe, and H. Nakajima, eds. (2012), p. 84280C.
- [121] R. Kazarinov, C. Henry, and N. Olsson, "Narrow-band resonant optical reflectors and resonant optical transformers for laser stabilization and wavelength division multiplexing," *IEEE J. Quantum Electron.* **23**(9), 1419–1425 (1987).
- [122] M. Li, N. Wan, B. Wang, H. Yu, Y. Yang, S. Yan, W. Sun, and X. Lin, "High Electrical-to-Green Efficiency 123 W Average-Power Quasicontinuous-Wave Laser at 532 nm in Compact Design," *J Russ Laser Res* **35**(6), 555–560 (2014).
- [123] B. M. Gibson and B. J. McCall, "Tilt-tuned etalon locking for tunable laser stabilization," *Opt. Lett.* **40**(12), 2696 (2015).
- [124] W. D. Kimura et al. "Laser acceleration of relativistic electrons using the inverse Cherenkov effect," *Phys. Rev. Lett.* **74**, 546-549 (1995).
- [125] Q. Zahn, "Trapping metallic rayleigh particles with radial polarization," *Opt. Exp.* **12**, 3377-3382 (2004).
- [126] R. Dorn et al, "Sharper Focus for a Radially Polarized Light Beam," *Phys. Rev. Lett.* **91**, 233901 (2003).
- [127] T. Nieminen et al. "Forces in optical tweezers with radially and azimuthally polarized trapping beams," *Opt. Lett.* **33**, 122-124 (2008).

- [128] R. Weber et al., "Effects of Radial and Tangential Polarization in Laser Material Processing", *Physics Procedia* 12 (A), 21-30 (2011).
- [129] M. Rumpel, et al., "Circular grating waveguide structures for intra-cavity generation of azimuthal polarization in a thin-disk laser," *Opt. Lett.* 37, 1763-1765 (2012).
- [130] F. Xu, C.-C. Cheng, A. Scherer, R.-C. Tyan, P.-C. Sun, and Y. Fainman, "Fabrication, modeling, and characterization of form-birefringent nanostructures," *Opt. Lett.* **20**(24), 2457 (1995).
- [131] C. Gu and P. Yeh, "Form birefringence dispersion in periodic layered media," *Opt. Lett.* **21**(7), 504 (1996).
- [132] T. Kämpfe and O. Parriaux, "Depth-minimized, large period half-wave corrugation for linear to radial and azimuthal polarization transformation by grating-mode phase management," *J. Opt. Soc. Am. A* **28**(11), 2235 (2011).
- [133] T. R. Groves, D. Pickard, B. Rafferty, N. Crosland, D. Adam, and G. Schubert, "Maskless electron beam lithography: prospects, progress, and challenges," *Microelectronic Engineering* **61–62**, 285–293 (2002).
- [134] U. D. Zeitner, M. Oliva, F. Fuchs, D. Michaelis, T. Benkenstein, T. Harzendorf, and E.-B. Kley, "High performance diffraction gratings made by e-beam lithography," *Appl. Phys. A* **109**(4), 789–796 (2012).
- [135] S. Donthu, Z. Pan, B. Myers, G. Shekhawat, N. Wu, and V. Dravid, "Facile Scheme for Fabricating Solid-State Nanostructures Using E-Beam Lithography and Solution Precursors," *Nano Lett.* **5**(9), 1710–1715 (2005).
- [136] P. Hudek and D. Beyer, "Exposure optimization in high-resolution e-beam lithography," *Microelectronic Engineering* **83**(4–9), 780–783 (2006).
- [137] A. Pimpin and W. Srituravanich, "Review on Micro- and Nanolithography Techniques and their Applications," *EJ* **16**(1), 37–56 (2012).
- [138] G. S. Pati, R. K. Heilmann, P. T. Konkola, C. Joo, C. G. Chen, E. Murphy, and M. L. Schattenburg, "Generalized scanning beam interference lithography system for patterning gratings with variable period progressions," *J. Vac. Sci. Technol. B* **20**(6), 2617 (2002).

- [139] C. G. Chen, P. T. Konkola, R. K. Heilmann, C. Joo, and M. L. Schattenburg, "Nanometer-accurate grating fabrication with scanning beam interference lithography," in D. K. Sood, A. P. Malshe, and R. Maeda, eds. (2002), p. 126.
- [140] M. Kim, C. Park, S. Je, H. Jang, C. Joo, and S. Kang, "Real-Time Compensation of Simultaneous Errors Induced by Optical Phase Difference and Substrate Motion in Scanning Beam Laser Interference Lithography System," *IEEE/ASME Trans. Mechatron.* **23**(4), 1491–1500 (2018).
- [141] M. Li, X. Xiang, C. Zhou, and C. Wei, "Scan angle error measurement based on phase-stepping algorithms in scanning beam interference lithography," *Appl. Opt.* **58**(10), 2641 (2019).
- [142] Häfner, M., et al. "Fabrication of rotational symmetric sub wavelength grating structures.", *DGaO proceedings*, ISSN: 1614-8436.
- [143] M. C. Traub, W. Longsine, and V. N. Truskett, "Advances in Nanoimprint Lithography," *Annu. Rev. Chem. Biomol. Eng.* **7**(1), 583–604 (2016).
- [144] H. Schiff, "Nanoimprint lithography: An old story in modern times? A review," *J. Vac. Sci. Technol. B* **26**(2), 458 (2008).
- [145] L. J. Guo, "Nanoimprint Lithography: Methods and Material Requirements," *Adv. Mater.* **19**(4), 495–513 (2007).
- [146] T. Khaleque, H. G. Svavarsson, and R. Magnusson, "Fabrication of resonant patterns using thermal nano-imprint lithography for thin-film photovoltaic applications," *Opt. Express* **21**(S4), A631 (2013).
- [147] Q. Xie, M. H. Hong, H. L. Tan, G. X. Chen, L. P. Shi, and T. C. Chong, "Fabrication of nanostructures with laser interference lithography," *Journal of Alloys and Compounds* **449**(1–2), 261–264 (2008).
- [148] J.-H. Seo, J. H. Park, S.-I. Kim, B. J. Park, Z. Ma, J. Choi, and B.-K. Ju, "Nanopatterning by Laser Interference Lithography: Applications to Optical Devices," *j. nanosci. nanotech.* **14**(2), 1521–1532 (2014).
- [149] F. Koch, D. Lehr, O. Schönbrodt, T. Glaser, R. Fechner, and F. Frost, "Manufacturing of highly-dispersive, high-efficiency transmission gratings by laser

- interference lithography and dry etching," *Microelectronic Engineering* **191**, 60–65 (2018).
- [150] Jung-Hun Seo, Jungho Park, Deyin Zhao, Hongjun Yang, Weidong Zhou, Byeong-Kwon Ju, and Zhenqiang Ma, "Large-Area Printed Broadband Membrane Reflectors by Laser Interference Lithography," *IEEE Photonics J.* **5**(1), 2200106–2200106 (2013).
- [151] D. Wang, Z. Wang, Z. Zhang, Y. Yue, D. Li, and C. Maple, "Effects of polarization on four-beam laser interference lithography," *Appl. Phys. Lett.* **102**(8), 081903 (2013).
- [152] T. Jia, X. Wang, Y. Ren, Y. Su, L. Zhang, H. Yang, Y. Qi, and W. Liu, "Incidence Angle Effects on the Fabrication of Microstructures Using Six-Beam Laser Interference Lithography," *Coatings* **11**(1), 62 (2021).
- [153] H. Kim, P. Baksh, M. Odstreil, M. Miszczak, J. G. Frey, L. Juschkina, and W. S. Brocklesby, "Lloyd's mirror interference lithography with EUV radiation from a high-harmonic source," *Appl. Phys. Express* **9**(7), 076701 (2016).
- [154] X. Li, Y. Shimizu, S. Ito, and W. Gao, "Fabrication of scale gratings for surface encoders by using laser interference lithography with 405 nm laser diodes," *Int. J. Precis. Eng. Manuf.* **14**(11), 1979–1988 (2013).
- [155] Y. Shimizu, "Laser Interference Lithography for Fabrication of Planar Scale Gratings for Optical Metrology," *Nanomanuf Metrol* **4**(1), 3–27 (2021).
- [156] K. Maru, Y. Yamamoto and K. Nakatsuhara, "Nb₂O₅-based Grating Coupler Employing Multiple Nb₂O₅/SiO₂ Layers in Integrated Probe for Cross-Sectional Velocity Distribution Measurement," 2021 26th Microoptics Conference (MOC), 2021.
- [157] R. Leitel, P. Heger, O. Stenzel, and N. Kaiser, "Theoretical treatment of thermal shifts in resonant grating waveguide structures," *J. Opt. A: Pure Appl. Opt.* **8**(3), 333–337 (2006).
- [158] Y. Wang, X. Gao, Z. Shi, L. Chen, M. Lopez Garcia, N. A. Hueting, M. Cryan, X. Li, M. Zhang, and H. Zhu, "Guided-Mode Resonant HfO₂ Grating at Visible Wavelength Range," *IEEE Photonics J.* **6**(2), 1–7 (2014).

- [159] D. Depla, S. Mahieu, and R. De Gryse, "Magnetron sputter deposition: Linking discharge voltage with target properties," *Thin Solid Films* **517**(9), 2825–2839 (2009).
- [160] D. M. Mattox and M. Plus, "History Corner A Short History : Magnetron Sputter Deposition," *Soc. Vac. Coaters* (2015).
- [161] S. Pongratz and A. Zöller, "Plasma ion-assisted deposition: A promising technique for optical coatings," *J. Vac. Sci. Technol. A Vacuum, Surfaces, Film.*, vol. 10, no. 4, pp. 1897–1904 (1992).
- [162] H. Takahashi, "Temperature stability of thin-film narrow bandpass filters produced by ion-assisted deposition," in *Proc.SPIE*, (1994).
- [163] P. J. Kelly and R. D. Arnell, "Magnetron sputtering: a review of recent developments and applications," *Vacuum* **56**(3), 159–172 (2000).
- [164] F. Bienert, T. Graf, and M. A. Ahmed, "Comprehensive theoretical analysis of the period chirp in laser interference lithography," *Appl. Opt.* **61**(9), 2313 (2022).
- [165] Coletti, G., et al. "Mechanical strength of silicon wafers depending on wafer thickness and surface treatment." *a, a 2000.80* (2006): 86.
- [166] "Interferential Devices - Twyman-Green Interferometer". *OPI - Optique pour l'Ingénieur*. 4 April 2012.
- [167] F. Bienert, T. Graf, and M. A. Ahmed, "Theoretical investigation on the elimination of the period chirp by deliberate substrate deformations," *Opt. Express* **30**, 22410-22420 (2022).
- [168] R.R.N. Rao, F. Bienert, M. Moeller, D. Bashir, A. Hamri, F. Celle, E. Gamet, M. A. Ahmed, and Y. Jourlin, "Quantitative investigation on a period variation reduction method for the fabrication of large-area gratings using two-spherical-beam laser interference lithography," *Opt. Express* **31**, 371-380 (2023).

